Advanced Thermal Insulation for Energy Efficient Buildings: Structural Performance of Aerogel Composite Panels

by

Thomas Goutierre

Submitted to the Department of Mechanical Engineering
in partial fulfillment of the requirements for the degree of

Master of Science in Mechanical Engineering

at the

MASSACHUSETTS INSTITUTE OF TECHNOLOGY

February 2011

Author .....
Department of Mechanical Engineering
December 10, 2010

Certified by .....
Lorna J. Gibson
Matoula S. Salapatas Professor of Material Sciences and Engineering
Thesis Supervisor

Accepted by .....
David E. Hardt
Chairman, Department Committee on Graduate Theses

Advanced Thermal Insulation for Energy Efficient Buildings: Structural Performance of Aerogel Composite Panels

by

Thomas Goutierre

Submitted to the Department of Mechanical Engineering
on December 10, 2010, in partial fulfillment of the
requirements for the degree of
Master of Science in Mechanical Engineering

Abstract

Aerogels are well known as exceptional thermal insulators. Thermal conductivities of 9 to 10 mW/m.K have been achieved at atmospheric pressure, and a moderate vacuum (between 1/3 and 1/10 of an atmosphere) can lower this number even further, to around 5 mW/m.K. However aerogels for insulation purposes are not widespread on the market. One of the major shortcomings of aerogels that prevent them from being more widely used is their extreme mechanical weakness and brittleness. In this thesis, we characterize and explain these low mechanical properties. We then propose a composite structure for a rigid aerogel panel, a sandwich panel with a truss core filled with monolithic aerogel. Mechanical and thermal properties are derived and partially tested for the truss cores. Several designs are studied and mechanical properties are derived in order to compare these designs. Some criteria for an efficient designs are given. Finally, we describe a first attempt to manufacture one of these composite structures on a small scale.

Thesis Supervisor: Lorna J. Gibson
Title: Matoula S. Salapatas Professor of Material Sciences and Engineering

Acknowledgments

First of all, I would like to thank my advisor, Professor Lorna Gibson, for her guidance during this work. In particular, I am grateful for her patient and efficient proof-reading of this thesis. I would also like to thank the other members of this project: Professor Leon Glicksman, Professor Taofang Zeng, Professor Gang Chen, Ellann Cohen, Yanjia Zuo and Yi He.

This project was made possible by financial support from the MIT-DuPont alliance.

I would like to thank Mike Tarkanian for its invaluable help for the manufacturing parts of this thesis; be also thanked Donald Galler, Yong Zhang, Yin-Lin Xie, Alan Schwartzman and Aaron Ramirez.

I am also grateful to Diane Rose and Leslie Regan for their help in this administrative maze that is MIT.

Thanks to the friends I had during my time at MIT: Stéphanie, Charlotte, Jonathan, Dan, CJ, Éric, Nicéphore and many others. Thanks also to Anne-Sophie for her patience and to our common friend Skype...

Special thanks to my labmate Yves Matton, who knows why...

Contents

List of Figures

List of Tables

Chapter 1

Introduction

A major element in meeting projected reductions in the nation's and the world's energy consumption and CO_2 generation is based on improved energy efficiency in the consumption sector. Buildings comprise the largest single sector, consuming approximately 40% of US primary energy (in 2006, 20.9% for the commercial sector and 18.0% for the commercial sector - the industrial sector is not included) and 70% of the US electricity (U.S. Energy Information Administration, 2008). In 2006, in the U.S., space heating and space cooling represented 49.9% of the total energy delivered to a residential building. For commercial buildings, heating and cooling represented 18.8%. Overall, space heating and cooling of residential and commercial buildings (not including heating and cooling of industrial buildings and transportation vehicles) accounts for 11.1 % of the total energy consumption in the United States. In Europe, where the residential sector accounted for 26.6% of the final energy consumption in 2005, heating represents still a higher component of the consumption: up to 67% in the group "EU-15", the members of the European Union before 2004 (European Environment Agency, 2008).

A number of organizations have established ambitious goals for the efficiency levels of future buildings. For example, the American Institute of Architects (AIA) and a number of other American organizations have a goal of achieving, by the year 2015, a minimum 70% reduction from the average regional (or country) level of consumption of fossil fuels used to construct and operate new and renovated buildings. They also would promote further reductions of remaining fossil-fuel consumption by 10 percentage points or more every five years after 2015, leading to carbon neutral buildings in 2030. This is known as the Architecture 2030 challenge. In the European Union, the Energy Efficiency Action Plans aims at a reduction of primary energy consumption as of 2005 by 20% by 2020 and assumes a potential for savings

in the household sector up to 25%, a large part being achieved by energy efficiency improvements reducing the heating energy used (European Environment Agency, 2008).

To reduce the overall energy consumption in the building sector requires a substantial reduction in energy consumption in existing buildings. The United States only builds 1 to 2 million new residential units in a normal year and has upwards of 100 million exiting units. Thus efficient retrofits of existing homes and commercial buildings will play a major role in the next few decades. The combination of space heating and cooling constitutes the largest energy use in residential and commercial buildings. The heating and cooling energy demand is directly related to the level of insulation in the exterior envelope of a building: primarily the performance of the walls and windows.

Many existing buildings have inadequate levels of installation in their external walls. Current methods of retrofit involve costly reconstruction or layering over the current exterior and/or infill of insulation in wall cavities. In northern climates this technique adds an additional hazard of moisture damage since the exterior addition adds another moisture barrier on the wrong side of the wall near the cold surface where condensation can occur. Conventional insulations can achieve up to an R value of 6 or 7 (imperial units) in a one inch thickness (*ie* a thermal conductivity of 20 to 24 mW/m.K) but they are subject to degradation in R value over time due to diffusion of low conductivity gas out of the insulation. Figure 1-1 shows values for common insulation materials. Several manufacturers have developed and test-marketed vacuum panels. However, the current designs are expensive and are made up of large vacuum elements so that the entire panel loses its superior insulation performance if the protective coating suffers a single puncture.

Aerogels are sol-gel derived solid materials with porosities from about 80% to 99.8%. The high porosity is achieved via supercritical drying or freeze drying of an alcogel or a hydrogel. Aerogels were first made by S. S. Kistler (Kistler, 1931) in the early thirties. An aerogel block is shown on Figure 1-2. Aerogels, and particularly silica aerogels, have been rapidly identified as excellent thermal insulators, with conductivity between 9 and 17 mW/m.K at atmospheric pressure. Existing literature also shows that that the thermal conductivity can even be reduced to between 4 and 8 mW/m.K when evacuated, and even with only a moderate vacuum, a fraction of an atmosphere, between 1/3 and 1/10 (Lee et al., 1995). Other potential improvements to aerogel thermal conductivity include reducing thermal radiation in the aerogel.

An important new product would combine a vapor and infiltration barrier with a thin insulation panel

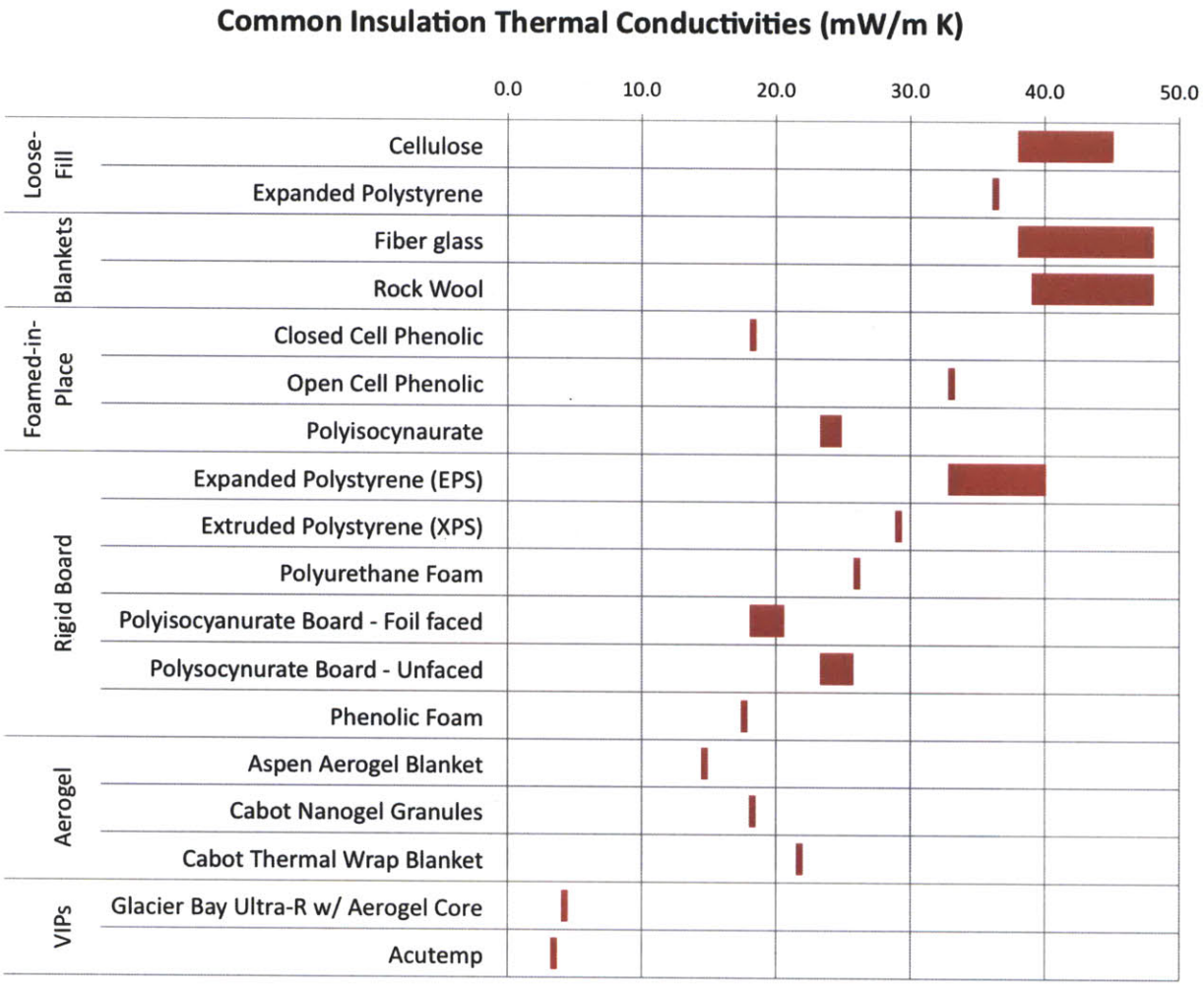

Figure 1-1: Thermal conductivities of common insulation materials, from (Cohen, 2011). VIP = Vacuum Insulation Panel

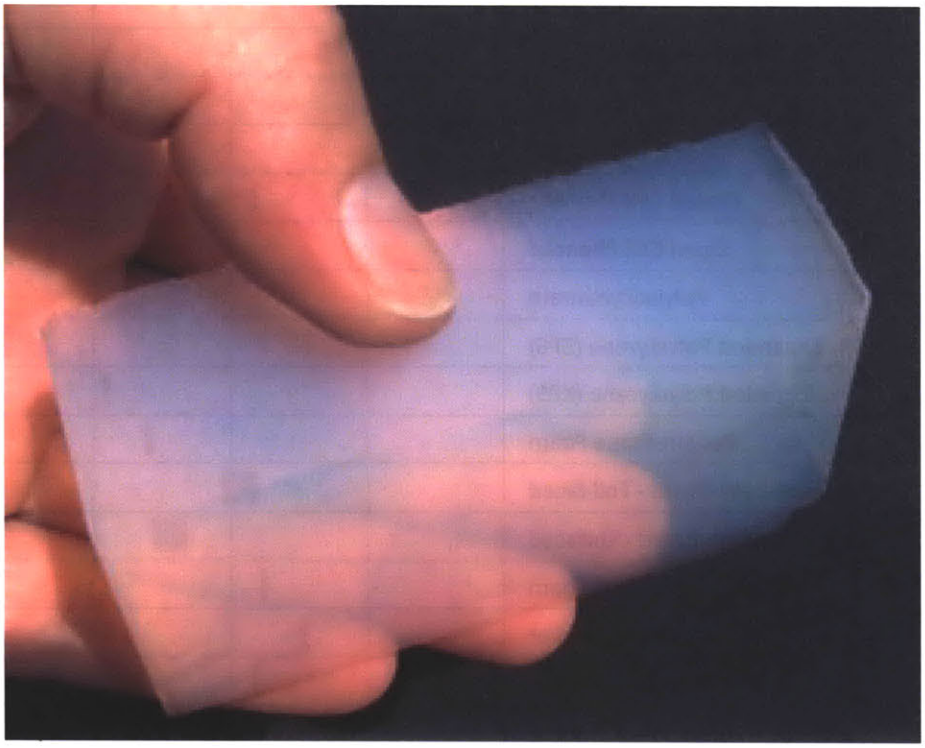

Figure 1-2: A block of silica aerogel, from www.aerogel.org

that has a substantial R value, for example R-10 (imperial units) in a half inch thickness or less, that is a thermal conductivity of 7 mW/m.K. The thin panel would allow retrofits over interior wall surfaces without a major impact on interior building geometry and smoother joints with windows. The proposed insulation would be twice as good as aerogel insulations at room temperature and pressure.

Despite its well known potential as a thermal insulator, aerogel has never been widely used for that purpose. It seems that there are two main reasons for that: one being that its manufacturing is complicated and expensive, and the other is that its mechanical properties are low, preventing one to fully use its potential.

The mechanical properties of aerogels are indeed low: for a typical 5% dense silica aerogel, Young's moduli are between 1-10 MPa, compressive strengths are about 0.5 MPa and tensile strengths are on the order of 0.01 MPa. These properties can be related to the porous structure of aerogels, which resembles that of foams, although they generally have a much more disconnected microstructure. Although the insulation panels do not carry structural loads in use and presumably would be adhered to a solid panel in retrofitting applications, they must be able to withstand loads associated with fabrication, transportation and installation.

This work focuses on proposing a design for an insulation panel that could achieve a very high thermal resistance while being sufficiently strong to be practical.

This thesis is part of a project funded by the MIT-DuPont Alliance. The project is led by Professor Leon Glicksman, an expert on heat transfer and building technology. Co-PIs for the project are Professor Gang Chen, an expert in thermal conductivity characterization and nanoscale heat transfer, Professor Lorna Gibson (advisor for this thesis), an expert in mechanical properties of porous media, and visiting assistant professor Taofang Zeng, an expert in aerogel synthesis. Three other graduate students have also been working on this project: Ellann Cohen on measuring the thermal properties of aerogels and Yanjia Zuo and Yi He on the synthesis and characterization of aerogels.

This thesis is organized in three main chapters.

The next chapter is a review of different aspects of aerogels relevant to our study: their microstructure, their mechanical properties, their commercial availability. It concludes that monolithic aerogel (as opposed to granulates in diverse forms) are required to achieve superior insulation properties, but that monolithic aerogel cannot be strengthened sufficiently by modifying the chemistry. That is why we

propose to study a composite structure with macroscopic elements to support the mechanical loads.

The third chapter focuses on analyzing structures that could act as a structural skeleton of a panel filled with aerogel, honeycombs and truss cores. We carry a theoretical analysis of those cores as a function of their geometry and their relative density. Then we test that the mechanical behavior of polystyrene truss cores fits the analysis.

The fourth chapter derives properties for several proposed panel designs and gives criteria for an efficient design. The last part of this chapter is a first try at the implementation of a composite panel with a truss core and a solid aerogel filling.

Chapter 2

Aerogel

2.1 Introduction

In this chapter, we first review the microstructure and mechanical properties of aerogels.. This review is mainly based on the literature but also on some characterizations made during this study. We then give an overview of commercially available aerogels. In the last section, we will see how an aerogel product could meet the specifications of the project and, based on a comparison with other insulating materials, we will see that this goal cannot be achieved by monolithic aerogel alone.

2.2 Aerogel structure and characterization

Generally, three basic techniques can be used to reveal structural features of aerogels (Fricke and Emmerling, 1992): direct methods (electron microscopy), adsorption or penetration measurements and indirect measurements (scattering techniques). Here we are applying these characterization methods to the case of silica aerogel, but they could be used for any kind of aerogel.

2.2.1 Electron Microscopy

Electron microscopy yields a direct image of the structure. Morphological features such as particle shapes, particle arrangements can be recognized. Two different techniques can give complementary information: SEM (Scanning Electron Microscopy) and TEM (Transmission Electron Microscopy). Both qualitative and quantitative information can be deduced from microscopy.

SEM

SEM images the sample surface by scanning it with a high-energy beam of electrons in a raster scan pattern. The detection of secondary electrons or back-scattered electrons contains information on the sample surface topography.

SEM imaging of aerogels (see Figure 2-1) is commonly performed for structural investigation (Rousset et al., 1990; Dumas et al., 1990; Vacher et al., 1991; Bouaziz et al., 1992; Pajonk et al., 1996; Rigacci et al., 1998; Martin et al., 2001; Kucheyev et al., 2007).

For basic SEM imaging, the sample has to be coated with a conductor to get a good resolution. Otherwise, electrons from the electron beam accumulate in the sample and have an effect on the imaging (charging artefacts) which limit the magnification one can achieve. The coating consists in vaporizing a conductive material on the sample at low pressure (typically 1 Pa), so that the sample is coated by a thin layer of conductor, typically 10-20 nm (Vacher et al., 1991).

The most common coating material is gold (Rousset et al., 1990; Dumas et al., 1990; Bouaziz et al., 1992). Another study (Pajonk et al., 1996) uses gold containing 20% palladium. Osmium impregnation followed by Pt coating is also reported. Vacher et al. (Vacher et al., 1991) report that Au coating produces artefacts that are not related to the actual structure of aerogels, namely a peculiar grainy appearance. They affirm that gold is well known, particularly among biologists, to limit the resolution of SEM pictures significantly, as it tends to clump. On the other hand, Pt/C coatings are known to give

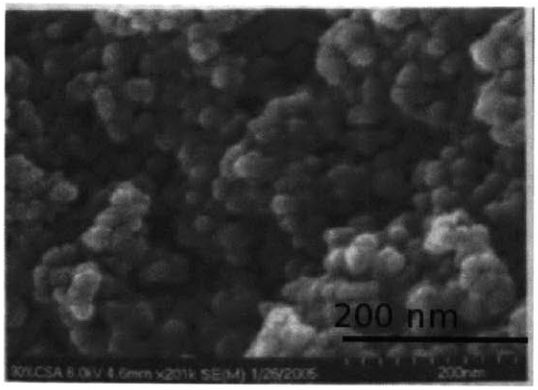

Figure 2-1: SEM photographs of silica aerogels (Roy and Hossain, 2008)

generally excellent results for fragile samples. In Figure 2-2, on the left, one see "grains". The grains show a microstructure at a scale of the order of 10nm typical for gold crystallization. The grains are well separated, giving the visual impression of a large inter-grain porosity (the dark areas between the grains). On the right of Figure 2-2, by contrast, one notes that the structure becomes finer as the density is decreased. Clearly the Pt/C coating preserves part of the fractal structure of the lightest sample. It does not have the mobility of gold, and thus forms neither the fine microstructure nor the large clumps that appear on the left-hand side. The latter might result from local damage produced by capillary forces. One does not gain the impression that the materials are "large scale aggregates of grains" as is the case for images with gold.

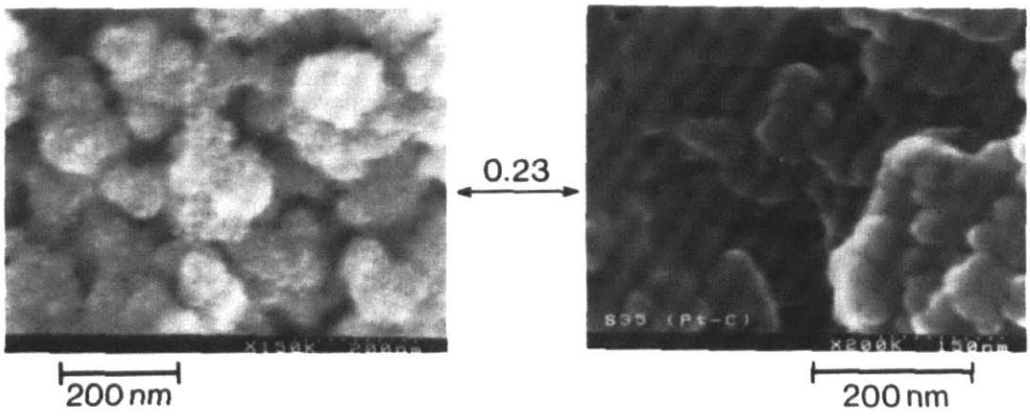

Figure 2-2: Scanning electron micrographs from (Vacher et al., 1991) for $\rho = 0.23 g/cm^3$. The left side shows surfaces with a gold coating, while the right side shows them with the Pt/C coating.

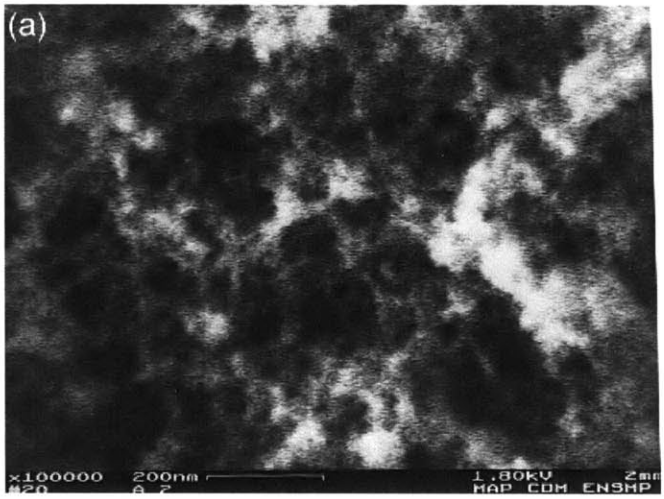

Figure 2-3: High resolution scanning electron microscopy of silica aerogels (Rigacci et al., 1998). Specimens are made under acidic conditions, samples are uncoated.

The coating process is far from trivial for a tenuous material, and it can have dramatic effects on fragile structures. An alternative approach is to use uncoated samples. This affects the resolution due to the charging effects in conventional SEM. The charging effects can be decreased using a low-vacuum mode available on certain SEM (Kucheyev et al., 2007), the electrons leaving the sample thanks to the ions in the surrounding gas. However, very good resolution has never been achieved by these means. Progress in techniques, such as high-resolution SEM with a field-emission, give reasonably good images on uncoated samples, as seen on Figure 2-3 (Rigacci et al., 1998).

We performed imaging with a thin gold coating on a LEO VP438 (LEO Elektronenmikroskopie, Oberkochen, Germany), see Figure 2-4. Although the resolution achieved was relatively low, one can see the aggregate of particles reported in other studies.

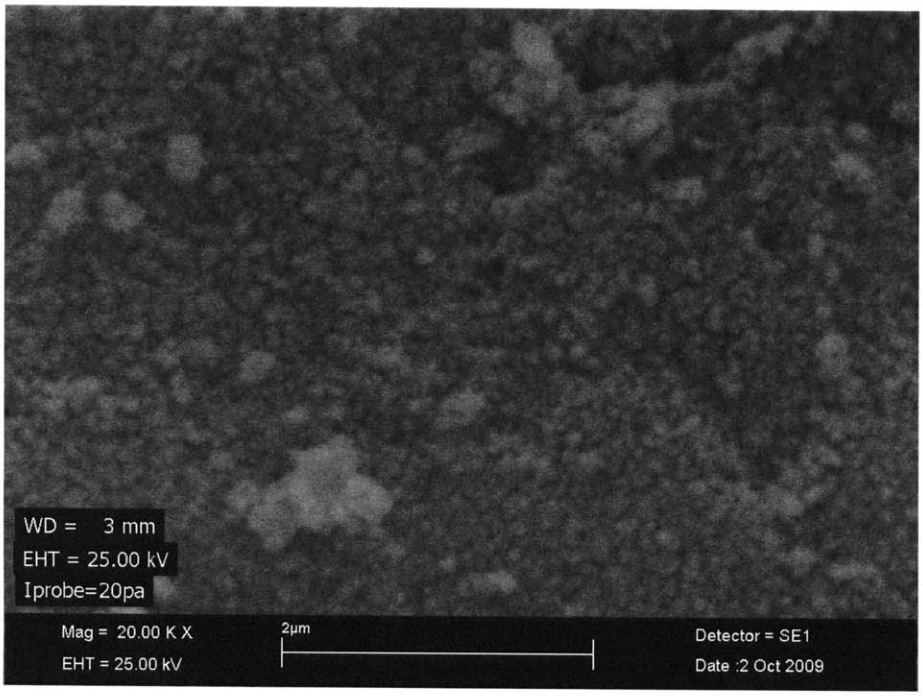

Figure 2-4: Image obtained with our SEM

TEM

TEM is a microscopy technique whereby a beam of electrons is transmitted through an ultra thin specimen, interacting with the specimen as it passes through. An image is formed from the interaction of the electrons transmitted through the specimen.

TEM gives higher resolution than SEM of approximately one order of magnitude.

TEM studies of aerogels have been performed (Rousset et al., 1990; Bourret, 1988; Ruben et al., 1995; Stroud et al., 2004). Due to the brittleness of aerogels, preparation of thin monolithic samples is impossible. Therefore, one has to grind the aerogel into a powder and then disperse the powder on a carbon support film. Often a solvent, e.g., acetone, ethanol, hexane, etc., is used to prevent aggregation of the powder on the support film, providing a more uniform distribution of particles. The use of a solvent is not strictly necessary, and in some cases leads to alteration of the aerogel structure. It is best to use dry grinding when feasible and to test several solvents if one is required. Typical images are shown on Figures 2-5 - 2-8.

Images on Figures 2-7 and 2-8 were made in this study using a TEM JEOL 200CX (Jeol Ltd., Tokyo, Japan). The aerogel was ground in a mortar and then put in ethanol before being dispersed on a copper

grid.

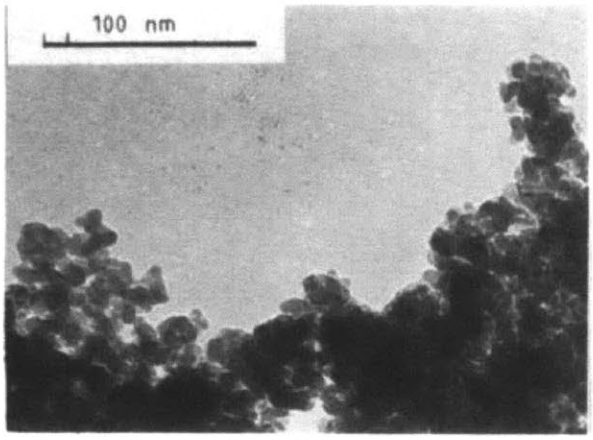

Figure 2-5: Transmission electron micrograph of a silica aerogel (ρ=0.23 g.cm^{-3}) (Rousset et al., 1990)

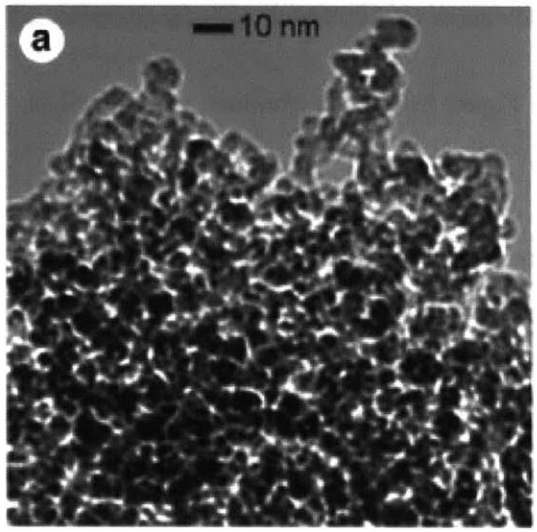

Figure 2-6: Conventional bright-field images of a silica aerogel obtained by TEM (Stroud et al., 2004)

Stereopairs can be taken to study the 3D arrangement (Bourret, 1988). A tilt angle of $\pm 5°$ is usually sufficient. Stereopairs can be examined on a stereoscope with a moving luminous spot which allows measurement of height differences. One can then identify the number of chains at crossing points.

Ruben et al. (Ruben et al., 1995) performed vertical replication of a fracture surface with a thin layer of platinum and carbon, which produces informative images, avoiding dispersing the sample in a solvent. However, the procedure is tedious and expensive.

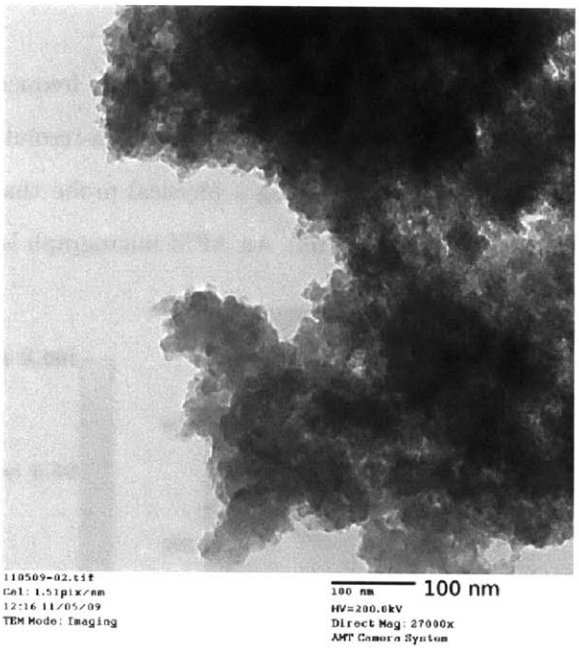

Figure 2-7: Image of one of our samples obtained by TEM

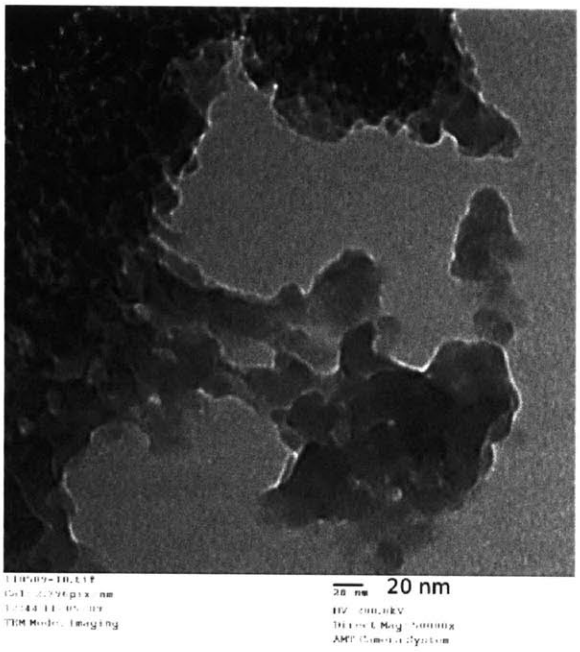

Figure 2-8: Image of one of our samples obtained by TEM

Atomic Force Microscopy

Atomic Force Microscope (AFM) has also been used, although not as frequently, to study aerogel structure (Borne et al., 1995; Marlière et al., 2001). The AFM is a high-resolution type of scanning probe microscopy, meaning it forms images of surfaces using a physical probe that scans the specimen, with demonstrated resolution of fractions of a nanometer. An AFM micrograph is shown on Figure 2-9.

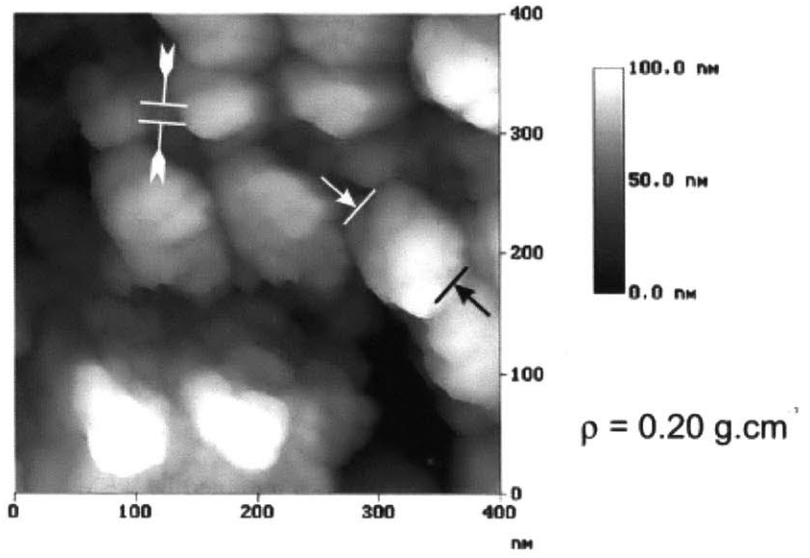

Figure 2-9: AFM data of the fracture surface of aerogel with a density of 0.20 g.cm^{-3}. The facing black and white arrows indicate the typical size of the aggregate of clusters, the facing white ones that of the clusters, as deduced from the AFM measurements (Marlière et al., 2001)

Results

Differences between acid-catalysed and basic-catalysed aerogels The structure of aerogel appears to be strongly dependent on the catalyst used during the condensation of the gel.

- Under acidic conditions, the silicic acid monomers condense slowly, which leads to the formation of polymer-like silica chains, resulting in a weakly cross-linked, low density network.
- Under basic conditions the condensation is rapid compared to the hydrolysis. One observes comparatively dense, colloidal particles; their final size depends on the temperature and on the pH-value of the solution.

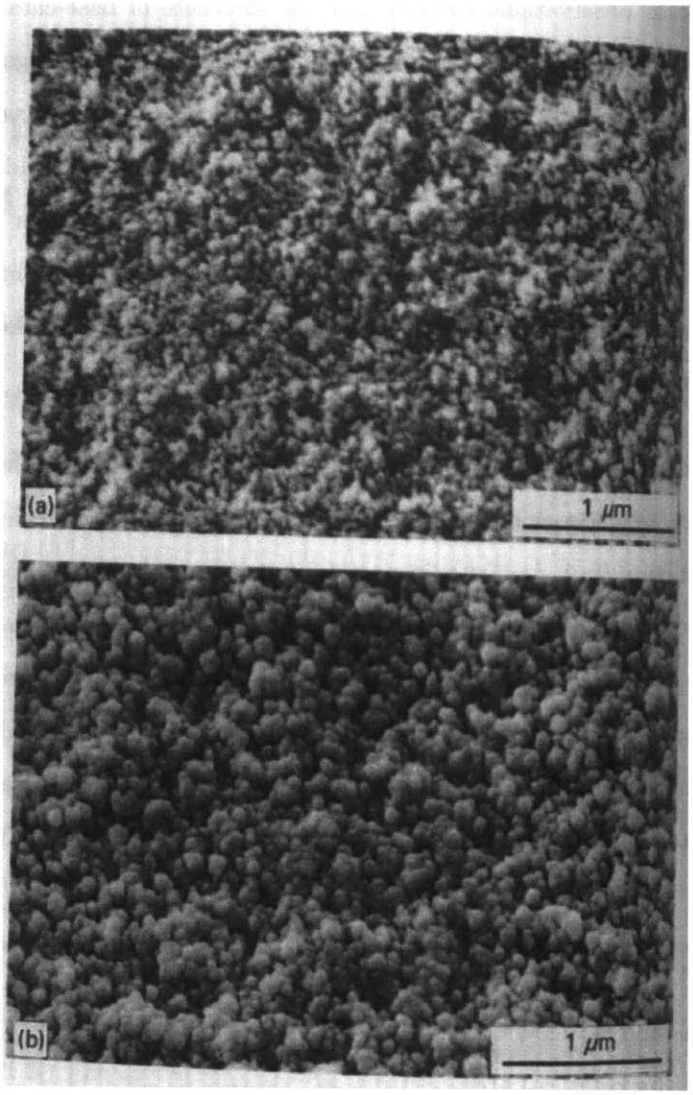

Figure 2-10: SEM photographs of silica aerogels prepared using (a) acidic (HCl) and (b) basic (NH_4OH) catalysed alcogels (Pajonk et al., 1996)

This distinction can be observed on Figure 2-10. One can see clearly the dense and colloidal particles for base-catalysed aerogel. Note that the aerogels synthesized for this study were condensed under basic conditions.

3D-structure The TEM observations confirm that the structure of base-catalysed aerogels is a 3D network, an open structure of small chains of diameter a_0, interconnected at average distances d_0 (Bourret, 1988) (Figure 2-11). The structure is best described by cylindrical chains: however some modulation of these chains is sometimes visible which could be reminiscent of initially spheroidal particles in the wet stage. At connecting points the number of departing branches is either three or four. Inside the chain the contrast is typical of a homogeneous amorphous medium. No sign of crystallinity is present and the material contained in each individual chain of the 3D-network is homogeneous down to a level of 5 to 8 Å (lowest resolution obtained).

The structure of acid-catalysed gels is more compact even at a very small scale. The chain diameters are smaller, $\sim$ 30 Å, and the network is much tighter. Moreover, the surface of each element is wavy and rough down to the resolution limit ($\sim$ 5 Å). In particular it is not possible to find any element even at the highest resolution level where the matter is homogeneously distributed. However, chains of denser material are still visible although the acid-catalysed gel structure is not always constant throughout the specimen. Some polydispersity is present and chains are sometimes better described as aggregates of small blocks or spheres (this is reflected in a smaller $\frac{d}{a}$ ratio as compared to the base catalysed gels). Bourret (Bourret, 1988) postulated that at the atomic resolution level, polymer chains, $(SiO_2)_n$ molecules, are the basic material forming a 3D network. At the lowest hierarchy level the diameter of this chain is therefore defined by twice the average ionic radius of oxygen and silicon and postulated to be of the order of 2.8 Å.

As we said earlier, a_0 and d_0 depend greatly on the catalysis method.

catalysis pH	a_0	d_0	$\frac{d_0}{a_0}$
basic	40 Å	130 Å	3.15
acidic	30 Å	70 Å	2.15

It is observed that this 3D network forms aggregates (clusters, "blobs") whose size has an order of magnitude of 100 nm (typical results from SEM imaging), which could be interpreted as a higher level network, although it is much more difficult to characterize (see Figure 2-12). Again, the size of this bigger

structural feature depends on the catalysis. Bourret reports the size of the aggregates is 25 nm for acidic catalysed aerogels and 75 nm for basic catalysed ones. However, the voids are much more difficult to characterize, and no study gave a good description of porosity at that level.

Fractal Geometry Direct observation reveals aerogels to be self-similar (fractal) materials, although historically the fractal character of aerogels has been first brought to light by scattering experiments (see subsection 4).

Bourret (Bourret, 1988) reports in his TEM study different levels of self-similarity in aerogels. These can be observed over two orders of magnitude in the case of acid catalysed gels (roughly three similar levels), slightly less in the case of basic catalysed gels (two similar levels), see Figure 2-13.

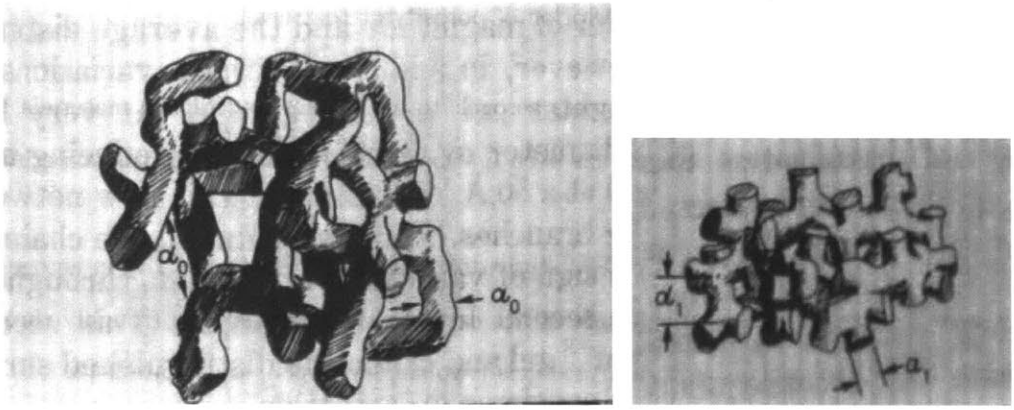

Figure 2-11: Aerogel structure of (a) base-catalysed aerogel and (b) acid-catalysed aerogels (Bourret, 1988). The scales are the same. The material contained in the chains of the base-catalysed aerogel appears to be homogeneous, while the material contained in the chains of the acid-catalysed aerogel is not homogeneous and supposed to be a 3D network of polymer-like chains

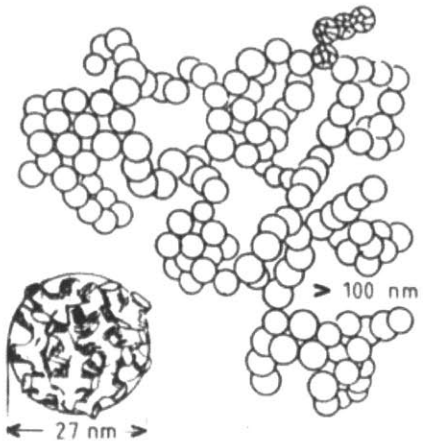

Figure 2-12: Sketch of the aerogel structure deduced from electron microscopy, with larger scale aggregates (Rousset et al., 1990)

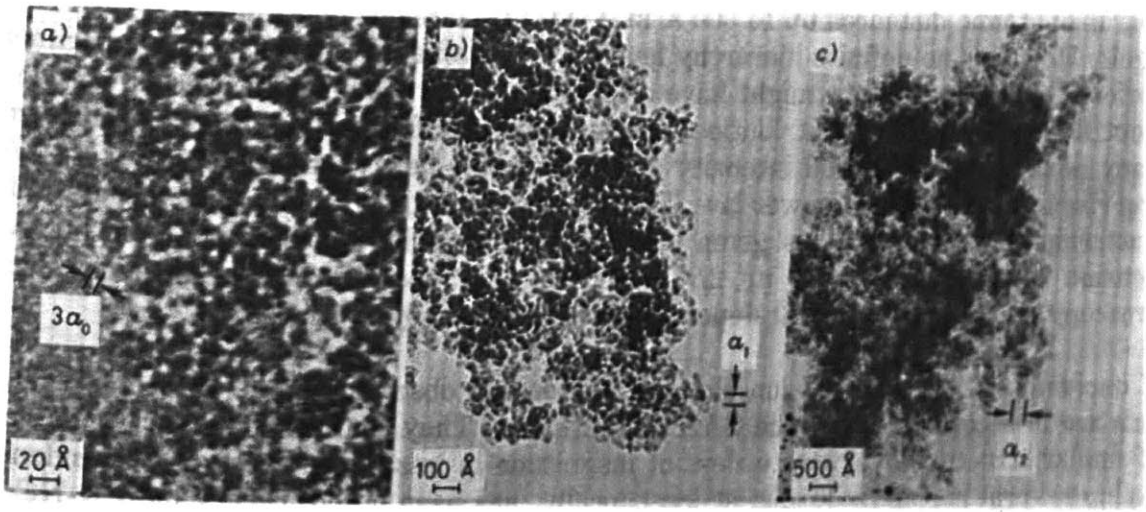

Figure 2-13: Different levels of organization in acid-catalysed aerogels, from (Bourret, 1988)

2.2.2 Adsorption and Penetration Measurements

The porosity Φ of an aerogel is derived with the formula $\Phi = 1 - \frac{\rho}{\rho_S}$, where ρ is the density of the aerogel and ρ_S the density of the material it is made of (ρ_S=2.6 g.cm^{-3} in the case of silica). Porosity as high as 99.8% has been reported (Pajonk et al., 1996). Now we want to characterize the shape and the size distribution of these voids.

The common techniques for characterizing porosity are mercury porosimetry, thermoporometry and nitrogen adsoption (Lowell et al., 2004; Scherer, 1998).

However, characterization of the pore size distribution in aerogels is complicated by their extreme compressibility (Scherer, 1998). These techniques apply capillary pressures on the aerogel network that can cause large volumetric compression, leading to false values for the pore volume and pore size. Since the bulk modulus of aerogels is known to exhibit a power-law dependence on density ($K \propto \rho^m$), it is possible in some cases to estimate the magnitude of the compression and then to derive the true distribution. The contraction levels for each methods are sketched on Figure 2-14.

It is necessary to mention that the pores of aerogels are not closed cells but rather spaces between filaments (Alié et al., 2001), thus it is hard to identify a "pore size" in such a geometry.

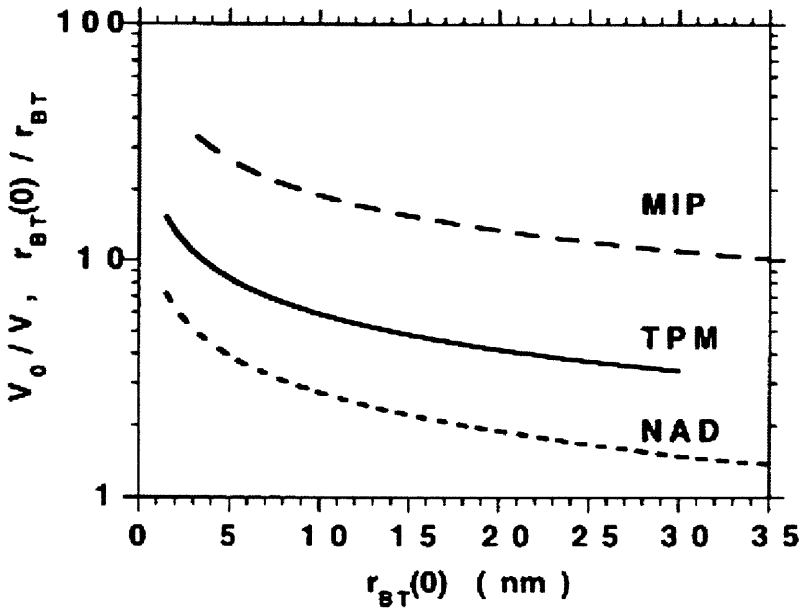

Figure 2-14: Volumetric contraction, $\frac{V}{V_0}$, and change in pore radius $\frac{r}{r(0)}$, of gel with bulk modulus $K_0 =$ 2 MPa and $m = 3$ (as in equation 2.1), as function of initial pore radius $r(0)$ when measured by mercury porosimetry (MIP), thermoporometry using water (TPM), or nitrogen adsorption/desorption (NAD), from (Scherer, 1998)

Mercury penetration porosimetry

Mercury porosimetry gives information on the structure of mesopores (2-50 nm) and macropores (>50nm). A material's porosity is characterized by applying various levels of pressure to a sample immersed in mercury. The pressure required to intrude mercury into the samples' pores is inversely proportional to the size of the pores. As pressure on the filled penetrometer increases, mercury intrudes into the samples' pores, beginning with those pores of largest diameter. The analysis of the distribution of the specific surface area and of the specific pore volume in relation with the pore size from mercury porosimetry data is classically based on Washburn's equation, which can be written in our case :

$$D = (\frac{1}{P})4\gamma cos(\phi)$$

where D is the pore diameter, P is the applied pressure, γ the surface tension of mercury and ϕ the contact angle between the mercury and the sample. The volume V of mercury penetrating the pores is measured directly as a function of applied pressure. This P-V information serves as a unique characterization of pore structure.

Yet, in the case of aerogels, it has been observed experimentally that the structure of aerogels is damaged by the high pressure required to intrude small cells. This can be explained by the small value of the Young modulus and of the ultimate compressive strength of aerogels. Consequently, Washburn's equation cannot be applied to aerogels (Pirard et al., 1995; Scherer et al., 1995b).

It has been suggested that one can estimate the amount of compression that will occur before mercury enters a gel (Pirard et al., 1995; Scherer et al., 1995a). From these estimates a correction can be made and the actual values of the pore sizes can be derived, see Figure 2-15.

The bulk modulus K, defined by $dP = -K\frac{dV}{V}$ (P is the pressure applied isostatically and V the resulting volume), is found to be for an aerogel (Scherer, 1998):

$$K(V) = \begin{cases} K_0 & \text{if } V \leqslant V_y \text{ where } V_y \text{ is a threshold volume depending on the sample} \\ K_0(\frac{V_y}{V})^m & \text{if } V \geqslant V_y \end{cases} \tag{2.1}$$

However, this estimate depends on the model for the elastic modulus, and it cannot be applied is the structure is not only compressed but modified by the compression. Furthermore, the shrinkage is so substantial that it reduces significantly the range of pores that can be explored, limiting greatly its

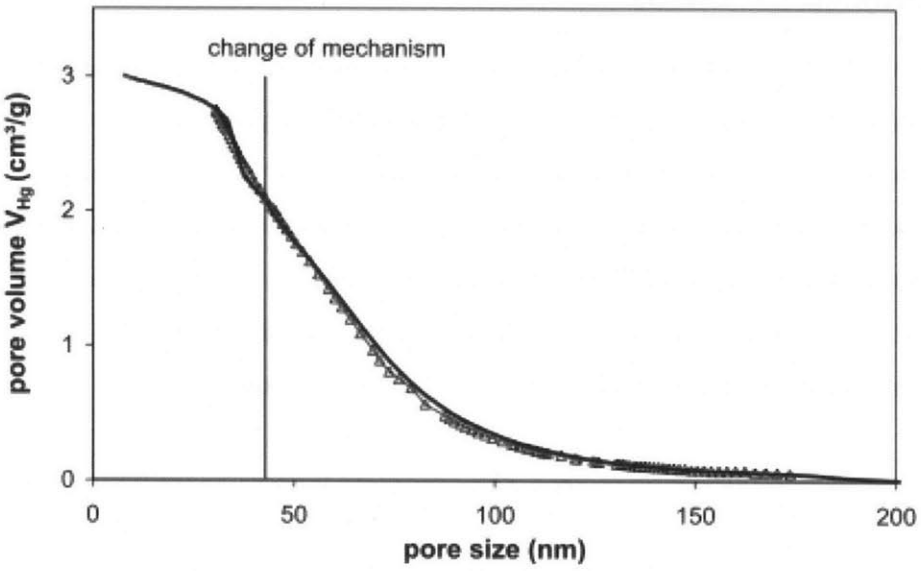

Figure 2-15: Pore size distribution by mercury porosimetry after correction, from (Alié et al., 2001)

applicability for mesopores determination if the gel is too compliant.

Nitrogen Adsorption / Desorption

Capillary condensation isotherms of vapors are widely used for calculations of pore size distributions (PSD) in nanoporous materials.

The principle of adsorption measurements (Lowell et al., 2004) is to observe the weight W of gas adsorbed in a material as a function of the absolute temperature T, the pressure P, and the interaction potential E between the vapor (adsorbate) and the surface (adsorbent). Usually the quantity adsorbed is measured at constant temperature:

$$W = F(P, E)$$

A plot of W versus P, at constant T, is referred to as the sorption isotherm of a particular gas-solid interface.

The state and thermodynamic stability of pure fluids in mesopores (pores exhibiting diameter from 2 to 50 nm) depends on the interplay between the strength of fluid-wall and fluid-fluid interactions on the one hand, and the effects of confined pore space in the other hand. The most prominent phenomenon observed in mesopores is pore condensation, which represents a first order phase transition from a gas-like state to a liquid-like state of the pore fluid occuring at a pressure P less than the corresponding saturation pressure P_0 of the bulk fluid, i.e., pore condensation occurs at a chemical potential μ less than the value μ_0 at gas-liquid coexistence of the bulk fluid. It is thus possible to calculate the pore radius as a function of P and P_0.

The basic equation is the Kelvin equation:

$$\ln(\frac{P}{P_0}) = \frac{-2\gamma\overline{V}}{rRT}$$

where R is the universal gas constant, γ is the surface tension of the liquid, $\overline{V}$ the molar volume of the condensed liquid and r the mean radius of curvature of the meniscus of the pore liquid (equal to the actual radius of the pores in the case of cylindrical pores).

To be complete, one has to take in account a multilayer adsorbed at the onset of pore condensation. Then one obtains the modified Kelvin equation $\ln(\frac{P}{P_0}) = \frac{-2\gamma\overline{V}}{(r-t_c)RT}$, where t_c describes the statistical thickness prior to condensation. t_c can be calculated under geometrical assumptions on the shape of the pores. The standard methods for the PSD calculations, such as the Barrett-Joiner-Halenda (BJH) method (Barrett et al., 1951) are based on a description of the capillary condensation to calculate t_c. An

example of PSD obtained by this method is given on Figure 2-16.

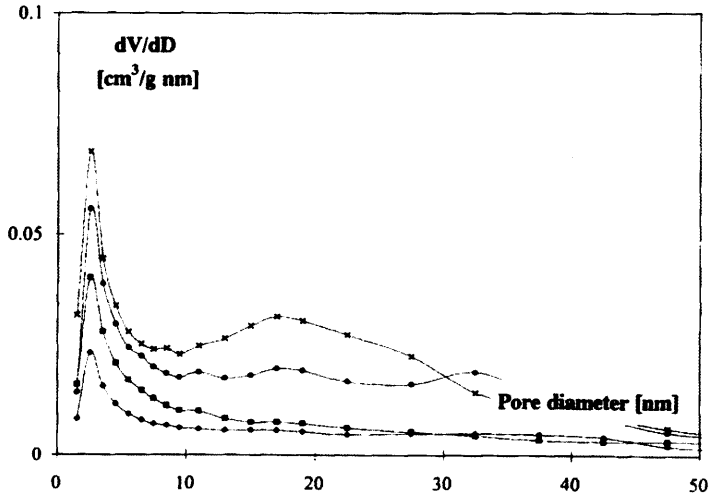

Figure 2-16: PSD obtained by N_2 adsorption for four different types of aerogels (Jarzebski et al., 1995)

However, this method has been questioned in the case of compliant materials, as the capillary pressures upon sorption can be as large as several MPa and thus large deformations are expected upon analysis. Reichenauer and Scherer (Reichenauer and Scherer, 2001) introduced a technique to correct the isotherms: simultaneous recording of nitrogen sorption data and linear length changes reveals a new type of isotherm. Comparison of dilatation and sorption data shows that the bulk modulus of a compliant material can be calculated from its nitrogen sorption isotherm alone. Using this information together with a model that describes the relationship between macroscopic deformation and changes in pore size and volume, the isotherm can be corrected for the contraction of the sample during analysis. The corresponding pore size distribution is found to be in excellent agreement with results deduced from small angle X-ray scattering (see Figure 2-17).

The nitrogen adsorption/desorption method also gives information about the specific area, using the same equations as those used for pore size characterization. The surface area is derived from the weight of the monolayer of adsorbate. The specific surface area is found to be in the range 200-800 m^2/g, increasing with the density (Rigacci et al., 1998; Hüsing et al., 1998). Only surfaces that are accessible to N_2 are detected.

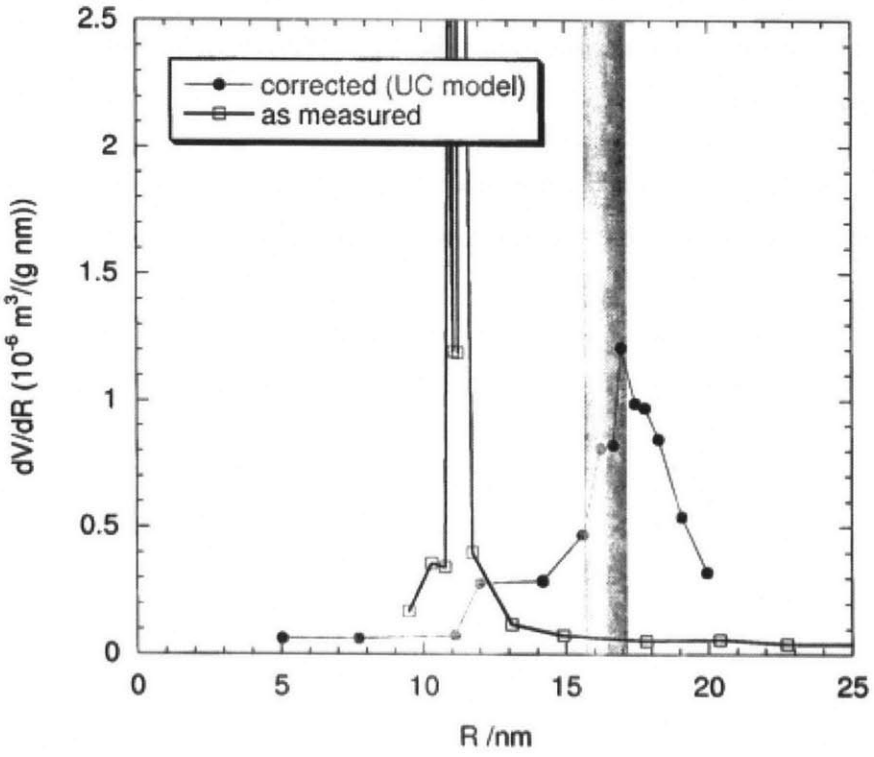

Figure 2-17: "As measured" and corrected datas from N_2 adsorption (Reichenauer and Scherer, 2001). The shaded area marks the average chord length in the pore phase as derived from SAXS.

Thermoporometry

Thermoporometry has been described by Brun et al.(Brun et al., 1977). A thermodynamic study of the liquid-solid phase transformation in porous materials provides the relationships between the size of the pores in which solidification takes place and the temperature of the triple point of the divided liquid, on the one hand, and between this temperature and the apparent solidification energy on the other hand.

Indeed, when the liquid in a pore freezes, the pore walls impose positive curvature on the crystal, so that the equilibrium melting point is reduced. This phenomenon can be used to measure the pore size distribution by measuring the freezing point using DSC (Differential Scanning Calorimetry) or NMR (Nuclear Magnetic Resonance).

Water thermoporometry was performed on aerogels in several studies (Rousset et al., 1990; Ehrburger-Dolle et al., 1992; Rigacci et al., 1998). A typical result is shown on Figure 2-18.

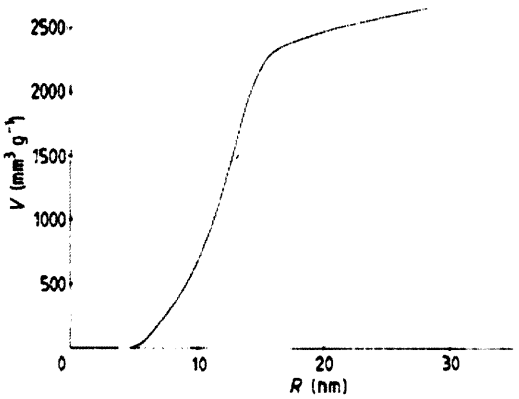

Figure 2-18: Cumulated porous volume against the pore radius obtained from thermoporometry (Rousset et al., 1990)

This method is highly successful for rigid materials, but it also exerts stresses on the network, so it is less reliable for compliant materials. Rousset et al.(Rousset et al., 1990) report that 27% of the total volume is not detected (this percentage grows to 50-60% in Rigacci et al.) and attribute it to the macropores (thermoporometry does not allow observations of pores with a radius larger than 400 Å). This interpretation has been refuted by Scherer (Scherer, 1998), who attributes it to the volume shrinkage during investigation.

Permeability

One method that is satisfactory for measuring the characteristic pore size of a network is permeability(Scherer, 1998). The permeability is controlled by the breakthrough radius, r_{BT}. This is the same characteristic size obtained from the inflection point of a mercury intrusion or nitrogen desorption curve, and it represents the critical pore size controlling entry into a percolating network of the largest pores.

A direct test of this idea has been made in the following way: r_{BT} was calculated from permeability measurements made on wet gels, then the gels were supercritically dried and the aerogels were examined by nitrogen desorption; the values of r_{BT} were found to be in good agreement. Measurements of this kind indicate that r_{BT} is 15 nm for silica gels containing >6 vol% solids. If there were a substantial fraction of macropores i.e. constituting 20% of the pore volume, then those pores should percolate and dominate the permeability, but that is not the case.

2.2.3 Scattering Techniques

SAXS (Small Angle X-Ray Scattering) (Borne et al., 1995; Schaefer and Keefer, 1986; Emmerling and Fricke, 1992) and SANS (Small Angle Neutron Scattering) (Vacher et al., 1988; Reidy et al., 2001) have been extensively used to study the fractal structure of the aerogel network. Low-angle scattering methods are valuable non-contact methods, yet they yield only general features of the network structure, not including a pore size distribution.

The typical arrangement of a scattering experiment is shown in Figure 2-19. The specimen is irradiated by monoenergetic photons (light, X-rays) or particles (neutrons). Part of this incoming primary beam is scattered as a result of the inhomogeneity of the sample.

We then consider the scattering wavevector

$$\vec{q} = \vec{k}' - \vec{k}$$

where $\vec{k}$ and $\vec{k}'$ are the wave vectors of the impinging and the scattered photon (neutron) respectively. In case of elastic scattering the absolute values of $\vec{k}$ and $\vec{k}'$ are unchanged ($|\vec{k}| = |\vec{k}'| = \frac{2\pi}{\lambda}$, λ being the wavelength). If, in addition, the structure is statistically isotropic, the scattering intensity depends only on the absolute value of the scattering vector:

$$q = \frac{4\pi}{\lambda} \sin \frac{\theta}{2}$$

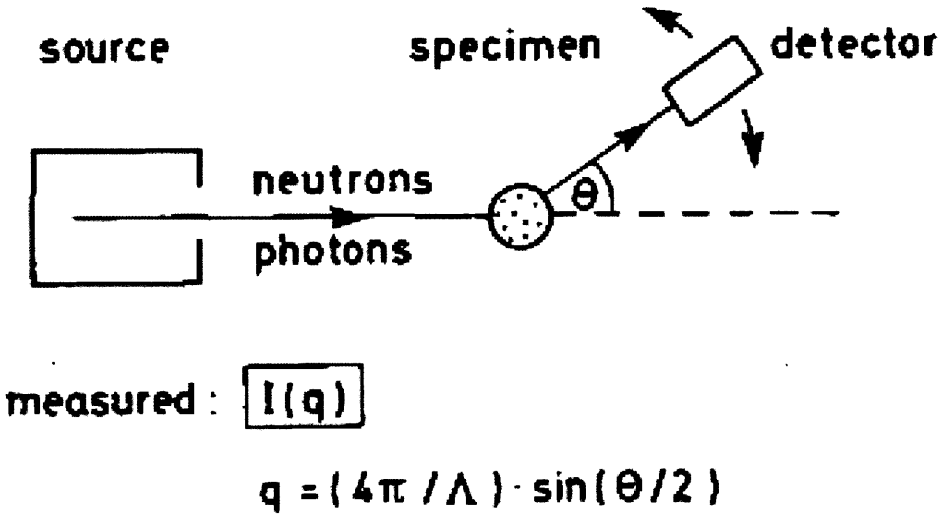

Figure 2-19: Representation of a scattering experiment, from (Emmerling and Fricke, 1992). Due to inhomogeneities of the sample, part of the monochromatic collimated beam of photons (or neutrons) is scattered. The angular distribution of scattered intensity is recorded either sequentially with a point-like detector (as drawn), or in parallel using a position-sensitive detector system.

whereby θ denotes the scattering angle. The structure in real space and the scattering observed in q-space are connected by a Fourier transformation; however, a simple back transformation cannot be performed, since only the intensity, but not the phase shift of the beam is measured. For a first order approximation, for every value of q a corresponding length scale, L, can be defined via Bragg's law ($qL = 2\pi$).

Typical wavelengths are 1-2 Å in X-ray and 2-10 Å in neutron experiments; these wavelengths are smaller than the structural sizes of 1 to 100 nm to be probed. Thus the scattered intensity has to be detected at small scattering angles (0.01° - 10°) close to the primary beam.

Figure 2-19 shows a typical curve of a disordered material, consisting of a network of particles. Different regimes can be observed. The transitions give rough information about the structural features sizes (larger aggregates, particles).

Assumptions for the intensity $I(q)$ based on the fractal formalism can explain the power-law behavior of the scattered intensity for small q. In the range $\frac{1}{R} < q < \frac{1}{r}$, the intensity has a very simple form $I(q) \propto q^{-D}$ where D is the mass fractal dimension ($D = 3$ for a simple body). At large intensity ($q \gg \frac{1}{r}$) another power law is observed: $I(q) \propto q^{D_S - 6}$, where D_S is the surface fractal dimension ($D_S = 2$ for a smooth body). The position of the two transitions between the two power-law regions occur near $q_R = \frac{1}{R}$

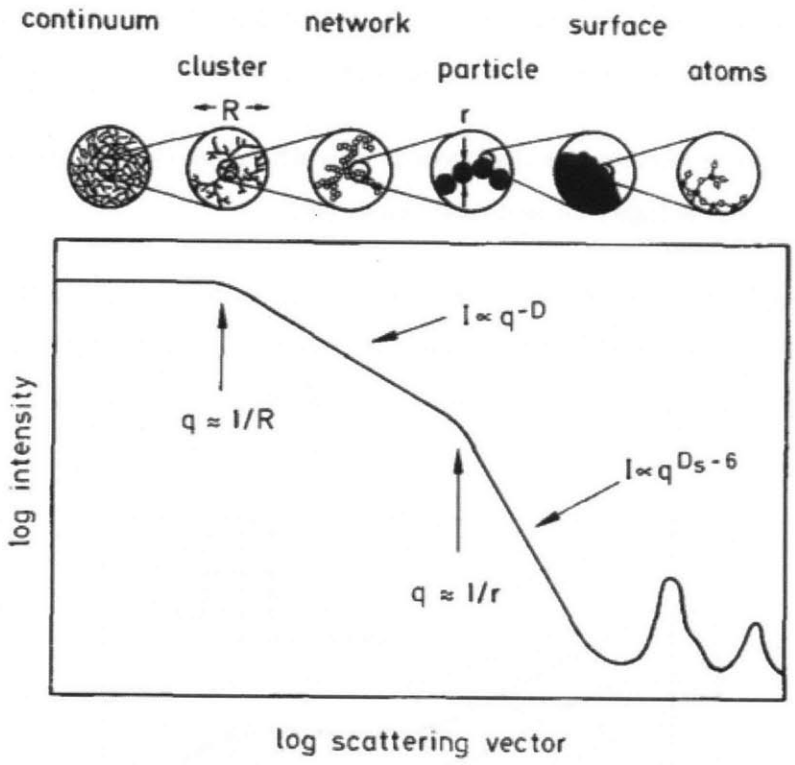

Figure 2-20: Typical small angle scattering intensity of a particle network such as aerogel, from (Emmerling and Fricke, 1992)

and $q_r = \frac{1}{r}$, furnishing information on the size of the structural features.

In addition to these values, which can be directly obtained from the scattering curves, further information becomes available, if a two-phase media model is applied. The porous body is assumed to consist of two phases with constant mass density: the solid phase with a mass density ρ_S and the voids (with density 0). Under this assumption, the mean chord length of each phase can be derived. Fractal analysis can also be used.

The particle diameter is found to be 4.5 to 7 nm (Emmerling and Fricke, 1992). No correlation exists between density and particle diameters; the latter are mostly pH-dependent. The mean free path within the aerogel network shrinks (from 150 to 50 nm) with increasing density.

The observation of power laws confirm that aerogels have self-similar (fractal) geometry. It is found that the self-similarity range is higher for acid catalysed aerogels.

More recently, USAXS (Ultra-Small Angle X-Ray Scattering) has been used to study bigger features of the aerogels (Marlière et al., 2001). It has been found another transition in the scattering curves, indicating another characteristic size of features around 100 nm (Figure 2-21), in accordance with direct observations.

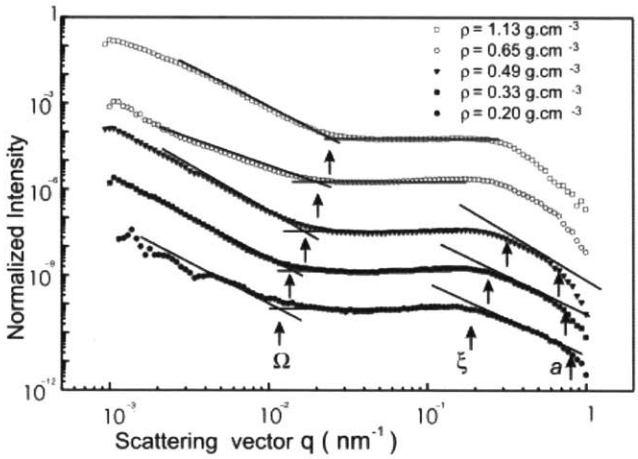

Figure 2-21: USAXS normalized intensity as a function of wave vector (Marlière et al., 2001). The left part with the transition at Ω has been specifically revealed by USAXS.

2.3 Aerogel mechanical properties

2.3.1 Introduction

Mechanical properties of aerogels have long been seen as one of the obstacles to a widespread use of aerogel as insulating materials, along with the cost. Indeed, insulating materials have to be handled easily in order to be installed, and one cannot afford to regularly break aerogel panels because of excessive brittleness. We present a review of the mechanical studies of silica aerogels in the literature. The number of these studies is relatively low compared to the emphasis given to the structure. Great interest has been shown in these studies to the scaling of the mechanical properties with density.

The mechanical behaviour of aerogels is generally described in terms of brittle and elastic materials, like glasses or ceramics. The main difference compared to silica glass is the order of magnitude of the elastic and rupture moduli, which are 10^4 times lower for aerogels. However, if this analogy is pertinent when gels are under a tension stress (bending test) they exhibit a more complicated response when the structure is submitted to a compressive stress (Woignier et al., 2000).

2.3.2 Elastic and plastic behaviour of aerogels

Bending test

The bending test is the easiest mechanical test to perform on silica aerogels, usually by 3-point bending (Woignier et al., 1987; Woignier et al., 1998; Alaoui et al., 2008). Under 3-point bending, the stress-strain curve is purely linear until the failure, as seen on Figures 2-22 and 2-23.

The Young's modulus is derived from the slope of the load-deflection line:

$$E = \frac{PL^3}{12\pi\delta r^4}$$

where P is the applied load, L the span between the two supports, δ the measured displacement and r the radius of a cylindrical sample.

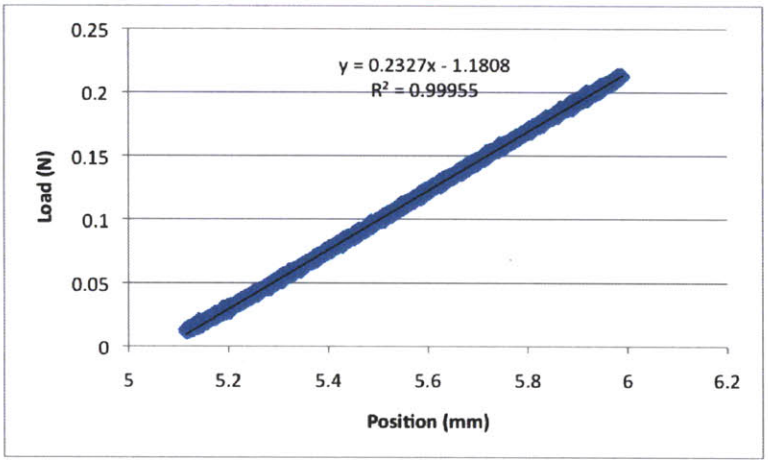

Figure 2-22: Bending test of one our samples with linear fit. We calculate E=0.62 MPa

Alaoui et al. (Alaoui et al., 2008) state that indentation occurs at the point of contact with the pushrod for the cylindrical samples they use. This must be taken into account to get an accurate measure of the elastic modulus. For the geometrical condition they use, the error in E from indentation is $<10\%$.

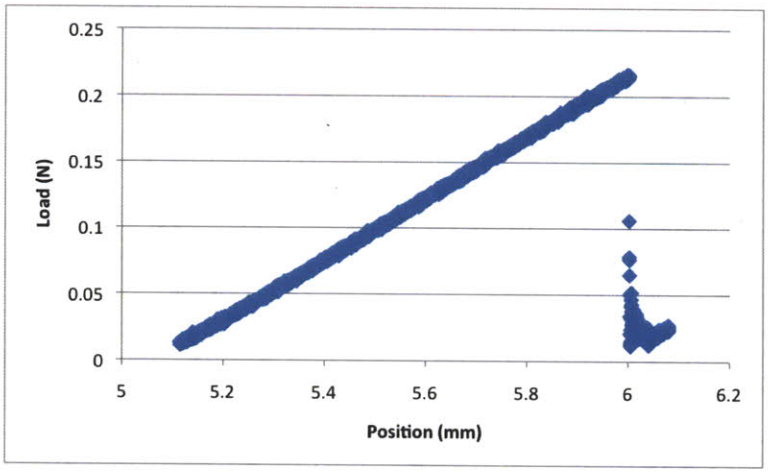

Figure 2-23: Bending test of one our aerogels up to failure; the behavior remains linear until failure (at 31 kPa, 5%)

Compression test

Uniaxial compression tests have been performed on silica aerogels by Gross et al. (Gross et al., 1988), Alaoui et al. (Alaoui et al., 2008). Typical stress-strain curves are plotted on Figures 2-24 to 2-26.

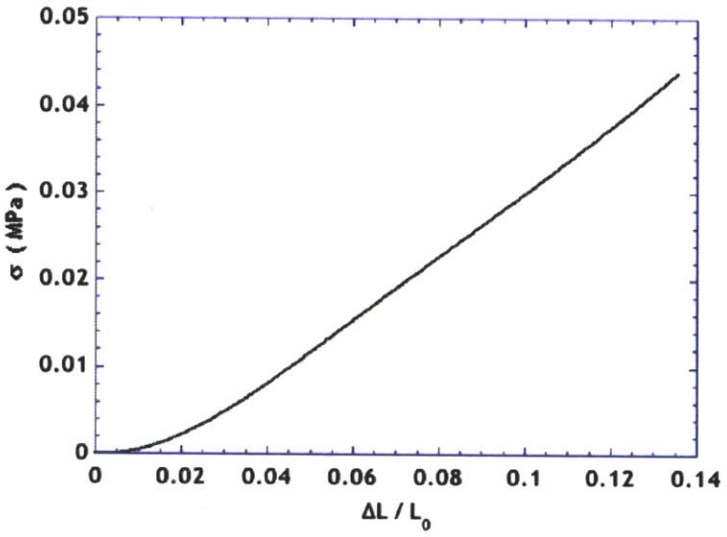

Figure 2-24: Stress versus strain curve showing reversible deformation of an aerogel under uniaxial compression (Alaoui et al., 2008)

In their study, Alaoui et al. find that the elastic modulus given by the uniaxial compression test is lower than that given by bending tests because of geometrical effects such as misalignment. They

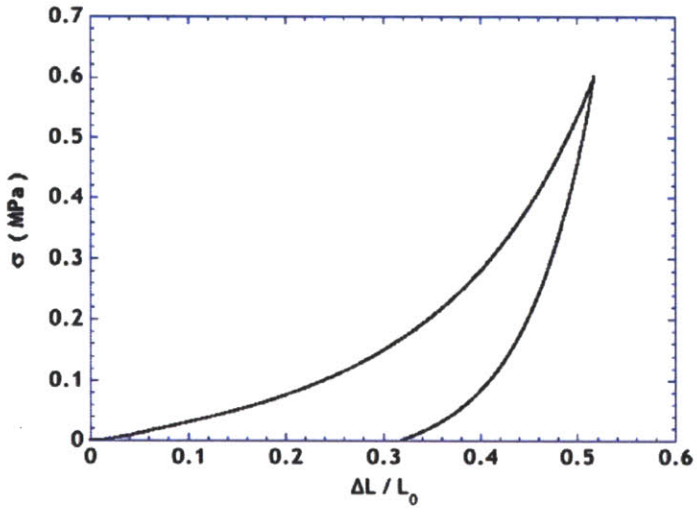

Figure 2-25: Stress versus strain curve showing irreversible deformation of an aerogel under uniaxial compression (Alaoui et al., 2008)

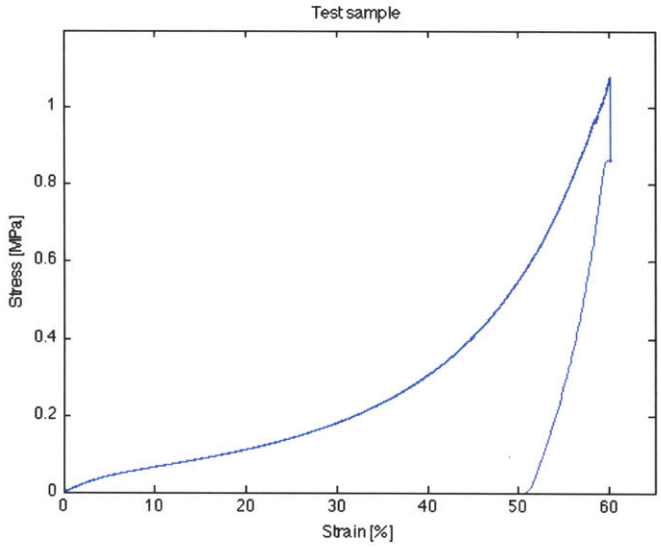

Figure 2-26: One of our samples in uniaxial compression up to failure and the unloading of the partially broken sample

propose a way of correcting the data. The uniaxial compression also gives an underestimated value of the exponent in scaling properties (see below).

The reason for underestimating the Young's modulus could be the presence of defects. Indeed, in the case of a compressive test, the defects will see the same load anywhere in the sample. Thus, all defects will weaken the sample. However, in the case of a bending test, only the defects located on the curved edges will have an effect. The defects near the neutral axis of the beam see no stress and thus have no effect on the overall Young's modulus.

Isostatic pressure test

Mercury porosimetry has also been found to give information on the mechanical properties of aerogels since the aerogel is submitted to isostatic compression before the mercury can intrude the pores. Bulk modulus can thus be derived from mercury porosimetry experiments. By fitting the results, Scherer et al. (Scherer et al., 1995a) find a power law for the bulk modulus, which they define by $dP = -K\frac{dV}{V}$ (P is the pressure applied isostatically and V the resulting volume). Pirard et al. (Pirard et al., 1995) showed that the crushing process is clearly irreversible (see Figure 2-27). The notation "K" and the term "bulk modulus" are thus to be used with caution since they usually refer to elastic (reversible) properties.

$$K(V) = \begin{cases} K_0 & \text{if } V \leqslant V_y \text{ where } V_y \text{ is a threshold volume depending on the sample based on curve-fitting} \\ K_0(\frac{V_y}{V})^m & \text{if } V \geqslant V_y \end{cases}$$

which can also be written in terms of the density of the sample during the test (the density increasing while the sample is compressed):

$$K(\rho) = \begin{cases} K_0 & \text{if } \rho \leqslant \rho_y \text{ where } \rho_y \text{ is the density corresponding to } V_y \\ K_0(\frac{\rho_y}{\rho})^m & \text{if } \rho \geqslant \rho_y \end{cases}$$

So, the aerogel is Hookean (linear stress-strain behavior) at small strain and then follows a power law as a function of volume (related to the strain) at some point.

They proposed a mechanism for the crushing of aerogels: the framework would be destroyed by lateral

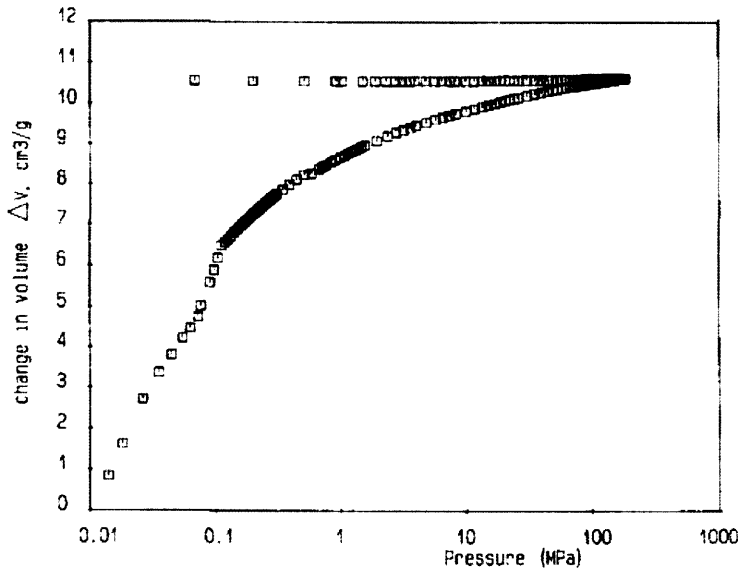

Figure 2-27: Mercury porosimetry curve, volume versus pressure, of af an aerogel sample crushed by mercury porosimetry (Pirard et al., 1995)

collapsing of the edges at a pressure P. This pressure would follow the Euler buckling law:

$$P = \frac{K}{L^4} \text{ where K is a constant for a given material and L the characteristic pore size}$$

Then they compare this mechanism to two others (axial crushing of the edges and intrusion of the mercury, see Figure 2-28) and show by plotting the pore size against the mercury pressure, that the mechanism they suggest fits the data better, Figure 2-29.

Another study (Pirard and Pirard, 1997) has suggested a theoretical model based on a hierarchical model; they consider different levels of pore size, progressively being crushed, starting with the largest ones as pressure increases. This model gives a relation between the pore size distribution and the correlation between the bulk modulus K and the bulk density ρ.

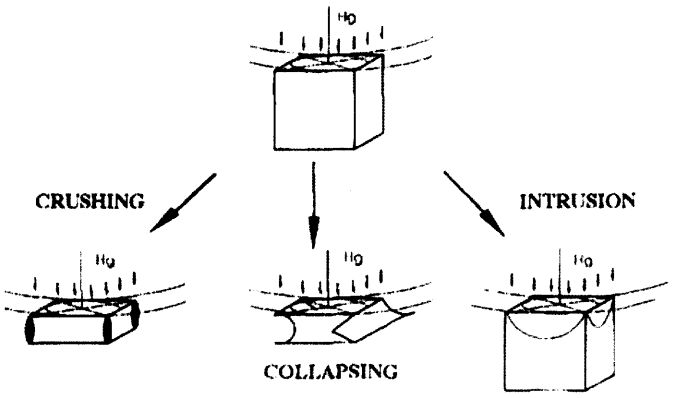

Figure 2-28: Schematic view of the three models considered for the volume variation of a network of cubic pores such as aerogel, by (Pirard et al., 1995)

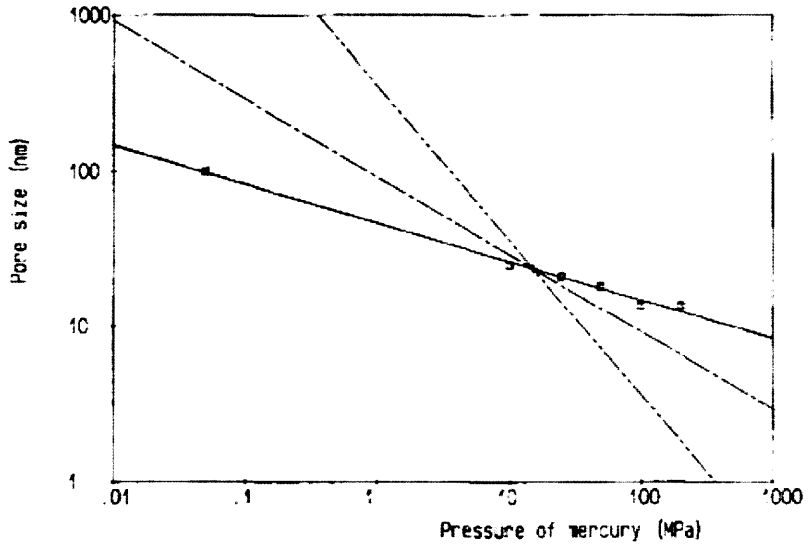

Figure 2-29: Size of the largest pore L_{max} versus compaction pressure P due to mercury: (□) experimental point, (—) regression line, (– – –) collapse law, (– – · – – ·) axial crushing law and (– – ·· – – ··) Washburn's intrusion law. Note that the regression curve is superimposed on the collapse law (Pirard et al., 1995)

Ultrasonic sound velocity

Another technique widely used for determining aerogel elastic modulus is the measurement of ultrasonic sound velocity in the material (Gross et al., 1988; Gross et al., 1992). The ultrasonic experiments are a non-destructive method that allows the Young's modulus E and the Poisson's ratio ν to be determined.

Indeed, the longitudinal sound velocity c_l in an isotropic material is related to E and ν by

$$c_l = \sqrt{\frac{E(1-\nu)}{\rho(1+\nu)(1-2\nu)}}$$

and the transverse velocity c_t is given by

$$c_t = \sqrt{\frac{E}{2\rho(1+\nu)}}$$

The measurement of both velocities allows calculation of E and ν. In particular, it is found that the Poisson's ratio ν is approximately constant in silica aerogel, independent of density, close to the Poisson's ratio for silica glass ($\nu \simeq 0.23$):

$$\nu \simeq 0.2$$

Gross et al. (Gross et al., 1988) compare their results obtained by acoustic measurements with uniaxial compression tests. The acoustic Young's modulus is found to be lower than the uniaxial Young's modulus at low density, and higher at higher densities. This is in accordance with the results of Alaoui et al. (Alaoui et al., 2008) who find lower exponent for the Young's modulus as function of density in uniaxial compression tests compared to bending tests.

Microindentation tests

Classic indentation tests (Vickers and Knoop indentation) have been attempted (Parmenter and Milstein, 1998), but failed because the indentation pressure was too large for these fragile materials and resulted in cracks in the surface.

Microindentation has been performed on silica aerogels by Moner-Girona et al. (Moner-Girona et al., 1999). They use a technique that enables the continuous measurement of load-displacement curves during loading and unloading cycles by using very small indentation loads (~1 mN). This load is small enough to prevent crack formation.

Indentation was performed on the lateral surface of cylindrical rods (see Figure 2-30), with maximum penetration depths in the range 2 - 7 μm. The Young's modulus is then obtained from the analysis of the unloading curve. The values obtained follow the scaling law against density as shown in next subsection, however the values seem to be somewhat higher than those obtained from more usual tests, in the range 7 - 346 MPa (for a density in the range 0.08 - 0.26 g/cm^3).

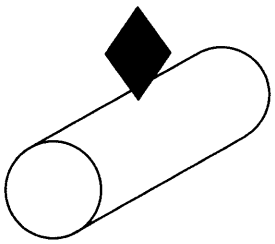

Figure 2-30: Indentation on the lateral surface of cylindrical rods

2.3.3 Scaling Properties

Woignier et al. (Woignier et al., 1989) and Pekala et al. (Pekala et al., 1991) have shown that for aerogels prepared under the same conditions but with various densities, one could observe a scaling between Young modulus and density. It is found that the Young modulus of a set of aerogels is related to the density by

$$E \propto \rho^m$$

The exponent m is higher than the exponent established for an open-cell foam model, $m = 2$ (Gibson and Ashby, 1997). With the exception of one study, all the studies reviewed here give exponents between 3.1 and 3.7.

Data gathered from several sources are plotted together on Figure 2-31, and a general power law fit is given on Figure 2-32.

However the Young modulus is also found to depend on other characteristics than density, for example the pore size and the microstructure, these characteristics depending themselves on formation conditions like the pH of the catalyst. The acid-catalysed aerogels are found to be stiffer (about 7 times stiffer) than the base-catalysed ones (Pekala et al., 1991).

These exponents can be compared with the theory for open-cell foams:

$$E \propto \rho^2 \text{ (Gibson and Ashby, 1997)}$$

The exponents for aerogels are far above this value of 2, meaning the aerogels are going to be orders of magnitude more compliant than foam-like materials.

Emmerling and Fricke (Emmerling and Fricke, 1997) suggest an approach using the mass fractal dimension D derived from SAXS experiments. Assuming the major deformation mechanism is bending (as seen prevously in the work of Pirard et al. (Pirard et al., 1995)), they find:

$$\frac{E}{E_S} \propto \left(\frac{\rho}{\rho_S}\right)^{\mu}, \text{ with } \mu = \frac{5-D}{3-D}$$

For example, for $D \simeq 1$, one finds $\mu \simeq 2$. Figure 2.3.3 shows good agreement between theory and experiment.

However, Woignier et al. (Woignier et al., 1998) have found different exponents for samples of same

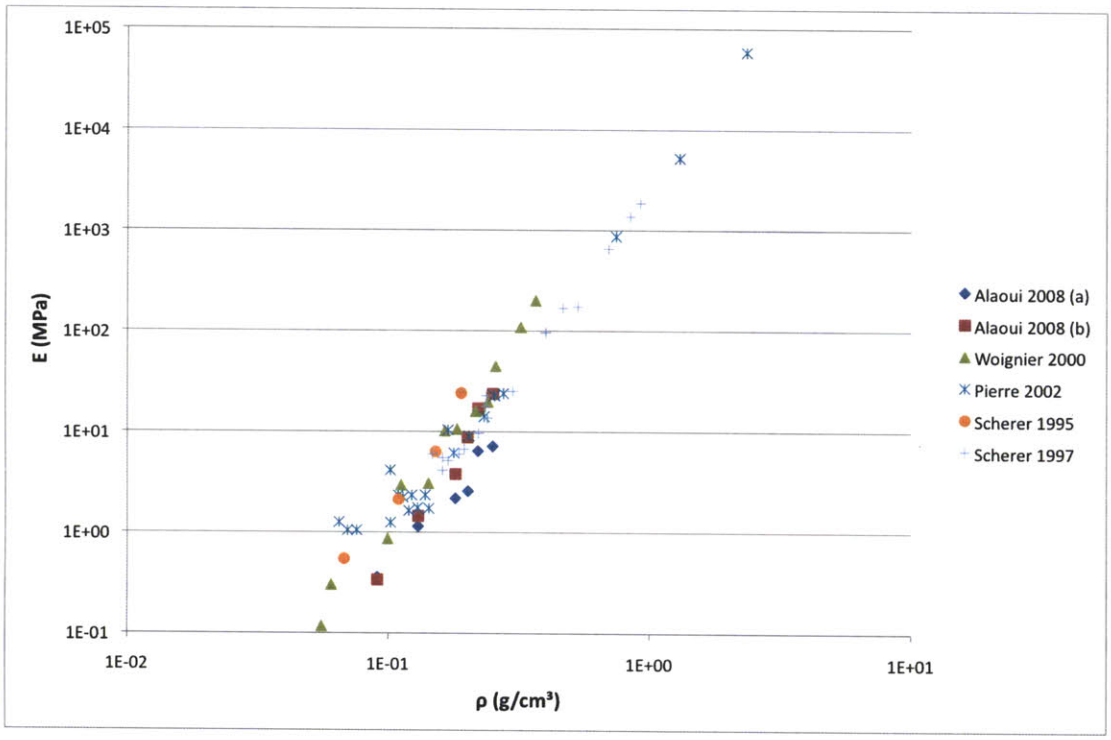

Figure 2-31: Data for the Young modulus against the density (log-log plot) obtained in (Alaoui et al., 2008; Woignier et al., 2000; Pierre and Pajonk, 2002; Scherer et al., 1995a; Scherer, 1997) for silica aerogels and some denser silica compounds

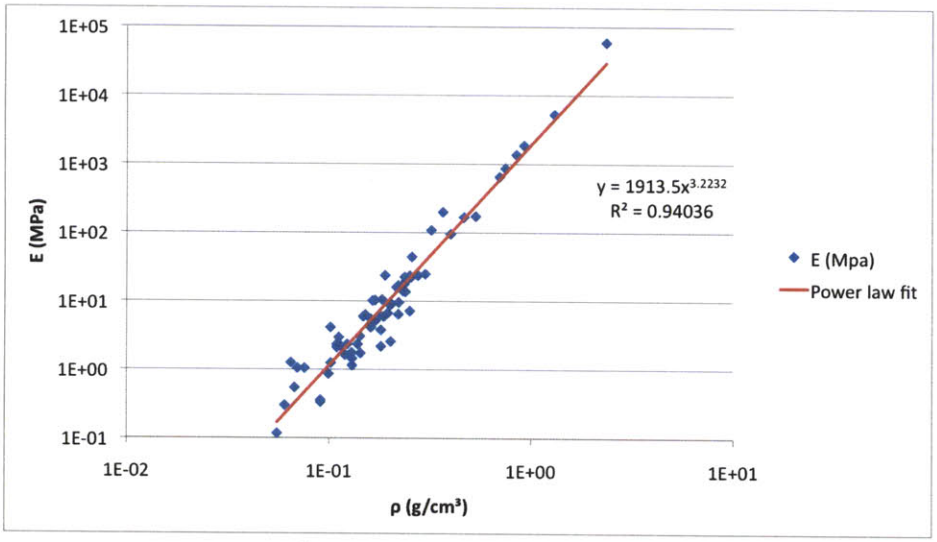

Figure 2-32: Power law fit for the whole set of data. We find an overall exponent of 3.2

Table 2.1: Comparison between $\mu(D)$ and μ_{exp} (Emmerling and Fricke, 1997)

Table 2. **Mass fractal dimension D and the resulting theoretical scaling exponent $\mu(D)$ as well as the experimentally derived scaling exponent μ_{exp} of the elastic modulus for different aerogel series.**

Aerogel sample series	D	$\mu(D)$	μ_{exp}
Resorcinol-formaldehyde [20]	1.75 ± 0.12	2.60 ± 0.15	2.44 ± 0.16
Two-step silica [20]	1.80 ± 0.05	2.67 ± 0.07	2.59 ± 0.10
Carbon [20]	1.80 ± 0.10	2.67 ± 0.14	2.69 ± 0.05
Base-catalyzed silica [20]	2.00 ± 0.08	3.00 ± 0.16	2.95 ± 0.15
Sintered silica [20]	2.20 ± 0.15	3.50 ± 0.47	3.40 ± 0.25
Neutrally reacted silica [18]	2.30 ± 0.10	3.86 ± 0.41	3.70 ± 0.10

fractal dimension (obtained by densification of an initial sample). They conclude that cluster features such as fractal dimension have no influence on the exponent, the major parameter, according to them, being the connectivity between clusters.

2.3.4 Strength

The major limitation of aerogels as insulating materials is their high brittlness. Therefore, it is necessary to have data on the mechanical strength of aerogel in order to understand and improve it. Very few studies have focused on this.

Woignier and Phalippou (Woignier and Phalippou, 1988) have done a study on the strength of silica aerogels with either flexural tests or Brazil tests. The mechanical bending test shows a perfect elasctic behaviour followed by a catastrophic failure. The conchoidal fracture morphology indicates that the material is brittle as a conventional glass.

The results of some studies on the mechanical strength of aerogels are plotted together in Figure 2-33. We see that we obtain again a power law for the strength against the density. The exponents are similar but large differences are found in absolute value between differents sets of aerogels. The exponents are generally found to be lower than those for the Young modulus, between 2.6 and 3, see the combined plot on Figure 2-34. This again is above the value found for open cell foams, where the brittle crushing strength is given by

$$\sigma_{comp} \propto \rho^{\frac{3}{2}} \text{ (Gibson and Ashby, 1997)}$$

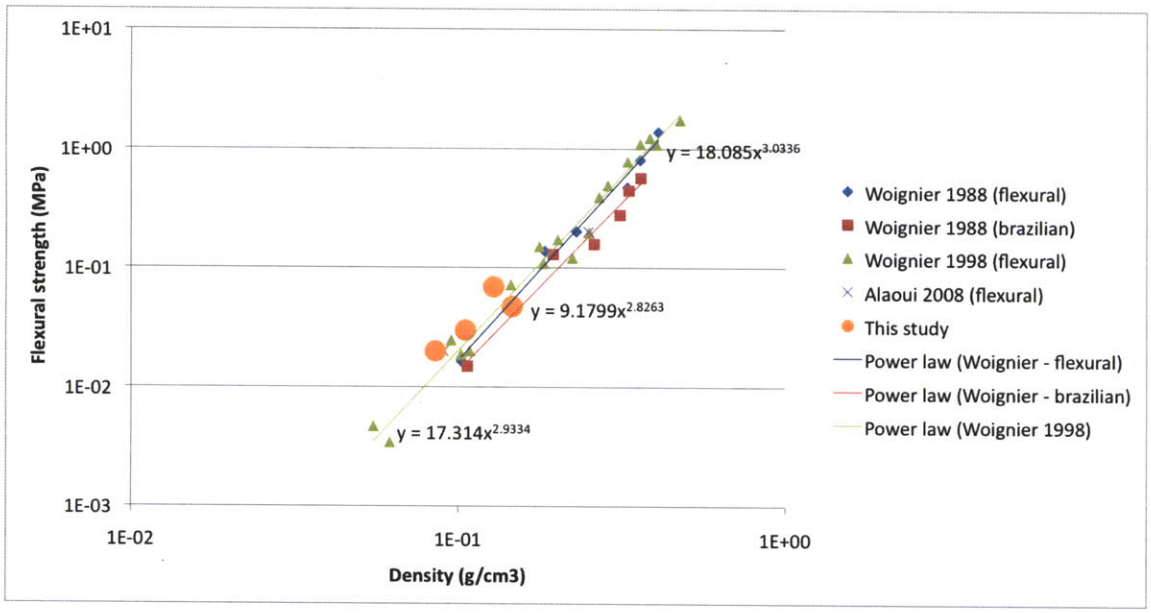

Figure 2-33: Data for the strength against the density obtained in (Woignier et al., 1998; Alaoui et al., 2008; Woignier and Phalippou, 1988)

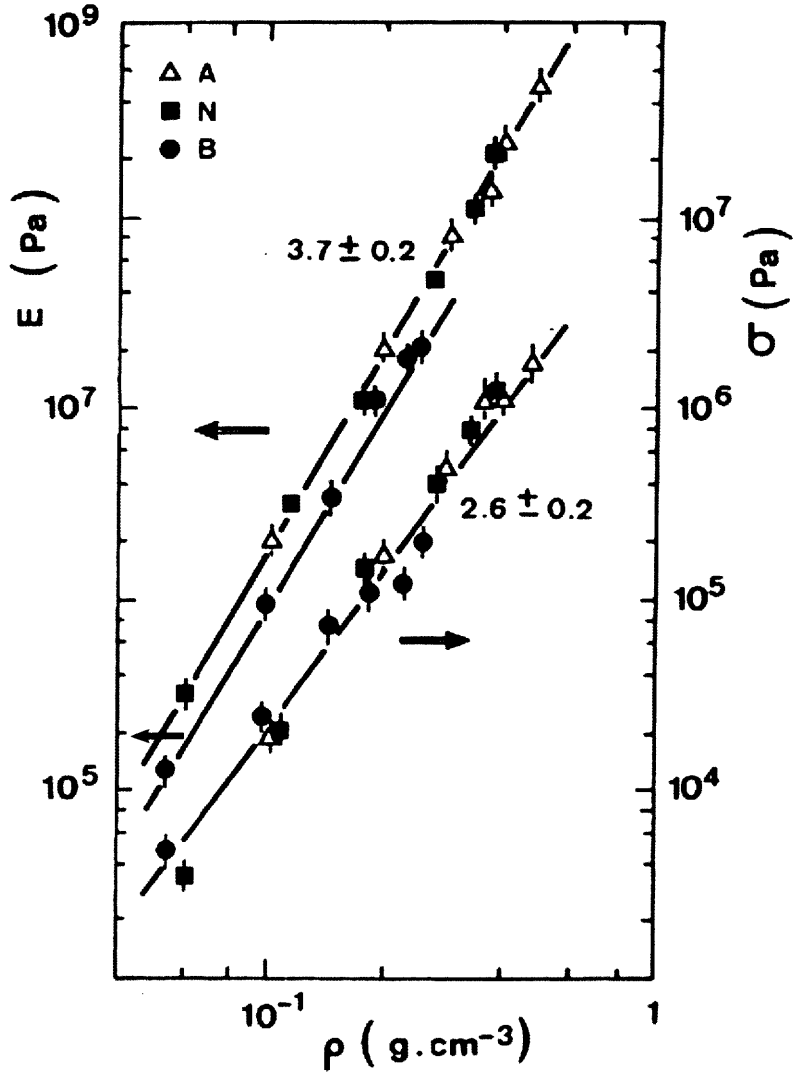

Figure 2-34: Combined plot of Young modulus and flexural strength for three sets of aerogels, acid (A), neutral (N) and basic (B) (Woignier et al., 1998)

Parmenter and Milstein (Parmenter and Milstein, 1998) have also made a study of the mechanical properties of silica aerogels, including strength. Most of their results investigate the influence of fiber reinforcements in the aerogel.

2.3.5 Fracture Toughness

The toughness can be measured using the single edge notched beam technique in 3 point bending. In their study, Phalippou et al. (Phalippou et al., 1989) use a diamond saw of 50 μm width to make the notch on a parallelepipedic sample; the notch depth C lies between 0.25W and 0.3W where W is the sample width. In such a configuration, the value of K_{IC} is given by

$$K_{IC} = \frac{3Pl}{2W^2d}\sqrt{C}Y$$

where P is the load necessary to break the specimen, d is the width and Y is a polynomial expression depending on the W value.

The toughness has also a power-law relationship with density (Woignier et al., 2000; Phalippou et al., 1989), see Figure 2-35 :

$$K_{IC} \propto \rho^l$$

The value of the exponent l is generally found between 1.6 and 1.7. This value is similar to that for models for the fracture toughness of an open cell foam, where the exponent is 1.5 (Gibson and Ashby, 1997).

From the fracture toughness we can derive a critical flaw size for catastrophic failure. Theory gives that this flaw size varies as the inverse of K_{IC}^2. Experiment shows that it follows the size change of the largest pores (see Figure 2-36).

The critical flaw size is larger than the pore size, so the critical crack extends over a number of pores. The failure occurs therefore by progressive bond breaking.

Because of the stress corrosion effect, a monolithic gel can crack several days or months later under a low stress, particularly under humid conditions.

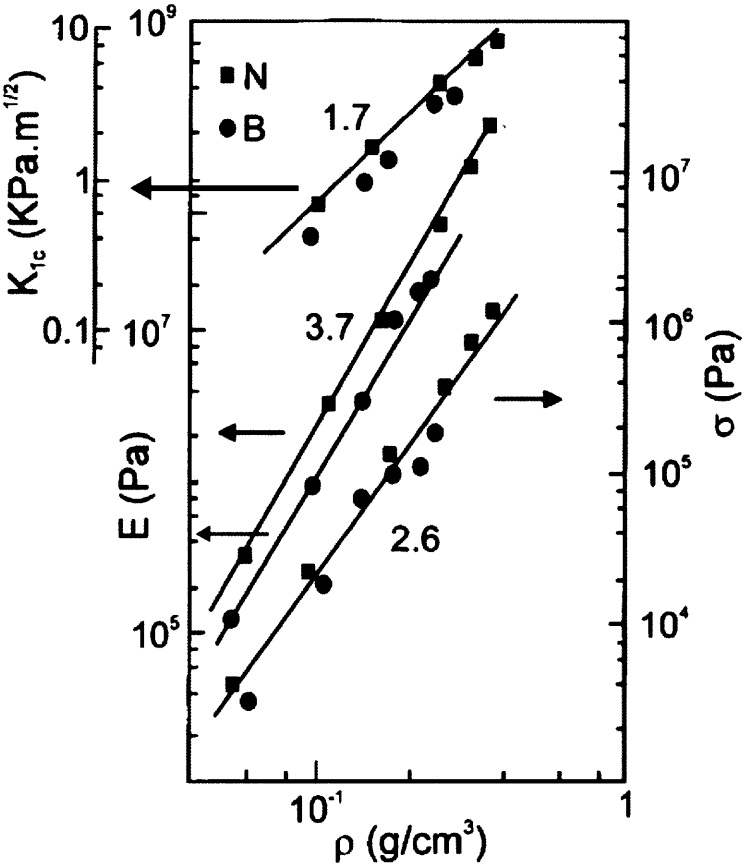

Figure 2-35: Evolution of the mechanical properties as a function of the bulk density for a set of of neutral-catalysed (N) and base-catalysed (B) aerogels (Woignier et al., 2000)

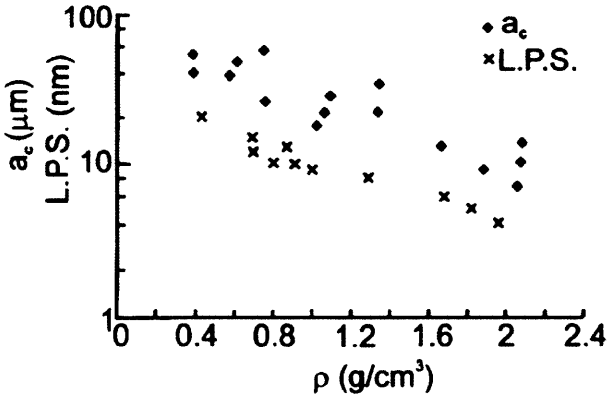

Figure 2-36: Evolution of critical flaw size (a_c) and larger pore size (L.P.S.) as function of the density (Woignier et al., 2000)

2.3.6 Effect of age

Parmenter and Milstein (Parmenter and Milstein, 1998) studied the effect of age on the mechanical properties of aerogels. Figure 2-37 indicates that the aging process tends to increase elastic moduli, while decreasing the strain at fracture, and not significantly affecting the compressive strength. Therefore, the toughness decreases and specimens become more brittle with age.

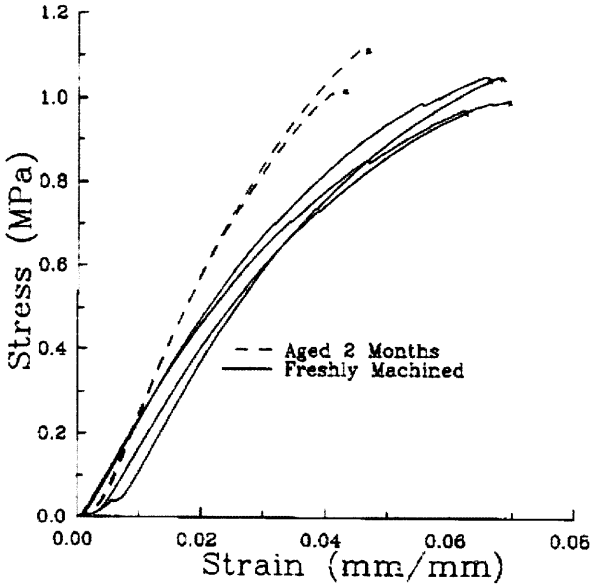

Figure 2-37: Comparison of stress-strain curves for freshly machined specimens and specimens aged in air for 2 months (Parmenter and Milstein, 1998)

2.4 Aerogel mechanical properties modeling

2.4.1 Introduction

The results of the previous section all come from empirical observations but do not relate aerogel mechanical properties to its inner structure. Modelling tools are required to try to explain, for example, the exponent that appears in the relationship between density and Young's modulus.

Two methods are used in simulation of aerogels:

- Simulation of the gelation process. The goal of these simulations is to reproduce the actual process of aggregation of particles during synthesis. These simulations have been widely studied for all kinds of gels and not only aerogels.
- "Static" simulations. These simulations focus only on the final structure of aerogels and do not try to reproduce accurately the gelation process.

All these models are generally based on primary particles, usually spheres. In both cases, the results of the simulation can be used to study the mechanical properties of aerogels using finite element methods. Interestingly, the results on computed mechanical properties also gives a feedback on the simulated structure itself.

2.4.2 Simulating gelation

There have been numerous particle-based simulations of gelation, in general, and of the preparation of silica aerogels in particular. Many simulation studies have focused on aggregating hard spheres.

It is generally agreed that the cluster-cluster aggregation regimes (DLCA - diffusion limited cluster aggregation, RLCA - reaction limited cluster aggregation) describe quite well the typical structures obtained by sol-gel processing. The sol-gel process involves indeed the assembly of small particles to form clusters and networks.

The DLCA model, the most commonly referred to, was first introduced by Witten and Sanders (Witten and Sander, 1981) and then developed in its current form by Meakin (Meakin, 1983) and Kolb et al. (Kolb et al., 1983), all in two dimensions. The model is a growth model that describes the clustering of clusters. One starts with an assembly of Brownian particles which stick together upon contact to form rigid clusters. The newly formed clusters diffuse along with the particles and continue to grow by aggregation when they meet other clusters or particles. The result can be seen on Figure 2-38.

The actual calculation is performed on a periodic square lattice with $V = L^2$ sites with initially N_0 randomly distributed particles. Clusters (particles connected by nearest-neighbor bonds) are rigid and move randomly one lattice spacing at a time. Clusters do not rotate, which presumably does not affect critical properties. An example is shown on Figure 2-38. One can observe the chain-like appearance and few branchings in the cluster.

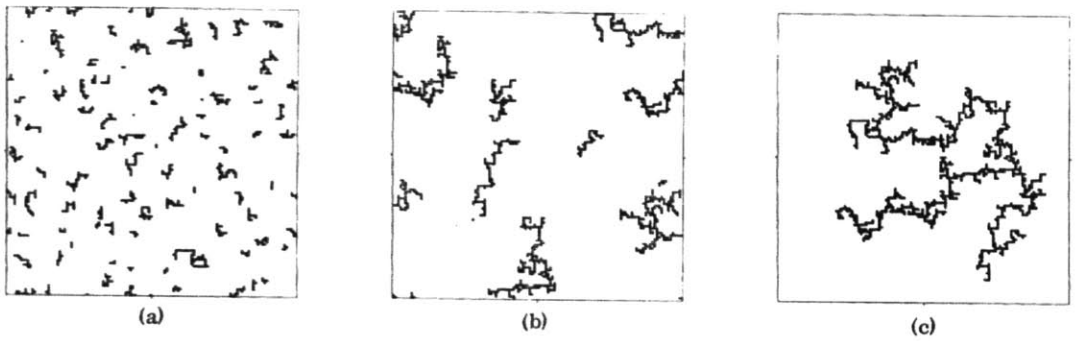

Figure 2-38: DLCA algorithm in two dimensions (Kolb et al., 1983). The three situations correspond to $N_C = 86$, 8 and 1 cluster, respectively. The system has a size $L = 128$ and initially $N_0 = 1024$ particles. Note the chainlike appearance and the few branchings of the clusters.

The model is easily extended to the third dimension with a cubic lattice. The DLCA process still begins with dispersion of particles (all of the same diameter) randomly in a three-dimensional cubic

lattice. The particles are allowed to diffuse randomly along the lattice connections. When they collide, they bond irreversibly and continue to diffuse as a dimer, trimer and so on, until one single cluster is left (Ma et al., 2000).

Further work (Botet et al., 1984) introduced the cluster-cluster model slightly differently in a hierarchical scheme, *ie* as an iterative method. It starts with $N_p = 2^p$ identical spheres and ends with a unique aggregate of N_p particles. At an intermediate iteration, one has a collection of 2^{p-i} aggregates, each containing $N = 2^i$ particles. To go to the next iteration, pairs of aggregates are randomly formed to build a new aggregate (see on figure 2-39) according to specific sticking rules. The authors affirm that the numerical precision is better due to the simpler (hierarchical) formulation, and that the results are similar to previously described method of (Kolb et al., 1983).

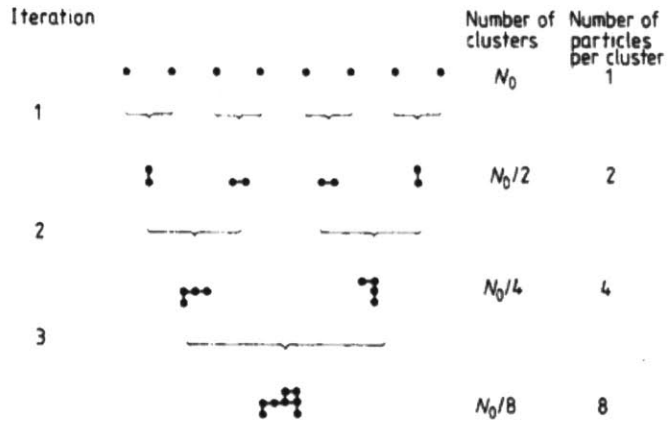

Figure 2-39: Sketch of the hierarchical model (Botet et al., 1984)

The sticking rule is similar to the original DLCA model. One cluster, say cluster 1, is centered at the origin of a square lattice. The other one, cluster 2, is released at a point chosen at random on a large circle of radius R_0 centered at the origin. Then cluster 2 undergoes a random walk on the lattice, jumping by one lattice spacing at each step. In this motion the cluster stays rigid and does not rotate. The random walk stops when one particle of cluster 2 becomes the nearest neighbour of one particle of cluster 1 and then a cluster of the new generation is formed by the reunion of clusters 1 and 2. If cluster 2 goes too far away from cluster 1, at a distance R_m, it is released again on the circle and this is done as often as it is necessary. One should note that, contrary to the model described above, the cluster is not built on a lattice since even if the random movement is on a lattice, the initial coordinates of cluster 2

relative to cluster 1 are not.

Other aggregation mechanism have been studied, such as RLCA - reaction limited cluster aggregation. The sticking rule is modified as follows (Hasmy et al., 1993): A particle of cluster 1 and a particle of cluster 2 are chosen at random as well as a random direction in space. The two randomly chosen particles are brought into contact along the randomly chosen direction. If other particles in the two clusters overlap, then the trial is discarded and another choice is made both for the particles and random direction. Results are quite similar to the DLCA model, the fractal dimension being however slightly higher.

In three dimensions, restructuring schemes can also be considered (Hasmy et al., 1993). Cluster 2 is rotated around one (or more) random axis going through one contact particle until another contact occurs between the two clusters. Effects of this restructuring are shown on Figure 2-40. Drastic compaction can be observed. This compaction being limited to short distances, the fractal dimension is not dramatically changed.

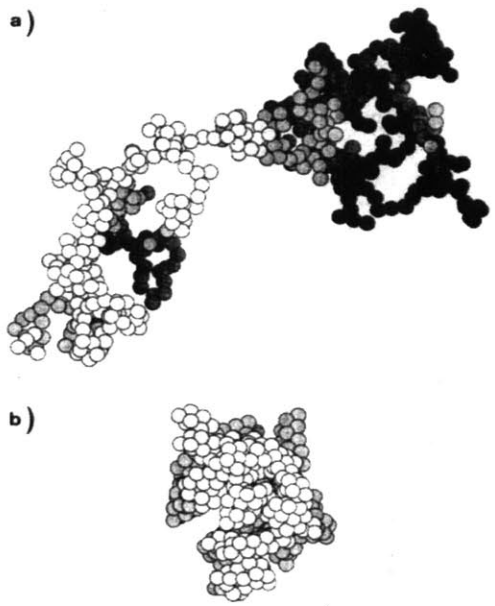

Figure 2-40: (a) Three-dimensional aggregate containing 4096 spherical particles without restructuring. (b) Same as (a) but with complete restructuring. (Hasmy et al., 1993)

Hasmy et al. (Hasmy et al., 1993; Hasmy et al., 1994) were the first to specifically apply the cluster-cluster model to aerogels. They show that the model accounts well for the fractal behavior of aerogels

by comparing simulation and experiments of small-angle neutron scattering (see section 2.4.4). Ma et al. (Ma et al., 2000; Ma et al., 2001; Ma et al., 2002) have applied it in order to investigate the mechanical properties (see in section 2.4.5).

Further studies have tried to model the interaction between the gel particles more realistically during the gelation process. Gelb use a more advanced model specifically for aerogels (Gelb, 2007). The so-called "flexible coarse-grain model" represents silica particles by smooth spheres interacting in two ways: *via* a very weak nonbonding two-body potential of the shifted-center Lennard-Jones form, and via short, stiff bonds. The bonds are created with a given probability P when two spheres are in contact. Bond breakage is also possible. The bonds are not completely rigid, and have also an associated potential, and the clusters are thus flexible. This allows for the effects of relaxation and fluctuations on gel structure that may be expected to play a role in the formation of even the most rigid gels. For simulation of gelation and gel aging, a stochastic dynamics approach is used, in which the solvent is modeled simply as a field that exerts fluctuating forces and drag on the gel particles. The results are different from the DLCA model, especially with a different fractal dimension (depending on the probability P) that may be due to the flexibility of the model. Examples of the simulated structures are shown on figure 2-41. Parameterization of the model is nontrivial, the choices are qualitative or semi-quantitative but do not look for reproducing exactly molecular behavior.

These works are focused on simulating the gelation process, the underlying assumption in using it for aerogels is thus that the drying process does not significantly modify the structure.

The primary particle used in the methods can be given any physical meaning in the self-similar (fractal) range. All the simulations are anyway non dimensional. Usually, the elementary particles are considered as the smallest homogeneous particles that can be seen on micrographs, in the range of 100-200 Å for colloidal aerogels.

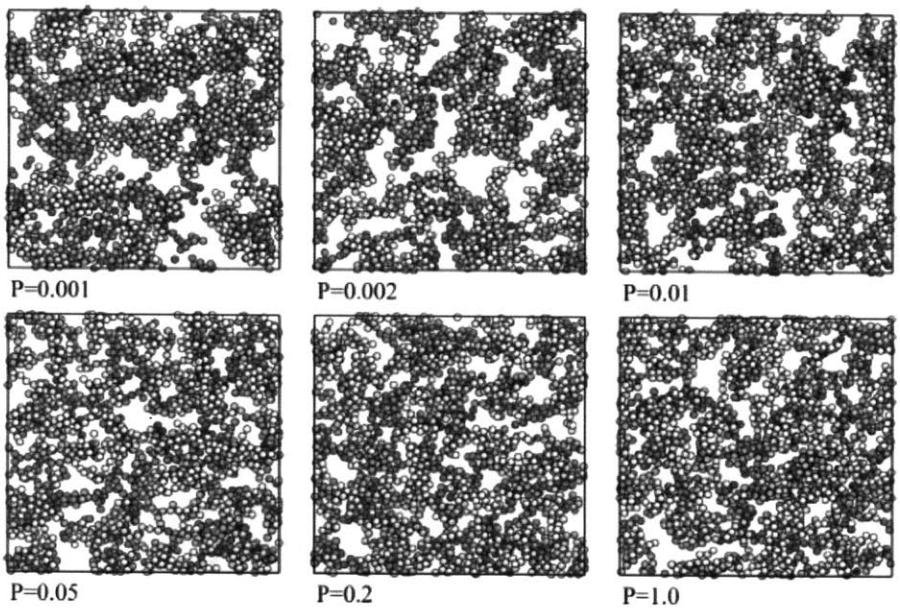

Figure 2-41: Results with a flexible model for different probabilities of formation of bonds. Only a thin slab of the structure is shown, with particle shaded by depth (Gelb, 2007).

2.4.3 Static method

The aerogels (especially the densest ones) have been described as an assemblage of random-packed spheres (Zarzycki, 1992). Esquivias, Morales-Flórez and their group have focused on numerical structural models for dense aerogels as such assemblages (Esquivias et al., 1998; Morales-Flórez et al., 2005; Morales-Flórez et al., 2008).

The model is a hierarchical one illustrated on Figure 2-42. First, one elementary sphere of unit diameter is placed in the center of the system. Then other elementary spheres are placed randomly in contact with the first one's surface to construct the first random shell. Every sphere has to be in contact at least with one other sphere, meaning within a minimum and a maximum contact distance previously defined. As many shells of random spheres are built as are required. Then the basic aggregate of the first hierarchical level is built, and its diameter is taken as the diameter of a secondary sphere. The number of shells describes the size of this basic aggregate, see Figure 2-43. The following hierarchical level is built in the same way, using these secondary spheres. After building this new aggregate, each secondary sphere is replaced with one basic aggregate, to obtain a two-level hierarchically-ordered assembly of random-packed spheres. Then the diameter of this second aggregate can be measured and used as the diameter of a tertiary sphere, if a third hierarchical level is to be built.

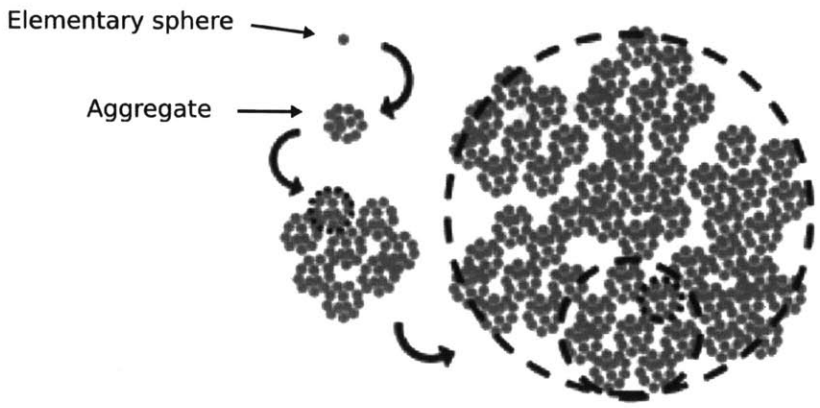

Figure 2-42: Diagram of the cluster model algorithm (Morales-Flórez et al., 2008)

Typical values of their model are 1000-60000 particles organized in 2-4 shells of random-packed spheres and 2 or 3 hierarchical levels. Their contact distance, d, are set within the interval $]0.85D, 1.0D[$, D being the particle diameter, meaning the spheres are interpenetrating. Examples are shown on figure 2-44. One

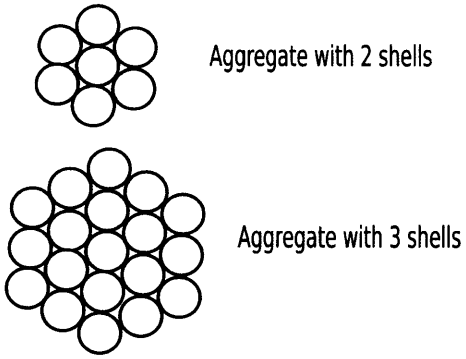

Figure 2-43: Aggregates with 2 and 3 shells

can see quite dense structures and no links as can be seen on some micrographs obtained by SEM (see Figure 2-45). The connectivity seems to be higher than for the cluster-cluster algorithms, where more "branchy" structures are obtained. This may be because the model was developed for denser gels that might not present the same structure.

The group of Morales-Flórez plans on extending their model to lighter aerogels, possibly introducing fractal description.

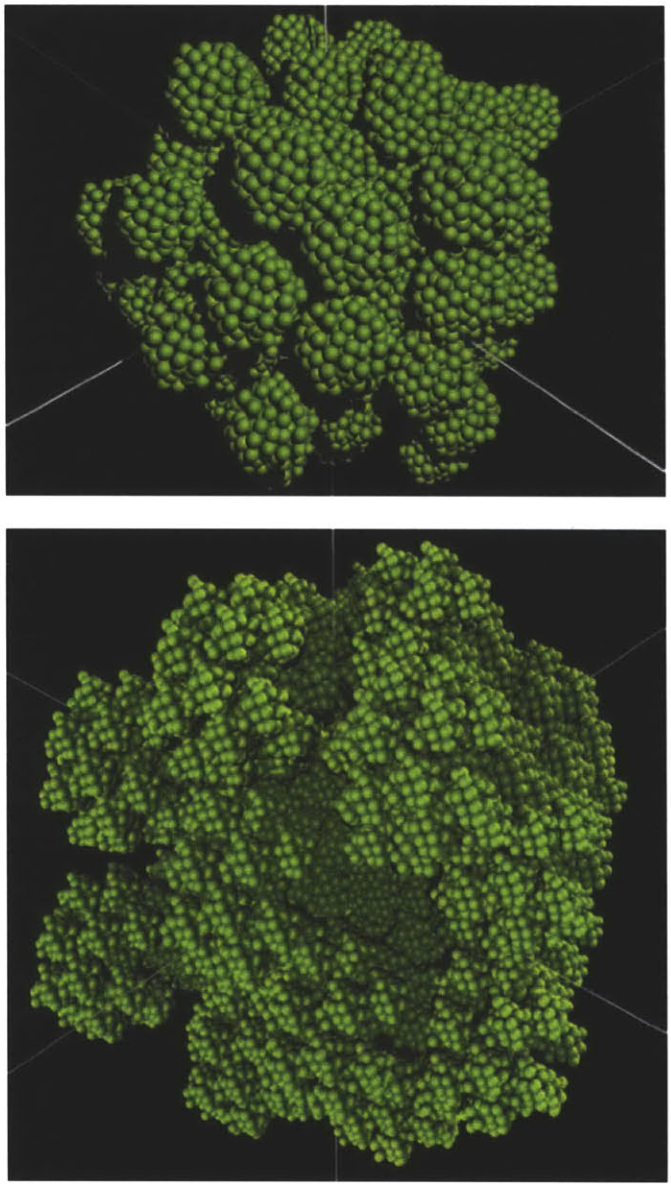

Figure 2-44: Two examples of cluster models with 3 shells of randomly-packed spheres and 2 hierarchical levels (top) and with 2 shells and 3 hierarchical levels (bottom), by Morales-Flórez et al. (Morales-Flórez et al., 2005)

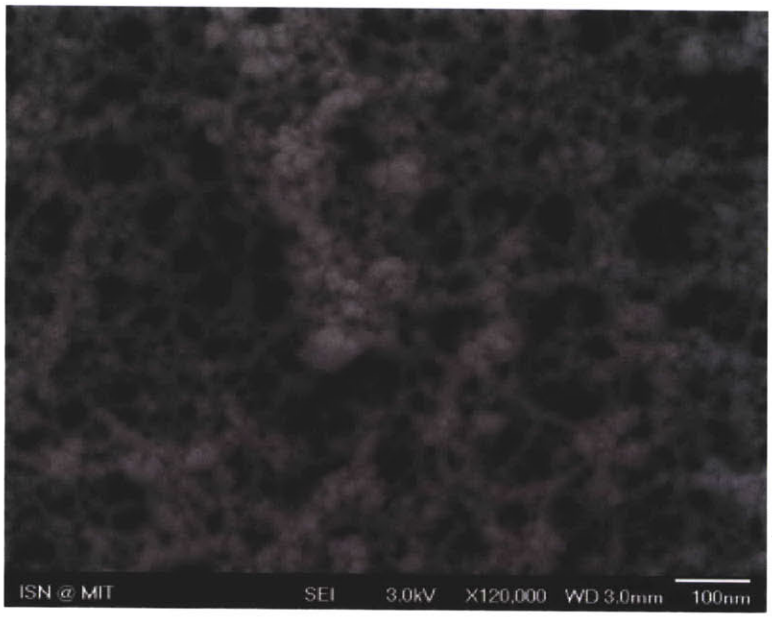

Figure 2-45: SEM micrograph of one of our aerogels

2.4.4 Characterizing the models

It is necessary to characterize accurately the structures obtained by simulations in order to set the different parameters and compare the simulated structures to actual materials.

Numerical characterization methods are often harder to define and require more computing time than the simulation of the structure itself.

The first item used for characterization is the distance distribution function $f(r)$, which is basically the histogram of center-to-center distances M_iM_j, the points M_i being the centers of the elementary particles. Then, the scattering function or structure factor, generally referred to as $S(q)$, is obtained as the Fourier transform of $f(r)$. $S(q)$ corresponds to the scattered intensity found by scattering experiments (SAXS and SANS) and comparisons can be made between simulation and materials by this mean, see for example on Figure 2-46. The curve allows determination of the fractal dimension d_f and the mass correlation length ξ.

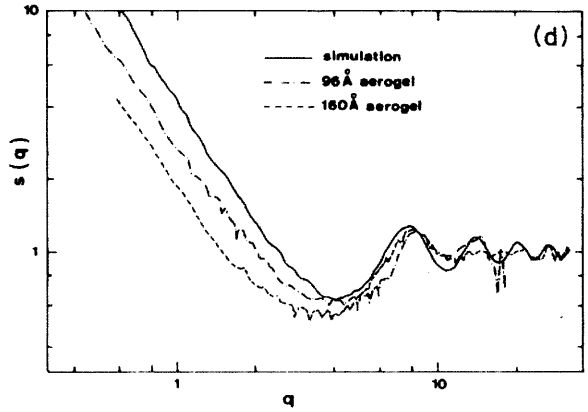

Figure 2-46: Comparison of the scattering curves for aerogels of constant density $\rho = 0.10g/cm^3$ (but with different particle size) and the simulated curve in the diffusion-limited case (DLCA model) (Hasmy et al., 1993)

Another particular characterization that one looks for is the Pore Size Distribution (PSD). Multiple ways of defining pores can be used in an assemblage of spheres with sometimes very different results. A pore is generally defined as a sphere, so the PSD is usually obtained geometrically by calculating, for each point of the pore space, the radius of the biggest sphere that fits into the pore volume, all by means of a Monte-Carlo integration (Gelb, 2007; Morales-Flórez et al., 2008). Other ways of calculating the pore

size are also reported, such as triangulation (see scheme on Figure 2-47). These methods can give very different results, as shown on Figure 2-48. Some studies have also tried to model nitrogen adsorption itself, but this has not been applied to aerogels due to the compliant behaviour of the network, which is hard to model.

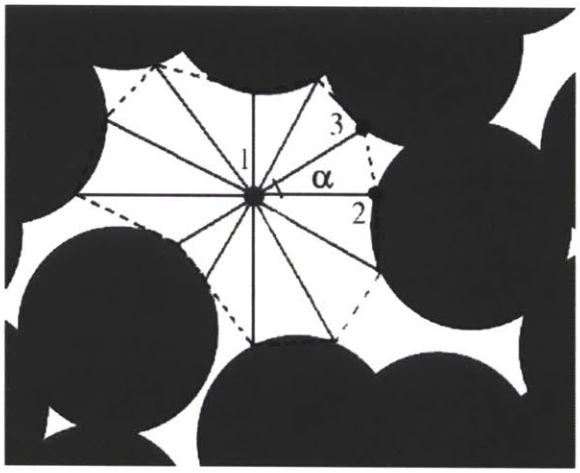

Figure 2-47: Schematic illustration of the 2-dimensional triangulation method applied to the pore space (Morales-Flórez et al., 2008)

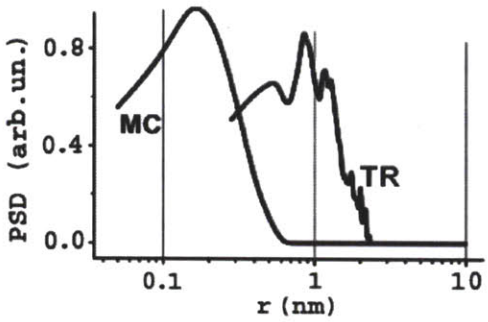

Figure 2-48: Comparison of two PSD calculation methods (Monte-Carlo integration and triangulation) on the static model of Morales-Flórez et al. (Morales-Flórez et al., 2008)

2.4.5 Simulating the mechanical properties

Method

The group of Morales-Flórez (Esquivias et al., 1998; Morales-Flórez et al., 2005; Morales-Flórez et al., 2008) studied the mechanical strength of their simulated aerogels (with the static method described in Section 3) but not by numerical means. They used an expression from the literature (Rumpf, 1958) to find the normalized strength due to the overlapping of the spheres as a function of the porosity:

$$\frac{\sigma}{\sigma_0} = \frac{9}{32}(1 - P)K\phi$$

where P is the porosity, K the mean coordination number and ϕ a factor accounting for the relative overlapped volume in the new system. They find results similar to those of Woignier's model of a cubic arrangement of overlapping spheres (Woignier and Phalippou, 1988). Using this model, they find values close to the experimental data and conclude that their structural model is of interest in describing aerogels.

The group of Ma et al. (Ma et al., 2000; Ma et al., 2001; Ma et al., 2002) have investigated the mechanical behaviour of the simulated structure obtained with DLCA models. Interestingly, they use the results as a mean of reassessing and correcting the model. This is at once a way to prevent unrealistic results and a risk as the structure is corrected by the same results as those the study wants to investigate.

The interparticles bonds are assumed to behave mechanically as beam elements resistant to 6 degrees of freedom (e.g., compression, bending, shear, torsion). The effects of the beam parameters are also studied. A further approach would be to further discretize the bonds, which could take more realistic shapes as strings of pearls, but this is for now too demanding on computer resources, and more importantly, according to the study, the beam elements are sufficient in providing good resemblance to the fibrous network in aerogels.

A boundary condition of -1% (compressive) volumetric strain is imposed by displacing the particles at the boundary towards the inside of the box. The bulk modulus K can then be calculated from the strain energy (or directly from the applied stress). Assuming a constant Poisson's ratio, the bulk modulus is proportional to the Young's modulus E.

Results

Ma et al. (Ma et al., 2000) have investigated the effect of the dangling mass (or dead-ends) that were believed to account for the high-scaling exponent m of the Young's modulus against density. An algorithm was thus developed to remove all the dangling mass from the model, so that the scaling behavior of the "perfectly" connected models could be compared to the initial model.

In the model, as little as 10% of total mass is perfectly connected when the initial relative density is low, at 0.03 (non dimensional units). It is shown that the perfectly connected networks exhibit fractal behavior similar to the DLCA models.

The scaling relationship of bulk modulus against relative density, derived from computer simulation, is illustrated in Figure 2-49. The untrimmed DLCA models show a scaling behavior with an exponent of 7.6. The data points of the perfectly connected (trimmed) network do not fall on a single regression line, but the points at lower density exhibit a power-law relationship with an exponent of 3.6.

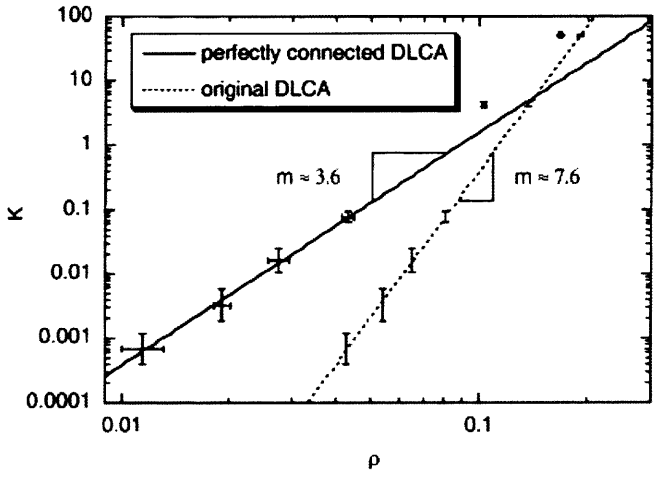

Figure 2-49: Scaling relationship of bulk modulus with relative density of DLCA models by the finite element analysis for DLCA models (original and perfectly connected) (Ma et al., 2000)

The effects of the beam parameters are studied. The bulk modulus varies linearly with the Young's modulus of the beams, but scales with an exponent q with the aspect ratio, which is, in the case of a square beams, the ratio $a = \frac{\text{beam width}}{\text{beam length}}$

$$K \propto a^q$$

q is almost constant at 4, indicating the major mechanism involved in compression is the bending of the

beams. Since q is constant, the scaling exponent of the Young's modulus $m \approx 3.6$ is independent of the beam properties (given that these properties remain uniform over the range of densities considered). Plus, it shows that if we make the density vary only by changing the cross-section of the beams and not the structure itself, we find the same scaling law as for an open-cell model with minor defects (Gibson and Ashby, 1997),

$$K \propto \rho^2$$

(Remark that if a perfect isotropic open-cell is submitted to a perfectly isotropic load, there will be no bending and we have $K \propto \rho$ but minor defects in the symmetry quickly lead to bending of the struts in all the structure and $K \propto \rho^2$.)

For the authors, the simulation shows that the exponent higher than this of 2.0 found in open-cell model (Gibson and Ashby, 1997) is not to be attributed to the dead-ends. They show that the trimmed DLCA model provides another explanation. The uneven distribution of the bonds results in inefficient sharing of the load, and significantly reduces the stiffness of the network. The disparity increases when density decreases, meaning fewer and fewer bonds are carrying the load, see figure 2-50. This phenomenon is distinctly different from the assumptions of the open-cell foam in which the increase of density is caused by thickening of the beams; here, the beams have uniform dimension and mechanical properties at all densities. This assumption is reasonable since in the sol-gel process, the particle size is determined only by the processing conditions such as pH value. Therefore, under the typical time-invariant processing conditions, the variation of the particle size, bond thickness, bond length and bond stiffness should be minimal.

Moreover, the study shows that the DLCA models with its dead-ends can not account precisely for the mechanical behavior since it exhibits too high an exponent. However, the "trimming" mechanism itself is too artificial as a mechanism for explaining the structure and the mechanical properties. Therefore, a new aggregation mechanism was developed in further studies (Ma et al., 2001; Ma et al., 2002) to capture the structural and mechanical properties of the gel-types materials. The DLCA was combined with a "dangling bond defection" algorithm to transform the dead-ends to loops. The same exponent of 3.6 is found with this mechanism.

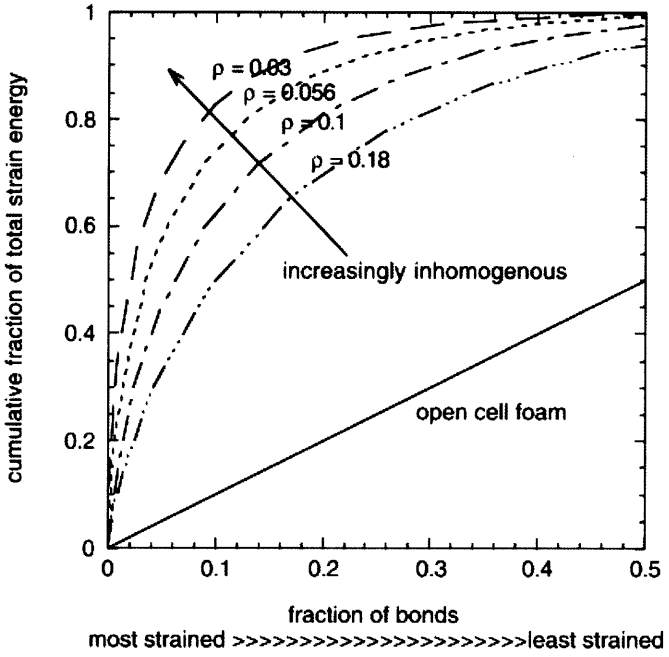

Figure 2-50: Cumulative distribution of strain energy in a bond (Ma et al., 2001)

Recent work

Recent work by Gelb (Gelb, 2007) has introduced further complexity in the mechanical simulation. They use the potentials introduced for the simulation of gelation and aging also for mechanical characterization. The bulk modulus K is determined through fluctuation analysis. K is calculated as the inverse of the isothermal compressibility κ_T, with

$$\kappa_T = -\frac{(\partial V/\partial P)_T}{V} = \frac{\langle \delta V^2 \rangle}{k_B T V}$$

The results are not in good agreement with experiments yet, according to the author. Values found for K are lower than expected (but of the same order of magnitude). The author suggests that minor modifications of the parameters and physical conditions could produce close agreement with experiment. The major interest of the model is to allow the study of extreme deformation and failure of the aerogels, which is not possible with simple beam elements.

2.5 Commercially available aerogels

After this review of the structure and mechanical properties of aerogels, we shift our focus to aerogels which are currently commercially available. We distinguished three categories: aerogel not initially intended as thermal insulation; aerogel commercialized for very high insulation purposes; and aerogel commercialized for building insulation.

2.5.1 Raw aerogel and non-insulating applications

Marketech International

Marketech International (Port Townsend, WA, USA, http://www.mkt-intl.com), sells silica aerogel in random pieces (0.2 to 2.0 cm) or in translucent monolithic blocks. They sell it for no application in particular. The density of their aerogel is $\sim$0.1 g/cm^3.

They give some physical data for their products:

- pore diameter $\sim$20 nm
- Poisson's ratio $\nu = 0.2$
- Young's modulus 1 - 10 MPa
- tensile strength 16 kPa
- compressive strength 0.3 MPa
- thermal conductivity in air 16 mW/m K
- thermal conductivity in vacuum 4 mW/m K

Prices are high, \$9,000 - 15,000 / kg for random pieces and \$50,000 - 70,000 /kg or \$5,000 - 7,000 /L for monolithic pieces (up to 4 x 8 x 0.5").

Markettech also sells resorcinol-formaldehyde (RF) aerogels and carbon aerogel in random pieces and in paper in the same range of prices.

United Nuclear

United Nuclear Scientific LLC (Laingsburg, MI, USA, http://unitednuclear.com) also sells a granular aerogel. They claim a density of 0.003 g/cm^3 (which can be calculated to be aerogel with a volume

fraction of air of 99.86%) but in reality they sell products with densities between 0.140 and 0.270 g/cm^3 with prices in the range \$200 - 300 /kg or \$35 - 55 /L. Like Markettech, they do not sell for specific applications.

Figure 2-51: Granular aerogel (100 cm^3 container) - United Nuclear

TAASI

TAASI Corporation (Delaware, OH, USA, http://www.taasi.com) commercializes a range of products called Pristina™Aerogels. They suggest several possible applications, mainly chemical applications (absorption, adsorption, catalysis and controlled release) but also thermal insulation properties. They say that they hold the application patent for the use of aerogels in the removal of pollutants from water and air.

TAASI make either aerogel powder or beads (~3 mm wide) out of various materials, utilizing a water-based process, which, they say, allows for lower pricing. They claim a high crush strength for their monolithic aerogels, but the strength is given as a force (9-14 Lbf) rather than a stress. Under the hypothesis of a circular flat surface of diameter 3 mm, this would give 6 to 9 MPa.

Figure 2-52: TAASI Aerogel Products

2.5.2 Aerogels commercialized for high insulation applications

American Aerogel™

American Aerogel Corporation (Rochester, NY, USA, http://www.americanaerogel.com) is commercializing aerogel panels named Aerocore™, in vacuum insulated panels. They use monolithic organic aerogel (polymeric and carbon-based) of density 0.050 to 1.0 g/cm^3. Their pore size ranges from 100 nm to 1 μm. They make panels of <1 mm thick and up (no upper limit given). Many shapes are available by mold form and machining. The main application are boxes for shipping of products at low temperature.

They claim to achieve a R-value of R-50 per inch (2.9 mW/m K). The pressure inside the panel is not public. Price is only given for specific quotes.

Glacier Bay

Glacier Bay, Inc (Union City, CA, USA, http://www.glacierbay.com) has a commercial product named Barrier Ultra-R™. It is a vacuum insulation panel. They suggest using it to retrofit iceboxes or refrigerators. They claim a thermal conductivity of R-50/in (2.9 mW/m K), reduced to R-9/in (16 mW/m K) if the panel is punctured and the vacuum no longer maintained. The vacuum inside is about 0.5 torr.

Typical panels include infrared opacifiers and a moisture-proof membrane. They are encapsulated in a tough polypropylene, or optionally fiberglass. The density (without encapsulation) is 0.164 g/cm^3.

The panels are 30 mm thick (without encapsulation) and are sold in typical sizes of : 36" x 22" and 29" x 24" (for $345) and 60" x 70" (for $595), which gives for the biggest panels $7.3 /L or $44.6 /kg.

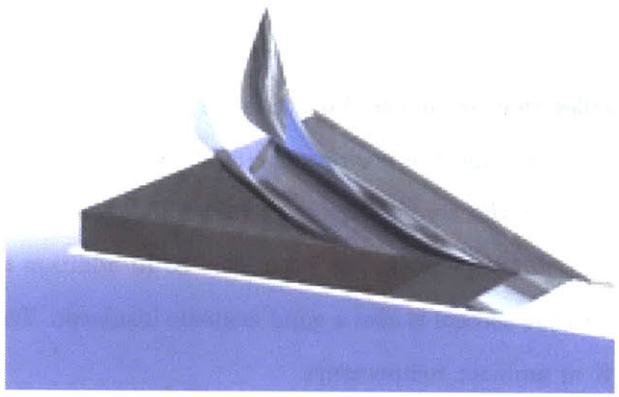

Figure 2-53: Panel with aerogel core - Glacier Bay

2.5.3 Aerogels commercialized for building insulation applications

Aspen Aerogel™

Aspen Aerogel, Inc (Northborough, MA, USA, http://www.aerogel.com) sells thin and flexible blankets containing aerogel. Their insulation product for buildings and homes is called "Spaceloft®". They sell blankets that are 5 or 10 mm thick and up to 1,450 mm wide. The density is 0.150 g/cm^3. The resistance of their product is $\sim$ R-10 per inch at ambient temperature (13-14 mW/m K).

Aspen Aerogels also have products for industrial insulation over a wide range of temperatures; they are especially interested in pipes insulation applications.

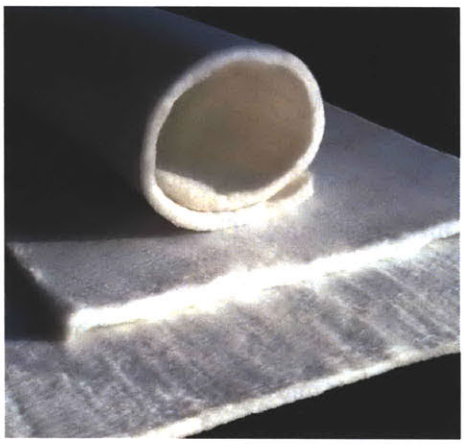

Figure 2-54: Aspen Aerogel™Spaceloft®

Cabot

Cabot Corporation (Boston, MA, USA, http://www.cabot-corp.com) sells aerogel under the name "nanogel®". Their basic product is granules that are 0.5 to 4.0 mm wide and could be use for filling wall cavities. The mean pore diameter is $\sim$20 nm and the porosity is >90%, corresponding to a bulk density of 0.090 - 0.100 g/cm^3. Cabot states that the aerogel has been tested for ignition and that the flash ignition temperature and the self ignition temperature are both 395 °C. In addition of the thermal properties, they are emphasizing the fact that aerogel is also a good acoustic insulator. The granules have a thermal conductivity of 18 mW/m K at ambient temperature.

They sell also an insulating blanket (nanogel Thermal Wrap™). The blanket is 4 - 10 mm thick, 56 cm wide and rolls up to 100 m long. The conductivity is 21.5 mW/m K at ambient temperature. The

density is 0.075 g/cm^3. The tensile strength is $\sim$7 kPa.

Finally, they have also composite panels for daylighting applications, with 75% light transmission and a R-value of R-8 per inch (18 mW/m K).

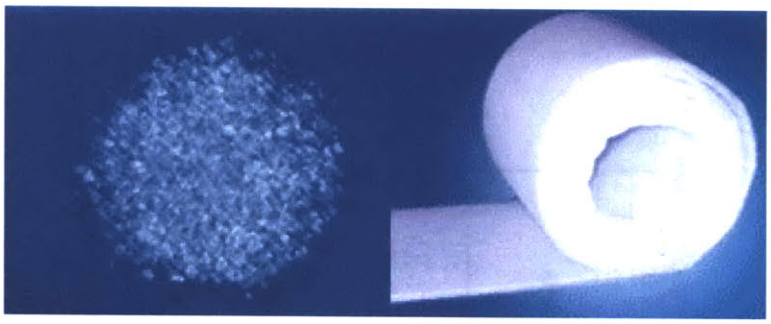

Figure 2-55: Cabot products: Nanogel® particles (left) and Thermal Wrap™(right)

2.5.4 Summary

We summarize in tables 2.2 and 2.3 the key properties of commercially available aerogels.

Table 2.2: detailed properties for aerogel commercialized with no insulating purposes

Company	Marketech international	United Nuclear	TAASI
Product			Pristina™Aerogel
Microstructure			
Composition	silica	silica	various
Density (g/cm^3)	0.1	0.14 - 0.27	
Pore size (nm)	20		
Thermal Properties			
lambda (in air) (mW/mK)	16		
lambda (in vacuum) (mW/mK)	4		
Mechanical Properties			
Young's modulus (MPa)	1-10		
Poisson's ratio (-)	0.2		
Compressive strength (kPa)	300		6,000
Tensile strength (kPa)	16		
Cost ($/kg)	9,000	200	
Product form	pieces - monolithic blocks	granules	powder, beads
Notes			water-based process chemical applications

Table 2.3: detailed properties of aerogel commercialized for insulating applications

Company	American Aerogel	Glacier Bay	Aspen Aerogel™	Cabot
Product	Aerocore	Barrier Ultra-R™	Spaceloft®	nanogel®
Microstructure				
Composition	organic		silica	silica
Density (g/cm^3)	0.05 - 1.0	0.164	0.150	0.09 - 0.1
Pore size (nm)	100 - 1,000			20
Thermal Properties				
lambda (in air) (mW/mK)		16	13	18
lambda (in vacuum) (mW/mK)	2.9	2.9		
Mechanical Properties				
Young's modulus (MPa)				
Poisson's ratio (-)				
Compressive strength (kPa)				
Tensile strength (kPa)				
Cost ($/kg)		45		
Product form	panels			
Notes	vacuum insulated boxes for shipping	vacuum insulated	flexible blanket	granules or blanket tested for ignition

2.6 Limitations of aerogels for their use in thermal insulation

2.6.1 Monolithic aerogel and its potential improvement

In the previous section, we showed that current thermal insulations using aerogel were either using aerogel particles embedded in fibers or vacuum insulated panels (VIP) with a high vacuum. The first method gives a relatively flexible blanket material that is easy to use but the fact that the aerogel component is made of separate particles embedded in the fibers gives less thermal insulation than could be hoped for aerogel-based insulation (generally more than 15 mW/mK). Furthermore, the aerogel particles reportedly tend to turn into dust over the long term. Also, a reduced vacuum has less effect on the thermal conductivity of particles than on the thermal conductivity of monolithic aerogel (Smith et al., 1998). On the other hand, VIPs are extremely good insulators, but they are expensive to make and maintaining a high vacuum over the long term is a difficult challenge.

Monolithic aerogel seems to be, in some ways, an ideal response. They provide great thermal insulation at atmospheric pressure or low vacuum. There is no path for air as there is when particles are used. The challenge is that there are weak and brittle.

One way of solving this problem is to synthesize aerogel with improved mechanical properties. This was extensively investigated by another student in the group, Yanjia Zuo (Zuo, 2010).

Different ways of improving monolithic aerogels have been tried. Zhihua et al. incorporated ceramic fibers in a silica gel preparation. This allowed for an ambient drying process and increased the mechanical strength by a factor of 6 (the mechanical strength being taken here as the recorded stress when the aerogel is damaged during an indentation experiment). However, the thermal conductivity was measured at 29 mW/mK (an increase of 6 mW/mK for this particular aerogel) which is too high for high thermal insulation (higher than a variety of polymer foams) (Zhihua et al., 2008). DeFriend et al. have templated silica aerogel with polystyrene (DeFriend et al., 2007). They incorporate polystyrene beads of size 50 nm to 2 μm in the preparation, supercritically dry the gel and finally remove the beads by oxidation, with the purpose of giving a more regular and thus more mechanically efficient structure to the aerogel. The resulting aerogel has improved mechanical properties (Young's modulus increased from 2 MPa up to 5 MPa with the highest amount of polystyrene and the smallest beads) but also has mesoporous pores, which can be expected to increase significantly thermal conductivity. It also has significantly higher complexity.

Yanjia Zuo focused on adding inorganic binders to aerogels. Previous work (Meador et al., 2005; Ilhan et al., 2006) has been done with incorporation of organic cross-linkers in the gel leading to cross-linking between the silica skeleton and surface-modifiying agents such as epoxides and polystyrene, but those processes are costly and likely lead to an increase in thermal conductivity. Zuo used instead small amounts of inorganic synthetic nanocomposites. Improved ductility is reported, along with low thermal conductivity similar to the other aerogels that were synthesized during the study.

Yanjia Zuo and Yi He also studied the effect of different synthesis parameters on the mechanical properties, namely the catalyst concentration and the solvent concentration. Some improvement could be made to increase the strain at fracture, but those also had the side effect of decreasing the density of the aerogel, and its absolute Young's modulus and strength. The resulting aerogel is thus softer and can be more easily handled without breaking, but will be still more sensitive to a constant load, such as an indentation by a body of given weight.

2.6.2 A comparison of monolithic aerogel with common insulation materials

We can compare aerogel properties with those of common insulating materials, whose densities are given in Table 2.4, in Table 2.5, 2.6 and 2.7 and Figure 2-56.

We see that the aerogels have mechanical properties (elastic modulus and strength) lower than that of common insulation materials by one to two orders of magnitude. In addition, having the behavior of a brittle material they have low strain at fracture (around 5%) and the mode of failure is generally catastrophic, why we need to increase those numbers in order to make a suitable product for the building industry (in which they differ, for example, from fiber glass or rock wool, which also have low mechanical properties but are not brittle). We want to have a panel that can be easily handled without breaking when it bends under its own weight or falls on the ground (more on typical loads can be found in chapter

Table 2.4: Densities of common insulating materials

Material	density (g/cm^3)	density (lb/ft^3)
Perlite	0.030 - 0.150	1.8 - 9.4
Polyisocyanurate foam	0.025 - 0.100	1.6 - 6.2
Expanded polystyrene foam	0.015 - 0.050	0.9 - 3.1
Extruded polystyrene foam	0.030 - 0.050	1.8 - 3.1
Cellular Glass	0.120 - 0.250	7.5 - 15.6
Gypsum board	0.600 - 0.800	37.5 - 50.0
Aerogel	0.100 - 0.150	6.2 - 9.4

Table 2.5: Young's modulus of common insulating materials

Material	Young's modulus (MPa)	Young's modulus (psi)
Perlite	10 - 12	1400 - 1800
Polyisocyanurate foam	1.8 - 3.3	250 - 500
Expanded polystyrene foam	0.7 - 10	100 - 1400
Extruded polystyrene foam	1.4	200
Cellular Glass	900	13000
Gypsum board	2 - 5	300 - 700
Aerogel	0.7 - 1.0	100 - 145

Table 2.6: Flexural strength of common insulating materials

Material	Flexural strength (kPa)	Flexural strength (psi)
Perlite	300 - 400	45 - 60
Polyisocyanurate foam	120 - 1000	18 - 150
Expanded polystyrene foam	30 - 900	4 - 130
Extruded polystyrene foam	300 - 350	44 - 50
Cellular Glass	500 - 550	70 - 80
Gypsum board	1500 - 2500	200 - 350
Aerogel	30 - 80	4 - 12

Table 2.7: Compressive strength of common insulating materials

Material	Young's modulus (MPa)	Young's modulus (psi)
Perlite	350 - 2000	50 - 300
Polyisocyanurate foam	60 - 700	9 - 100
Expanded polystyrene foam	30 - 500	4 - 70
Extruded polystyrene foam	170 - 1000	25 - 140
Cellular Glass	550 - 1600	80 - 230
Gypsum board	3500 - 10000	500 - 1450
Aerogel	30 - 80	4 - 12

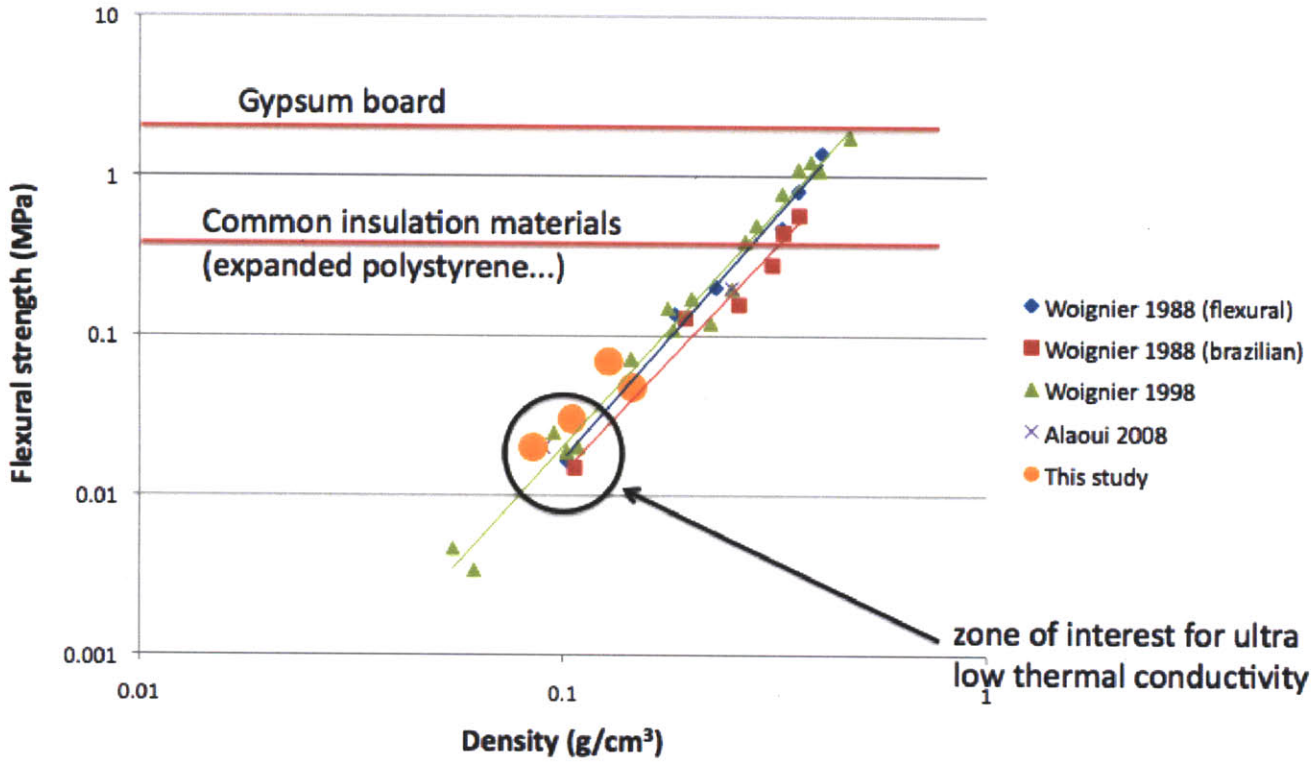

Figure 2-56: Comparison of the strength of aerogels with that of common insulation materials

4), which is not the case with the aerogel as it is currently synthesized. The routes described in section 2.6.1 do not alone give enough improvement for that purpose. That is why we are investigating in the next chapters a composite concept.

Chapter 3

Core structures for composite panels

3.1 Introduction

The previous chapter showed that silica aerogel by itself is more compliant and more brittle than most common insulation materials by several orders of magnitude. This can be explained by the microstructure of aerogels. They are made of silica nanoparticles, tens of nanometers in diameter, poorly bonded together at narrow necks into tangled chains, which themselves form larger scale aggregates on the order of hundreds of nanometers. The disorder of the structure is responsible for the rapid decrease in mechanical properties with density. The arrangement of the fibers itself is poor, with some disconnected, dangling fibers, so that a small fraction of the fibers support most of the load.

We do not believe that we can increase the mechanical properties of an aerogel to a point where it can be used by itself as an insulation panel while maintaining its low thermal conductivity. We are now investigating the idea of a composite panel where the rigidity would be provided by another component. The two structures that are envisioned for that purpose are honeycombs and truss lattices. Both have the advantage, compared to aerogels, that their members (walls or trusses) are geometrically regular, that they deform by local stretching when submitted to a load, and that the load is applied evenly to all members: they are thus much more efficient mechanically.

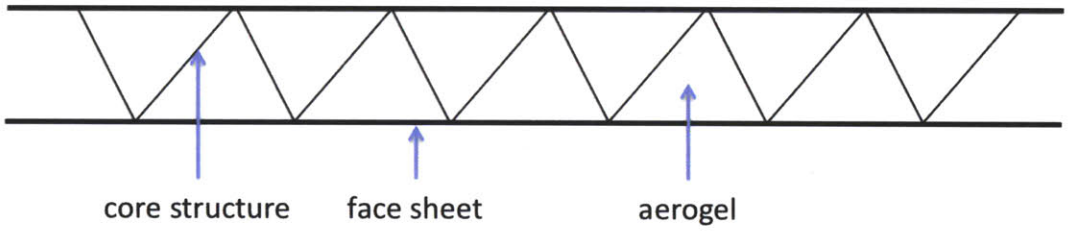

Figure 3-1: Drawing of the suggested structure of an aerogel insulation panel

3.2 Review and Analysis

In this section, we analyze the mechanical and the thermal properties of honeycombs and truss cores. We calculate properties for the cores, as a function of the core density and of the properties of the bulk material the core is made of. A substantial part of the mechanical analysis is available in the literature on lightweight and structurally efficient structure for sandwich panels, generally in the context of metal structures.

For those cellular materials, the principle of the analysis is to consider one repeating unit cell and to perform the analysis on this cell. Then the result is taken as that of the entire core by neglecting the edge effects, which can be considered as reasonably accurate for honeycombs or lattice structures with about 10 cells or more along one dimension.

The mechanical properties of interest for the cores are:

1. The Young's modulus and compressive strength.

2. The shear modulus and shear strength. As mentioned by Gibson and Ashby (Gibson and Ashby, 1997), in a sandwich panel where the faces are stiffer than the core, which is usually the case, the core is mostly loaded in shear when the panel is bent.

In all the following, the superscript $*$ will indicate the core, while the subscript S will refer to the material the core is made of.

3.2.1 Honeycombs cores

Geometry

A honeycomb is a two-dimensional cellular material made of an array of prismatic cells which nest together to fill a plane, as seen on Figure 3-2. We are considering in our study hexagonal cells, which are the most common shape.

The general geometry of an hexagonal cell is given in Figure 3-3. In a regular hexagonal cell, the cell is a regular hexagon ($\theta = 30°$, $h = l$) with walls of length l and the walls have a uniform thickness t. In that case, the relative density of the honeycomb core is

$$\frac{\rho^*}{\rho_S} = \frac{2}{\sqrt{3}} \frac{t}{l} \tag{3.1}$$

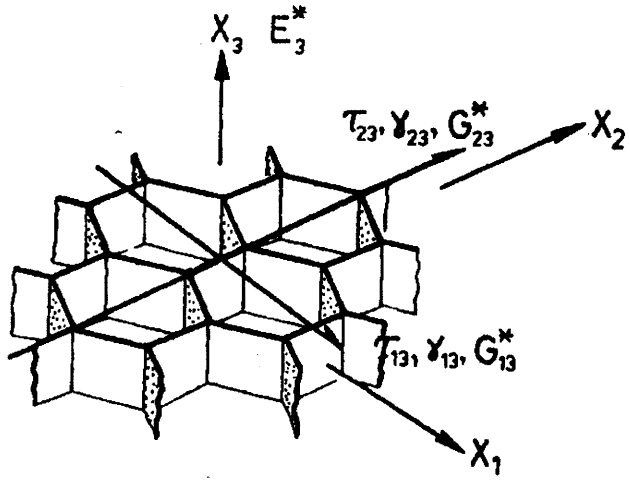

Figure 3-2: Honeycomb structure, from Gibson and Ashby (Gibson and Ashby, 1997)

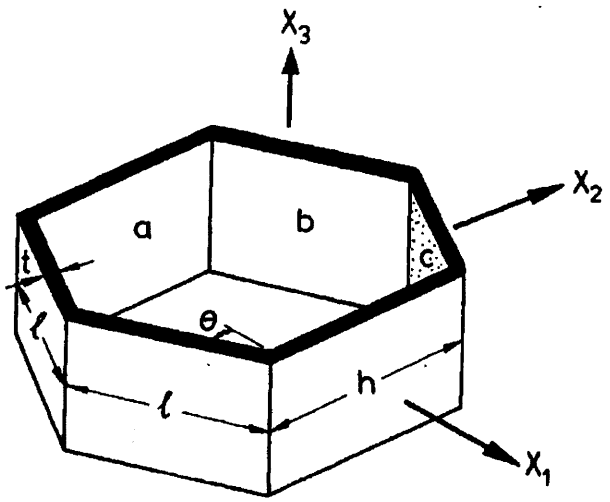

Figure 3-3: Honeycomb cell, from Gibson and Ashby (Gibson and Ashby, 1997)

Commercial honeycombs are commonly made by gluing strips of material periodically such that when pulled part, hexagonal cells are formed (Gibson and Ashby, 1997). The resulting cells have two out of six walls of double thickness, as seen in Figure 3-4.

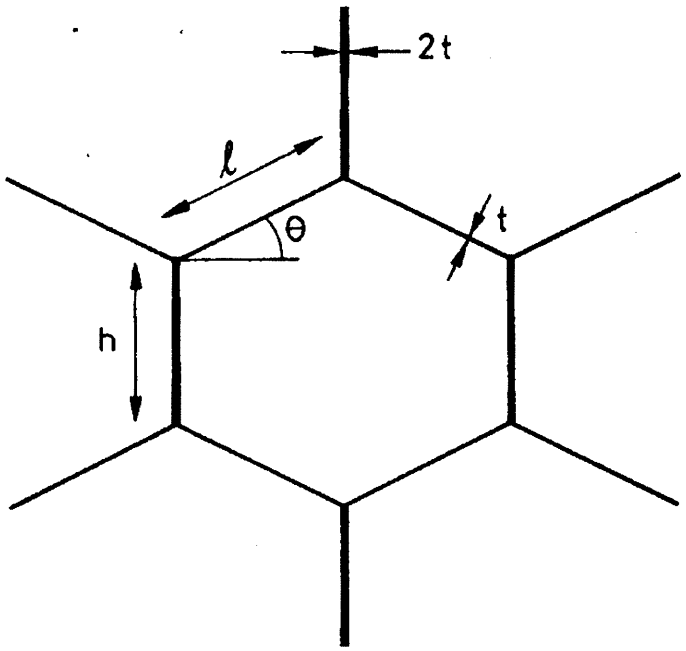

Figure 3-4: Double-wall honeycomb, from Gibson and Ashby (Gibson and Ashby, 1997). The inclined walls have thickness t while the vertical walls have thickness $2t$.

Mechanical properties

Mechanical properties of honeycombs are extensively analyzed by Gibson and Ashby (Gibson and Ashby, 1997). For a honeycomb with regular hexagonal cells, the mechanical properties are:

The compressive Young's modulus:

$$\frac{E^*}{E_S} = \frac{\rho^*}{\rho_S} \tag{3.2}$$

The shear modulus:

$$\frac{G^*}{G_S} = \frac{1}{2}\frac{\rho^*}{\rho_S} \tag{3.3}$$

The yield strength in compression:

$$\frac{\sigma_c^*}{\sigma_{ys}} = \frac{\rho^*}{\rho_S} \tag{3.4}$$

The elastic buckling limit in compression (assuming $\nu = 0.3$):

$$\frac{\sigma_c^*}{E_S} = 5.2\left(\frac{t}{l}\right)^3 = 3.4\left(\frac{\rho^*}{\rho_S}\right)^3 \tag{3.5}$$

The plastic buckling limit in compression, another possible mode of failure:

$$\frac{\sigma_c^*}{\sigma_{ys}} = 5.6\left(\frac{t}{l}\right)^{\frac{5}{3}} = 4.4\left(\frac{\rho^*}{\rho_S}\right)^{\frac{5}{3}} \tag{3.6}$$

The buckling limit in shear (lowest):

$$\frac{\tau_c^*}{E_S} = 3.6\left(\frac{\rho^*}{\rho_S}\right)^3 \tag{3.7}$$

An analysis was carried on double-wall honeycombs as well. Those honeycombs exhibit in-plane anisotropy. The results are given in the tables summarizing the mechanical properties of all the types of cores (Tables 3.1 and 3.2) and we will not elaborate on them here.

Thermal properties

We find an equivalent thermal conductivity of a honeycomb core by considering that the two ends of the core are at constant temperature. It is easy to conclude that the conductivity λ^* of the honeycomb, relative to the thermal conductivity λ_S of the material it is made of, is given simply by the area ratio of the material in the honeycomb, which is also equal to the volume or mass fraction of the honeycomb.

$$\frac{\lambda^*}{\lambda_S} = \frac{\rho^*}{\rho_S} \tag{3.8}$$

3.2.2 Truss cores

Description of the tetrahedral truss core

The geometry of the cores is shown on Figure 3-5. The core trusses are the dashed members. The solid lines making up the top and bottom faces are not actual members in our case since we have a face sheet, but it shows what the structure is: the tetrahedrons occupy one out of two sites of a triangle paving. A single tetrahedron is shown in Figure 3-6. The length of a member in the core is L_C and the core thickness is H_C. Initially, only circular members of radius a will be considered. The length of the virtual -but useful to define the geometry- struts in the face is L_F. To be noted, there is a relationship between

L_C, H_C and L_F: $H_C = \sqrt{L_C^2 - \frac{1}{3}L_F^2}$. We also introduce the angle ω between the core members and the normal to the faces, $\omega = \cos^{-1}(\frac{H_C}{L_C})$. The structure in which the tetrahedrons are regular ($L_F = L_C$) is characterized by an angle $\omega = \cos^{-1}(\sqrt{\frac{2}{3}}) = 35.3°$. In all the following, we will refer to the faces as being "horizontal", and the third direction, normal to the faces, along the thickness of the core to be "vertical".

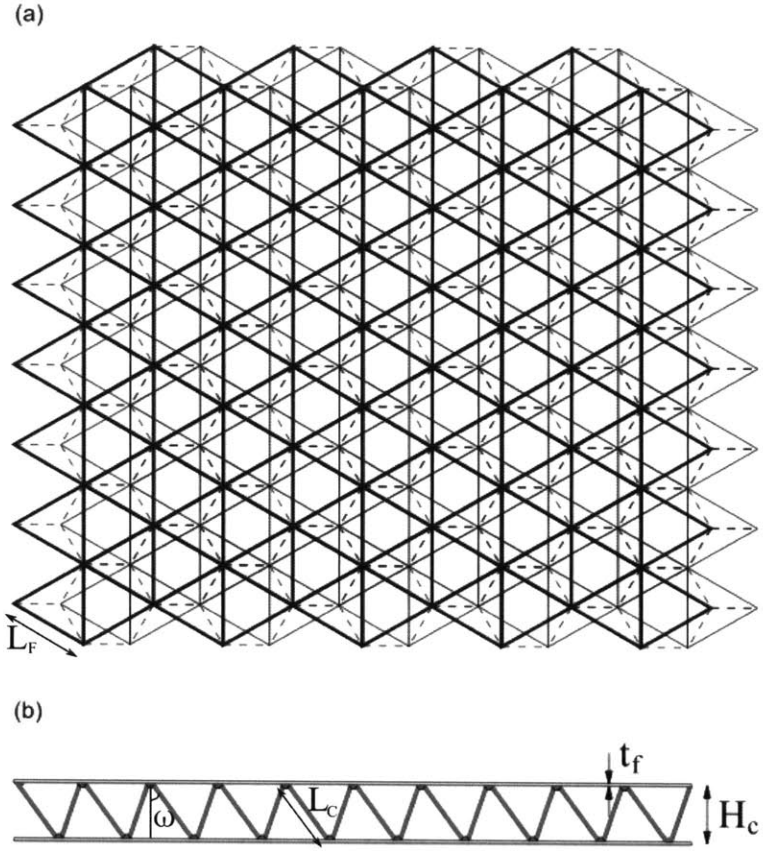

Figure 3-5: Geometry of a tetrahedral core panel, from Wicks and Hutchinson (Wicks and Hutchinson, 2001)

The unit cell of the tetrahedral core can be taken as two adjacent triangle sites, one base of a tetrahedron, the other not, over all the thickness of the core. The area of this unit cell is thus

$$A = \frac{\sqrt{3}L_F^2}{2} \tag{3.9}$$

and the volume

$$V = \frac{\sqrt{3}L_F^2 H_C}{2} \tag{3.10}$$

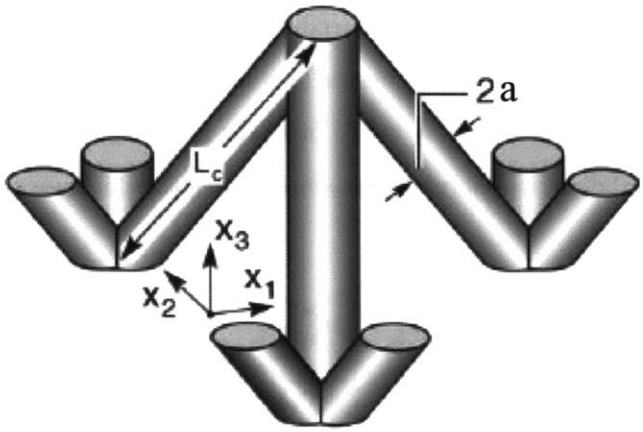

Figure 3-6: 3D representation of one of the tetrahedron, from Chiras et al. (Chiras et al., 2002)

One unit cell contains the three struts constituting the tetrahedron, for a total volume

$$3\ \pi a^2 L_C \tag{3.11}$$

Therefore, the relative density (or volume fraction) of the tetrahedral core is

$$\frac{\rho^*}{\rho_S} = \frac{2\sqrt{3}\pi a^2 L_C}{H_C L_F^2} \tag{3.12}$$

Using the angle ω, the density is also

$$\frac{\rho^*}{\rho_S} = \frac{2\pi\sqrt{3}}{3\cos\omega\sin^2\omega}\left(\frac{a}{L_C}\right)^2 \tag{3.13}$$

Mechanical properties

For calculating the mechanical properties, we consider the nodes to be glued to horizontal face sheets of infinite rigidity, meaning all the nodes of a given face will have the same displacement. For a sandwich panel where the core is a 3% dense polystyrene regular tetrahedral core, 25 mm thick, and the faces are made of pine (two to three times stiffer than polystyrene), 2 mm thick, the relative displacement of the face compared to that of the nodes is of the order of 1 %, which allows us to make this approximation.

We summarize here the mechanical properties of the tetrahedral truss core, derived from Deshpande and Fleck (Deshpande and Fleck, 2001). The struts in the core are assumed to behave like truss, deforming

only by stretching. The struts are supposed to be pin-jointed to the faces (free to rotate). Failure by yielding and buckling are investigated: the core fails by the mode with the lowest associated strength. It is to be noted that the core's behaviour is anisotropic in shear when it comes to the strength, although the elastic behaviour is isotropic. We will always give the shear strength in the weakest direction.

The compressive Young's modulus:

$$\frac{E^*}{E_S} = \frac{H_c^4}{L_c^4}\frac{\rho^*}{\rho_S} = \cos^4(\omega)\frac{\rho^*}{\rho_S} \text{ , max for } \omega = 0° \tag{3.14}$$

The shear modulus:

$$\frac{G^*}{E_S} = \frac{1}{6}\left(\frac{L_f H_c}{L_c^2}\right)^2 \frac{\rho^*}{\rho_S} = \frac{1}{8}\sin^2(2\omega)\frac{\rho^*}{\rho_S} \text{ , max for } \omega = 45° \tag{3.15}$$

The yield strength in compression:

$$\frac{\sigma_c^*}{\sigma_{ys}} = \frac{H_c^2}{L_c^2}\frac{\rho^*}{\rho_S} = \cos^2(\omega)\frac{\rho^*}{\rho_S} \text{ , max for } \omega = 0° \tag{3.16}$$

The buckling limit in compression:

$$\frac{\sigma_c^*}{E_S} = \frac{\pi}{8\sqrt{3}}\frac{L_f^2 H_c^3}{L_c^5}\left(\frac{\rho^*}{\rho_S}\right)^2 = \frac{\pi\sqrt{3}}{8}\cos^3(\omega)\sin^2(\omega)\left(\frac{\rho^*}{\rho_S}\right)^2 \text{ , max for } \omega = 39.2° \tag{3.17}$$

The yield strength in shear (lowest):

$$\frac{\tau_c^*}{\sigma_{ys}} = \frac{1}{2\sqrt{3}}\frac{H_c L_f}{L_c^2}\frac{\rho^*}{\rho_S} = \frac{1}{4}\sin(2\omega)\frac{\rho^*}{\rho_S} \text{ , max for } \omega = 45° \tag{3.18}$$

The yield strength in shear (highest):

$$\frac{\tau_c^*}{\sigma_{ys}} = \frac{1}{3}\frac{H_c L_f}{L_c^2}\frac{\rho^*}{\rho_S} = \frac{1}{2\sqrt{3}}\sin(2\omega)\frac{\rho^*}{\rho_S} \text{ , max for } \omega = 45° \tag{3.19}$$

The buckling limit in shear (lowest):

$$\frac{\tau_c^*}{E_S} = \frac{\pi}{48}\frac{L_f^2 H_c^3}{L_c^5}\left(\frac{\rho^*}{\rho_S}\right)^2 = \frac{\pi}{16}\cos^3(\omega)\sin^2(\omega)\left(\frac{\rho^*}{\rho_S}\right)^2 \text{ , max for } \omega = 39.2° \tag{3.20}$$

The buckling limit in shear (highest):

$$\frac{\tau_c^*}{E_S} = \frac{\pi}{24}\frac{L_f^2 H_c^3}{L_c^5}\left(\frac{\rho^*}{\rho_S}\right)^2 = \frac{\pi}{8}\cos^3(\omega)\sin^2(\omega)\left(\frac{\rho^*}{\rho_S}\right)^2 \text{ , max for } \omega = 39.2° \tag{3.21}$$

Note that the buckling limits are calculated with an end constraint factor $k = 1$ corresponding to pin-jointed members. In that sense, these limits are lower bounds for the buckling limit because the members may not actually be free to rotate in all directions at their ends.

More accurate calculations can be made using a beam model instead of this rough truss model, as seen on Figure 3-7. However the results are extremely close in the range that we investigate. For example, for the compressive Young's modulus, one can compute, in the limit of vanishing node volumes, and for all degrees of freedom in rotation blocked as seen on the Figure 3-7,

$$\frac{E^*}{E_S} = \cos^4(\omega)\frac{\rho^*}{\rho_S} + \frac{1}{2}\sin^3(\omega)\cos^4(\omega)\left(\frac{\rho^*}{\rho_S}\right)^2 \tag{3.22}$$

The first term in the previous equation represents the contribution to the stiffness due to the stretching of the struts and is similar to the truss model. The second term represents the bending of the strut. For a relative density of 3% and an angle $\omega = 45°$, the second term is only 0.5% of the first one.

An assumption that is more problematic is the limit of the vanishing nodes. Indeed, when we make a truss or a beam assumption, we essentially consider one dimension elements going from one node to another without intersecting (those elements have in fact no volume in the modeling). The actual struts have a non-zero thickness and thus intersect. Therefore the actual volume is lower than that calculated geometrically. For example, for pyramidal cores such as those described in section 3.4.3, the geometric calculation taking into account the length and diameters of the struts and the height of the core gives a density of 6.0 % for a given sample while the true density based on the exact geometry gives a density of 4.5%. This gives a huge factor of uncertainty in the modeling. In the following we will always input the true relative density of the sample in the formula calculated above.

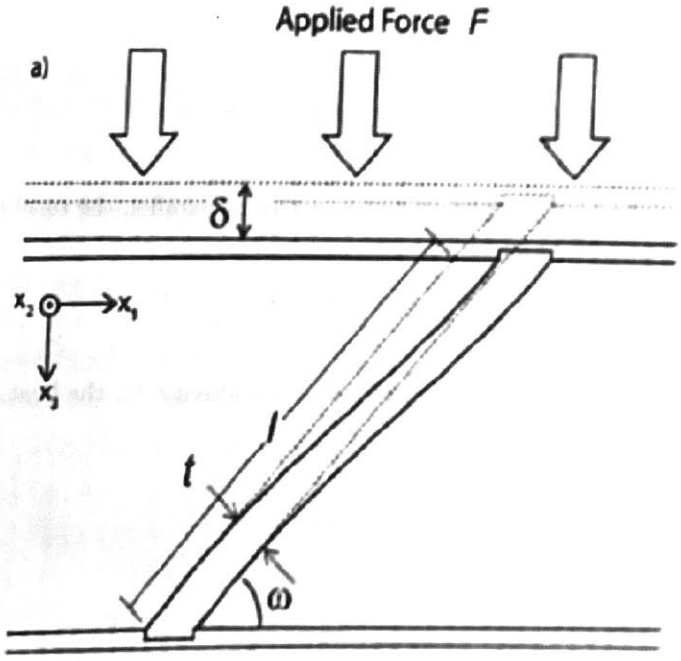

Figure 3-7: Beam model for the deformation of a truss core, from Finnegan et al. (Finnegan et al., 2007)

Thermal properties

The thermal conductivity of the core considered as a bulk material can be calculated by imposing a constant temperature over each of the face sheets. As an approximation, we do not take into account any effect of the nodes and we thus consider only the struts in each cell.

The derivation for the case of the tetrahedral core panel with a given angle ω follows. Let the upper face be at constant and uniform temperature T_1 and the lower face be at a higher constant and uniform temperature T_2. We calculate the heat flux Q between the two plates over one unit cell. We consider the only source of heat transfer is the conduction along the struts. There are three struts of length L_C. Each of them sees a temperature of T_1 at one end and T_2 at the other end. The thermal conductivity of the material is λ_S and the struts have a radius a, so each strut has a thermal resistance

$$\frac{L_C}{\pi a^2 \lambda_S} \tag{3.23}$$

Thus, the heat flux through one strut is

$$Q_{1strut} = \frac{\lambda_S \pi a^2 (T_2 - T_1)}{L_C} \tag{3.24}$$

Finally, assuming that the three struts act thermally as perfectly parallel, the total heat transfer through the unit cell is

$$Q = \frac{3\lambda_S \pi a^2 (T_2 - T_1)}{L_C} \tag{3.25}$$

If we now consider the unit cell as a bulk material of conductivity λ^*, the heat transfer between the two plates is written

$$Q = \lambda^* A \frac{T_2 - T_1}{H_C} \tag{3.26}$$

where A is the area of the unit cell, or

$$Q = \lambda^* \frac{\sqrt{3} L_F^2}{2H_C} (T_2 - T_1) \tag{3.27}$$

Finally, we equate these two expressions to find

$$\frac{\lambda^*}{\lambda_S} = 2\sqrt{3}\pi a^2 \frac{H_C}{L_C L_F^2} \tag{3.28}$$

In terms of relative density:

$$\frac{\lambda^*}{\lambda_S} = \frac{H_c^2}{L_c^2} \frac{\rho^*}{\rho_S} = \cos^2(\omega) \frac{\rho^*}{\rho_S} \tag{3.29}$$

Interestingly, the relative thermal conductivity is always equal to the relative yield strength in compression.

It is straightforward to show that the best geometry for maximizing the shear modulus at a given thermal conductivity gives an angle $\omega = 90°$. On the other hand, the optimal geometry to maximize the Young's modulus at a given thermal conductivity is to have vertical struts, $\omega = 0°$. Therefore the best core geometry will depend on what property we want to optimize.

Other geometries of cores

While this section develops the properties of the tetrahedral truss core, other geometries of cores could be used as well. One of the most relevant is the pyramidal core, see Figure 3-8. Instead of having a triangle

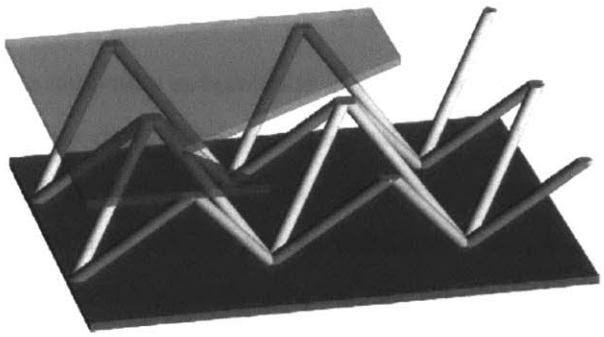

Figure 3-8: Geometry of a pyramidal core panel, from Queheillalt and Wadley (Queheillalt and Wadley, 2005)

paving of the plane with one out of two sites occupied by a tetrahedron, we have a square paving with each site occupied by a pyramid. Of the practical interest for this geometry, the nodes are disposed on a square grid. The mechanical analysis of those cores can also be found quite extensively in the literature (Deshpande and Fleck, 2001), and the thermal analysis is easy to adapt. It is interesting to note that both thermal and elastic properties are the same for both geometries in terms of relative density, but the pyramidal core is slightly worse for the minimum shear strength because it exhibits a higher anisotropy.

Another change that can be made in the geometry is the geometry of the struts. While we developed our analysis for cylindrical struts, square or rectangular cross-sections could also be used. Such a geometry is natural if the core is made by deforming a sheet. The analysis can be easily adapted to this case, the thermal, elastic and yielding analysis remaining the same, while the bending analysis is only marginally modified by the different moment of inertia of the struts along their axis (the circular cross-section being obviously the most efficient of all).

3.3 Comparison and optimization of the geometry

We give here a summary of the properties previously calculated as a function of the volume fraction of the core. For the honeycomb core, we give results for the regular honeycomb and for the so-called double-wall regular honeycomb (regular honeycomb where 2 walls out of 6 are twice the thickness of the other 4). For the truss panel, we give results for two tetrahedral geometries, one with regular tetrahedrons, one with struts making an angle $\omega = 45°$ with the vertical, all with circular struts. We summarize these results in Tables 3.1 and 3.2.

Several ways of comparing the results are possible. The Figure 3-9 shows what thermal conductivity can be expected of a structure for a given volume fraction (or relative density). The graph itself shows that for a given relative density, lower thermal conductivities can be achieved with truss cores than with honeycombs. Of course, this does not say everything, because the mechanical properties of the truss cores may also be poorer than those of the honeycombs at a given relative density. Nonetheless, there are manufacturing limits (minimum diameter of the struts or minimum thickness of the walls) as well as other mechanical considerations (in particular, bending) that make it desirable to maintain the relative density of the core not too low.

Leaving aside the manufacturing issues, what makes a design more efficient is what mechanical properties we can get for a given thermal conductivity. The elastic properties are investigated first. Figure 3-10 gives the compressive Young's modulus of different structures for a given thermal conductivity. We see that honeycombs are stiffer than truss cores in compression: for a given $\frac{\lambda^*}{\lambda_S}$, honeycomb gives higher $\frac{E^*}{E_S}$, and at lower $\frac{\rho^*}{\rho_S}$. For truss cores, we observe as previously mentioned that the larger the angle, the more compliant in compression the core is. The Figure 3-11 shows the relative shear modulus of a structure for a given thermal conductivity. Several comments are required to understand this graph. The double-wall honeycombs exhibit an in-plane anisotropy, the two lines correspond to the minimum and maximum shear moduli that can be expected, depending on the direction. If the panel is to be loaded in all directions with the same intensity, which is likely, especially for a square panel, a conservative estimate will have to assume the lower shear modulus. Also, while shearing a honeycomb panel will actually shear the walls, relating G^* to G_S, the members of the truss core will be loaded in tension / compression, relating G^* to E_S, so we have to assume a relationship between the elastic moduli G and E to compare the analysis (we assume $\nu = \frac{1}{3}$ here). This shows that truss cores can be stiffer than honeycombs in shear, depending on the angle ω.

Table 3.1: Summary of the analysis of elastic and thermal properties for honeycombs and truss cores

Structure	Young's modulus $\frac{E^*}{E_S}$	Shear modulus G^*	Thermal conductivity $\frac{\lambda^*}{\lambda_S}$
Regular honeycomb	$\frac{\rho^*}{\rho_S}$ (Gibson and Ashby, 1997)	$\frac{1}{2}\frac{\rho^*}{\rho_S}G_S$ $(GibsonandAshby, 1997)$	$\frac{\rho^*}{\rho_S}$
Double-wall regular honeycomb	$\frac{\rho^*}{\rho_S}$ (Gibson and Ashby, 1997)	$G_{13} = \frac{3}{8}\frac{\rho^*}{\rho_S}G_S$ $G_{23} = \frac{9}{16}\frac{\rho^*}{\rho_S}G_S$ .. $\frac{5}{8}\frac{\rho^*}{\rho_S}G_S$ $(GibsonandAshby, 1997)$	$\frac{\rho^*}{\rho_S}$
Regular tetrahedral core panel	$\frac{4}{9}\frac{\rho^*}{\rho_S}$ (Deshpande and Fleck, 2001)	$\frac{1}{9}\frac{\rho^*}{\rho_S}E_S$ (Deshpande and Fleck, 2001)	$\frac{2}{3}\frac{\rho^*}{\rho_S}$
$\omega = 45°$ tetrahedral core panel	$\frac{1}{4}\frac{\rho^*}{\rho_S}$ (Deshpande and Fleck, 2001)	$\frac{1}{8}\frac{\rho^*}{\rho_S}E_S$ (Deshpande and Fleck, 2001)	$\frac{1}{2}\frac{\rho^*}{\rho_S}$

Table 3.2: Summary of the analysis of different failure mode for honeycombs and truss cores

Structure	Compressive strength σ_c^*		Shear strength τ_c^*	
Regular honeycomb (Gibson and Ashby, 1997)	elastic buckling	$3.4(\frac{\rho^*}{\rho_S})^3 E_S$	elastic buckling	$\tau_{13}^* = 4.1(\frac{\rho^*}{\rho_S})^3 E_S$
	plastic yielding	$\frac{\rho^*}{\rho_S}\sigma_{ys}$		$\tau_{23}^* = 3.6(\frac{\rho^*}{\rho_S})^3 E_S$
	plastic buckling	$4.4(\frac{\rho^*}{\rho_S})^{\frac{5}{3}}\sigma_{ys}$		
Double-wall regular honeycomb (Gibson and Ashby, 1997)	elastic buckling	$6.6(\frac{\rho^*}{\rho_S})^3 E_S$	elastic buckling	$\tau_{13}^* = 1.7(\frac{\rho^*}{\rho_S})^3 E_S$
	plastic yielding	$\frac{\rho^*}{\rho_S}\sigma_{ys}$		$\tau_{23}^* = 2.9(\frac{\rho^*}{\rho_S})^3 E_S$
	plastic buckling	$3.2(\frac{\rho^*}{\rho_S})^{\frac{5}{3}}\sigma_{ys}$		
Regular tetrahedral core panel (Deshpande and Fleck, 2001)	elastic buckling	$0.12(\frac{\rho^*}{\rho_S})^2 E_S$	elastic buckling	$\tau_{min}^* = 0.04(\frac{\rho^*}{\rho_S})^2 E_S$
	plastic yielding	$0.67\frac{\rho^*}{\rho_S}\sigma_{ys}$		$\tau_{max}^* = 0.08(\frac{\rho^*}{\rho_S})^2 E_S$
	plastic buckling	?	plastic yielding	$\tau_{min}^* = 0.24(\frac{\rho^*}{\rho_S})\sigma_{ys}$
				$\tau_{max}^* = 0.27(\frac{\rho^*}{\rho_S})\sigma_{ys}$
$\omega = 45°$ tetrahedral core panel (Deshpande and Fleck, 2001)	elastic buckling	$0.12(\frac{\rho^*}{\rho_S})^2 E_S$	elastic buckling	$\tau_{min}^* = 0.035(\frac{\rho^*}{\rho_S})^2 E_S$
	plastic yielding	$0.50\frac{\rho^*}{\rho_S}\sigma_{ys}$		$\tau_{max}^* = 0.07(\frac{\rho^*}{\rho_S})^2 E_S$
	plastic buckling	?	plastic yielding	$\tau_{min}^* = 0.25(\frac{\rho^*}{\rho_S})\sigma_{ys}$
				$\tau_{max}^* = 0.28(\frac{\rho^*}{\rho_S})\sigma_{ys}$

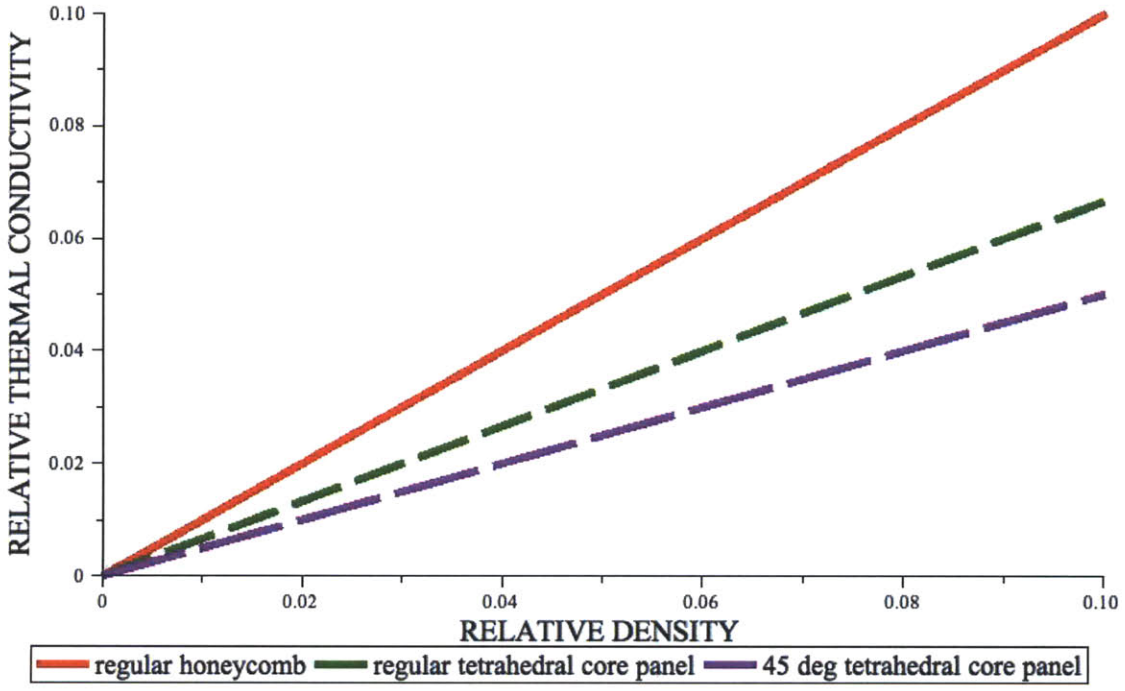

Figure 3-9: Graph showing the expected relative thermal conductivity $\frac{\lambda^*}{\lambda_S}$ of different structures as a function of the relative density $\frac{\rho^*}{\rho_S}$

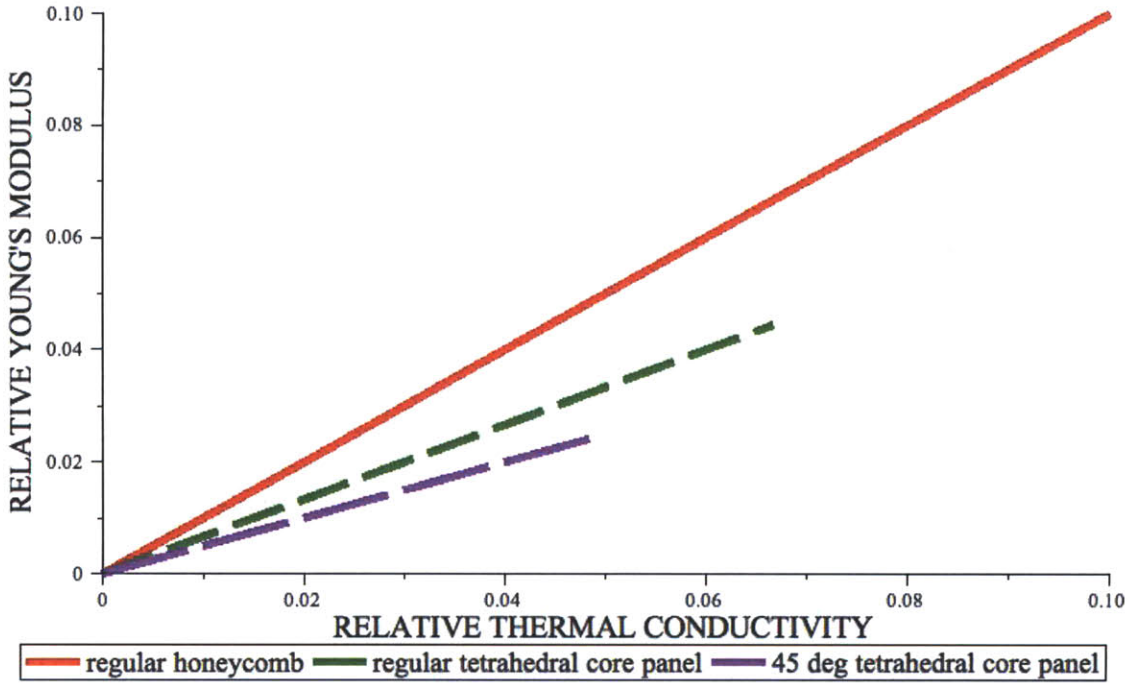

Figure 3-10: Graph showing the expected relative Young's modulus $\frac{E^*}{E_S}$ of different structures for a given thermal conductivity. The lines end at a relative density of 10% and both Young's modulus and thermal conductivity scale linearly with the density.

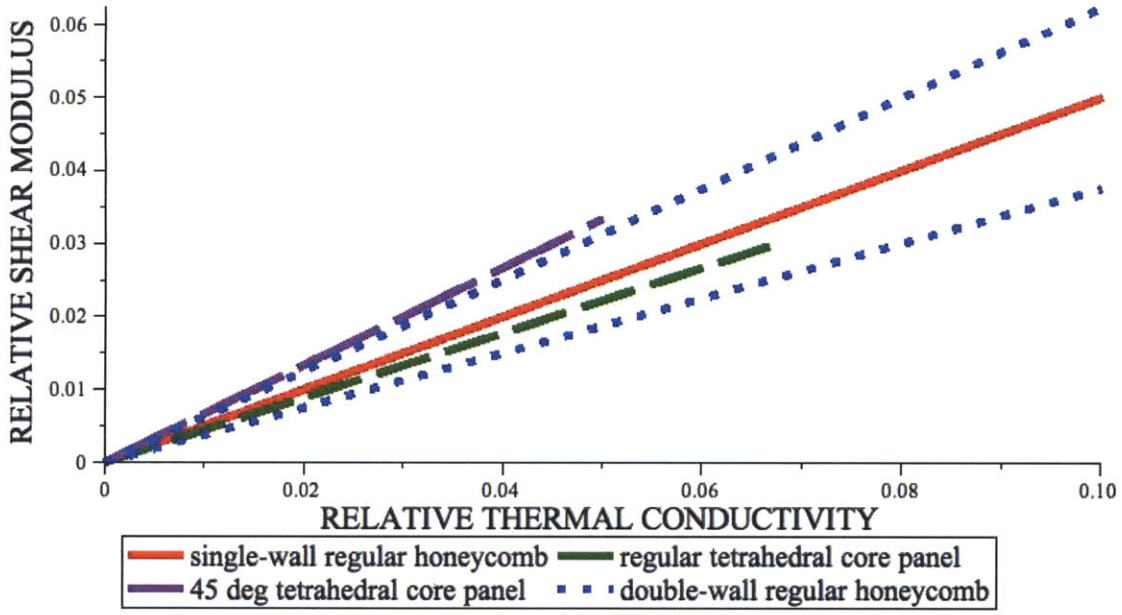

Figure 3-11: Graph showing the expected relative shear modulus $\frac{G^*}{G_S}$ of different structures, assuming $G = \frac{3}{8}E$, for a given thermal conductivity. The lines end at a relative density of 10% and both Young's modulus and thermal conductivity scale linearly with the density.

Finally, the mechanical strength of these structures is also a key property. Both the compressive and the shear strengths for a given thermal conductivity are given in Figures 3-12 and 3-13. The curves exhibit a non-linear part at low $\frac{\rho^*}{\rho_S}$, corresponding to a failure by buckling, while the linear part at higher $\frac{\rho^*}{\rho_S}$ corresponds to a failure by yielding (or a brittle fracture in the case of tensile load). The strengths are given relative to the Young's modulus, assuming a ratio of yield strength to Young's modulus $\frac{\sigma_{ys}}{E_S} = 0.01$, typical of most polymers. The graphs show that honeycombs are worse than truss cores at low relative thermal conductivity, even for compressive strength. Note that the strength of the core is important only if it occurs at a strain lower than that of the aerogel failure, which we want to prevent because it would cause an increase of the thermal conductivity. The strain at fracture of those core could thus be compared to that of the aerogel.

Depending on the criteria that we will define most important, we are now able to perform an optimization analysis.

The last two tables, Tables 3.4 and 3.5, show a case study where the chosen material is polystyrene (see next section). The properties of polystyrene are taken as the median values of those given by the Cambridge Engineering Selector software (Granta Design Limited, 1999), see Table 3.3.

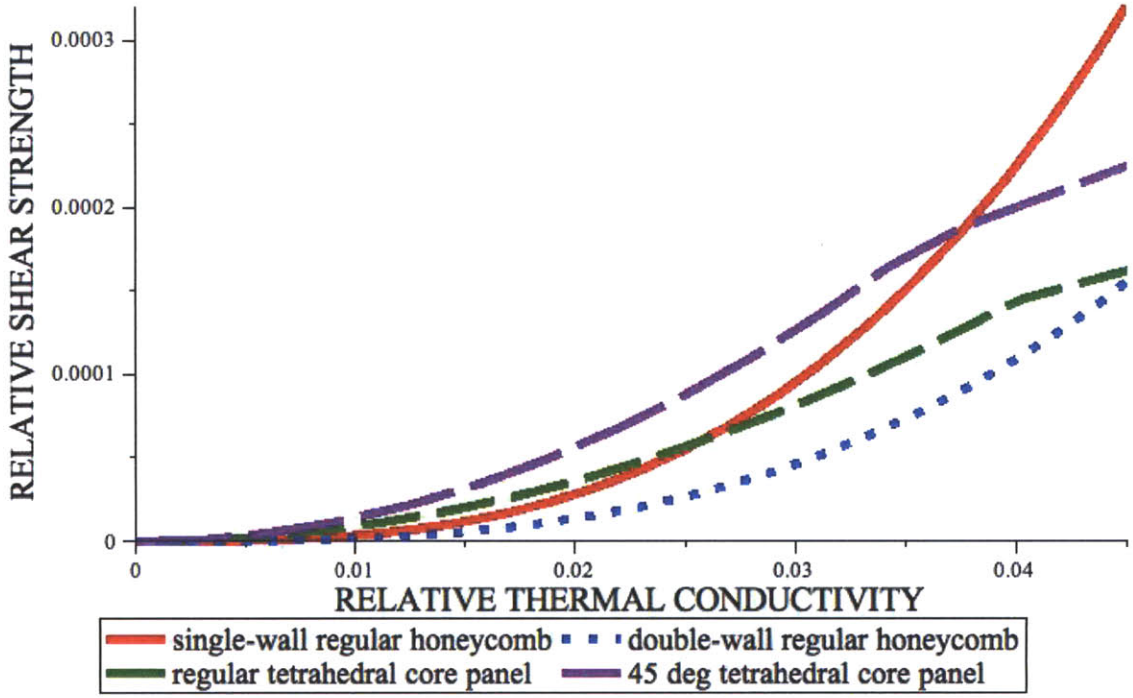

Figure 3-12: Graph showing the expected relative compressive strength of different structures for a given thermal conductivity. The thermal conductivity is linearly dependent on the relative density based on the numbers given in Table 3.1.

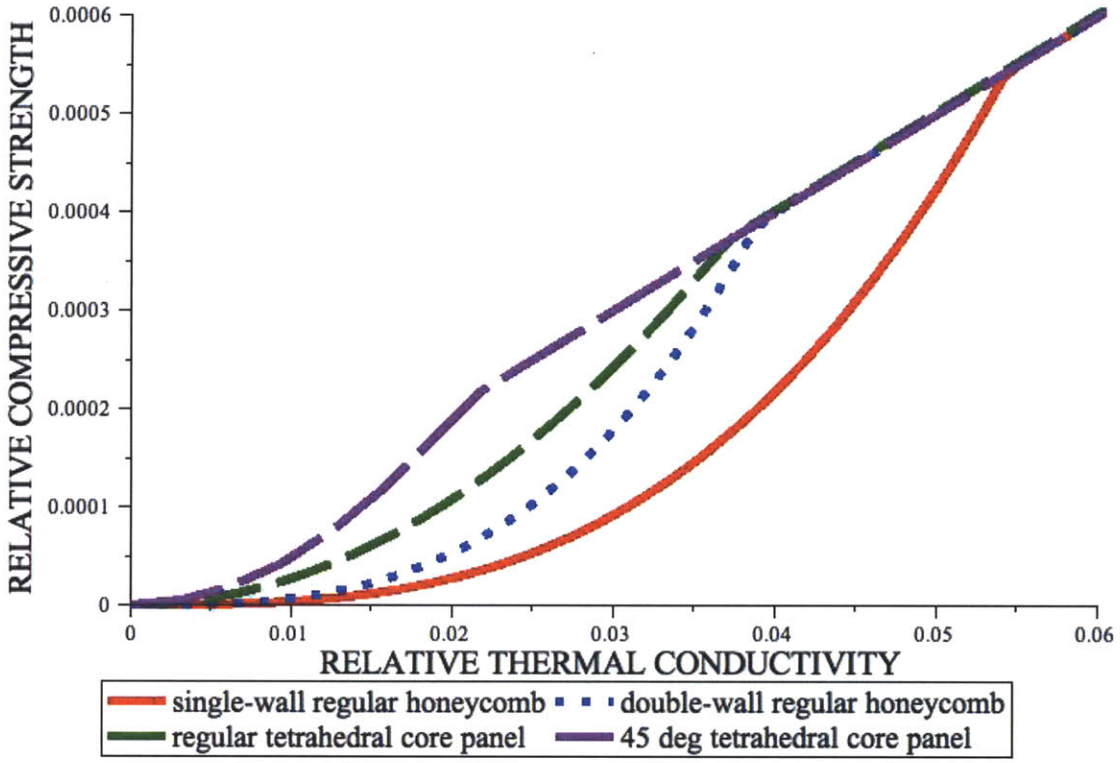

Figure 3-13: Graph showing the expected relative compressive strength of different structures for a given thermal conductivity. The thermal conductivity is linearly dependent on the relative density based on the numbers given in Table 3.1.

Table 3.3: Median properties of polystyrene (Granta Design Limited, 1999)

Density	1.05 kg/m^3
Thermal conductivity	0.126 W/m.K
Young's modulus	2.8 GPa
Shear modulus	1.0 GPa
Elastic limit	42.5 MPa
Tensile strength	46.2 MPa
Compressive strength	89.6 MPa

Table 3.4: Comparison of polystyrene structures each 3% dense

Property	Double-wall honeycomb	Regular tetrahedral core	$\omega = 45°$ tetrahedral core
Thermal conductivity (mW/m.K)	3.8	2.5	1.9
Young's modulus (MPa)	84.0	37.3	21.0
Shear modulus (MPa)	11.3	9.3	10.5
Compressive strength (kPa)	499 (elastic buckling)	302 (elastic buckling)	302 (elastic buckling)
Shear strength (kPa)	129 (elastic buckling)	101 (elastic buckling)	88.2 (elastic buckling)

Table 3.5: Comparison of polystyrene structures having each a thermal conductivity of 2 mW/m.K

Property	Double-wall honeycomb	Regular tetrahedral core	$\omega = 45°$ tetrahedral core
Relative density	1.6 %	2.4 %	3.2 %
Young's modulus (MPa)	44.8	29.9	22.4
Shear modulus (MPa)	6.0	7.5	11.2
Compressive strength (kPa)	75.7 (elastic buckling)	184 (elastic buckling)	344 (elastic buckling)
Shear strength (kPa)	19.5 (elastic buckling)	64.5 (elastic buckling)	100 (elastic buckling)

3.4 Manufacturing of the cores

3.4.1 Choice of the material

The first thing to do is to identify a material that is suitable for our purpose. Many criteria have to be accounted for. If we only consider the elastic properties and the thermal conductivity, we know that these all depend linearly on the core volume fraction, so we need to find the materials that achieve the best ratio $\frac{E}{\lambda}$, where E is the Young's modulus and λ the thermal conductivity. Even so, there is also a manufacturability criteria: between two bulk materials with the same ratio $\frac{E}{\lambda}$, we will choose the one with the lower thermal conductivity, because we can then afford a higher volume fraction to achieve the same core thermal conductivity, probably allowing easier manufacturing.

The choice of the material can be guided by the use of material charts. We used charts using the software Cambridge Engineering Selector (Granta Design Limited, 1999). Two main groups of materials have been identified as possibly suitable for this use: polymer-based materials and wood-based materials. Log-log plots of Young's modulus versus thermal conductivity are given for wood, Figure 3-14, and for common polymers, Figure 3-15. Charts have also been studied for other properties, such as tensile strength. Polymers are found to do slightly better than wood in terms of $\frac{E}{\lambda}$ and other mechanical properties, and in addition the manufacturing process to make the cores seems easier for polymers than for wood. However, the use of polymers in interior insulation panels may raise fire safety issues that we will need to deal with.

Table 3.6 shows E, λ and $\frac{E}{\lambda}$ for the best candidates. Among those, polystyrene is by far the most readily available and is easy to manufacture. Therefore, we are going to study polystyrene truss cores in all the following.

Preliminary calculations based on our analysis show that a 3.2 % dense tetrahedral truss core with $\omega = 45°$ would increase the mechanical properties to an elastic compressive modulus of 18 - 27 MPa

Table 3.6: Comparison of polymers with high $\frac{E}{\lambda}$ ratios

Polymer	Young's modulus E GPa	Thermal conductivity λ W/m.K	Ratio $\frac{E}{\lambda}$ 10^9 s K/m^2
PMMA (Polymethylmethacrylate)	2.24 - 3.8	0.0837 - 0.251	8.9 - 45.4
PS (Polystyrene)	2.28 - 3.34	0.121 - 0.131	17.4 - 27.6
PEI (Polyetherimide)	2.89 - 3.04	0.0644 - 0.0697	41.5 - 47.2
PF (Phenol formaldehyde)	2.76 - 4.83	0.141 - 0.152	18.2 - 34.3
Polyamideimide	4.0 - 17.2	0.149 - 0.6147	6.5 - 115

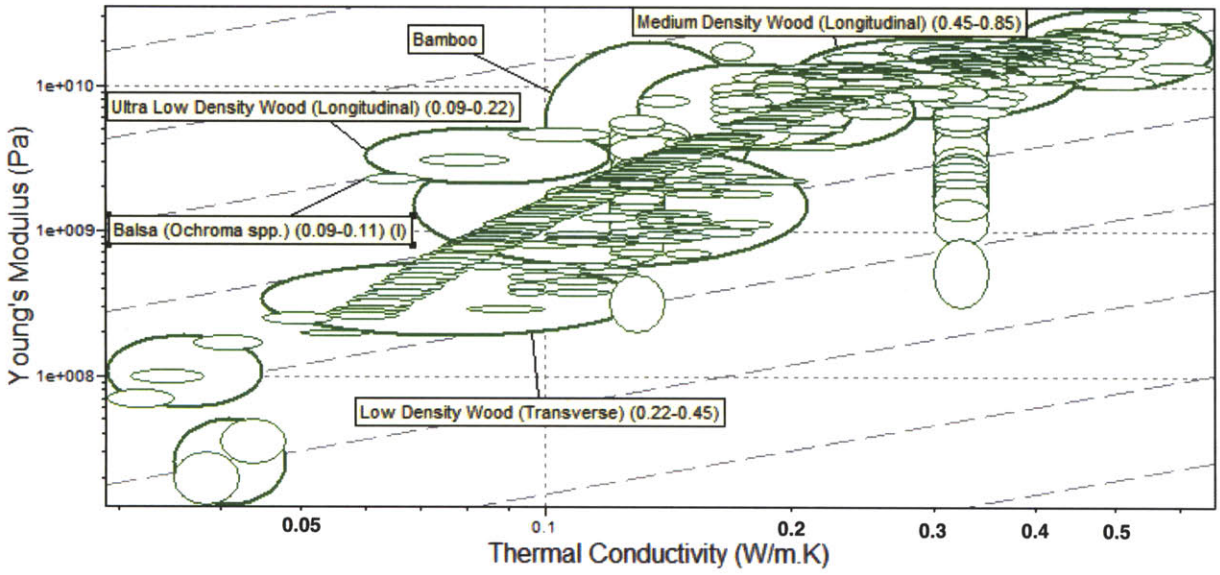

Figure 3-14: Materials chart plotting Young's modulus against thermal conductivity of wood.The dashed lines represent constant $\frac{E}{\lambda}$.

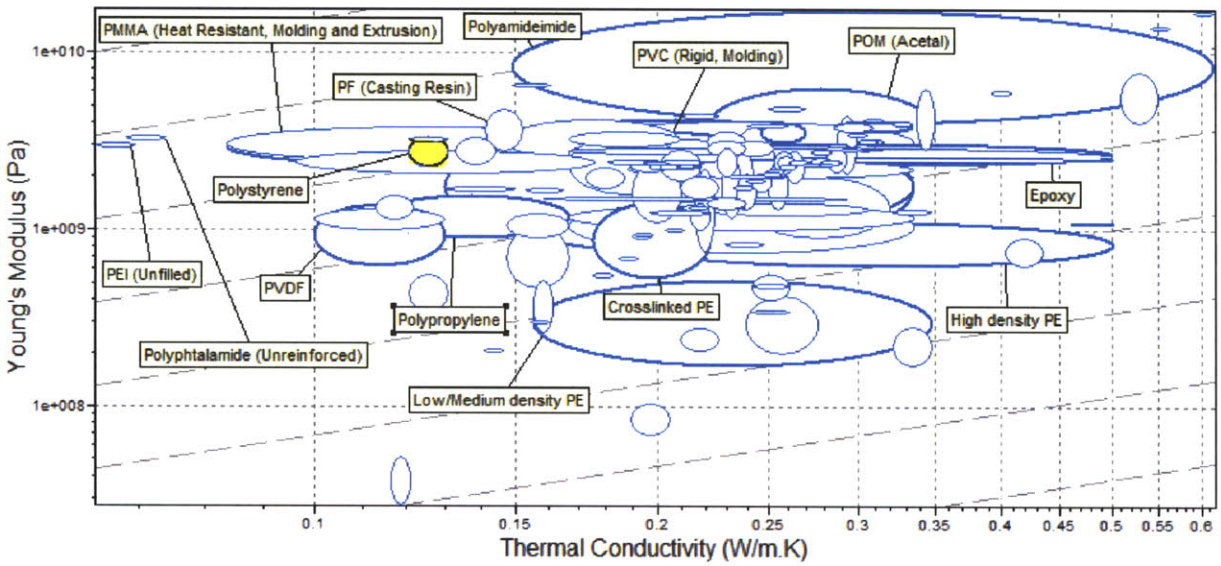

Figure 3-15: Materials chart plotting Young's modulus against thermal conductivity of polymers. The dashed lines represent constant $\frac{E}{\lambda}$.

(versus about 1 MPa for bulk aerogel) and a shear modulus of 9 - 14 MPa (versus about 0.4 MPa for bulk aerogel), while increasing the thermal conductivity by only 2 mW/m.K, see Table 3.5. These calculations give us a reasonable hope that the composite structure would be substantially stiffer and stronger than monolithic aerogel alone.

3.4.2 Injection molding

Injection molding is a method of forming plastic to the desired shape by forcing heat-softened plastic into a relatively cool cavity where it rapidly solidifies. It is extremely cost-effective when producing large quantities, but requires a metal mold.

Over the past years, the research on truss cores has been mainly directed on metal truss cores, see (Deshpande and Fleck, 2001; Wallach and Gibson, 2001; Evans et al., 2001; Chiras et al., 2002; Sypeck and Wadley, 2002; Queheillalt and Wadley, 2005). In several studies (Deshpande and Fleck, 2001; Chiras et al., 2002), the manufacturing route was to make the core by investment casting using a polymer or wax template as a sacrificial pattern. Those templates are usually made by injection molding (Deshpande and Fleck, 2001) or by rapid prototyping (Chiras et al., 2002). It has been possible to obtain regular tetrahedral polystyrene truss cores from some of those previous projects, thanks to N.A Fleck of Cambridge University. One of those core can be seen on Figure 3-16. The polystyrene of those cores is glassy and transparent.

In some other cases (Sypeck and Wadley, 2002; Queheillalt and Wadley, 2005), the metal truss cores have been made directly from metal sheets. The sheet is perforated and then deformed out-of-plane by a punch on a die to make the desired structure. Although attractive, this method did not give good results for polymers in the past (Bouwhuis and Hibbard, 2006) and we did not investigate this fabrication method. The two following sections describe an alternative manufacturing route to make those cores.

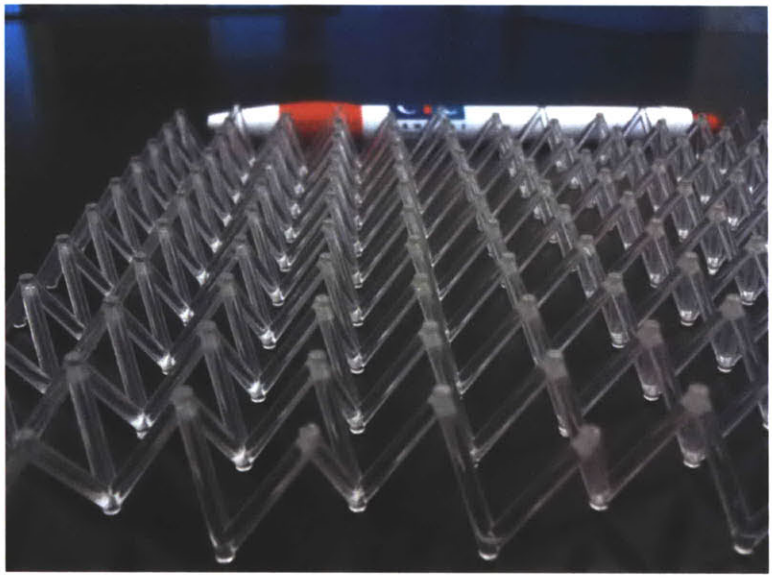

Figure 3-16: A polystyrene truss lattice made by injection molding

3.4.3 Waterjet cutting

The injection molding manufacturing of those cores is very practical for large-scale production. Once the mold is made, hundreds or thousands of cores can be made at very little cost. However, each mold is for one specific geometry associated with this mold. Hence, to study the influence of the geometry (as described by the analysis), we needed to find another way to build cores with different geometries.

The waterjet cutting method has been described in an article by Finnegan et al. (Finnegan et al., 2007). They use waterjet cutting to build carbon fiber composite pyramidal truss sandwich cores. There are two main steps in this method, and the process is illustrated in Figure 3-17.

1. 2-D trusses are designed and cut by waterjet cutting from a sheet of the raw material, see Figure 3-17 - a)

2. The pyramidal lattice is assembled by snap-fitting the truss patterns, see Figure 3-17 - b). At the same time, or possibly in a second step if the snap-fitting is strong enough, the lattice is epoxy-bonded to a face sheet, Figure 3-17 - d).

We applied this method to a polystyrene sheet. This polystyrene differs of that of the injection molded core in that it is entirely white (not transparent) and much more flexible. The trusses were designed using a CAD software, see Figure 3-18, and then cut using an abrasive waterjet cutting machine available

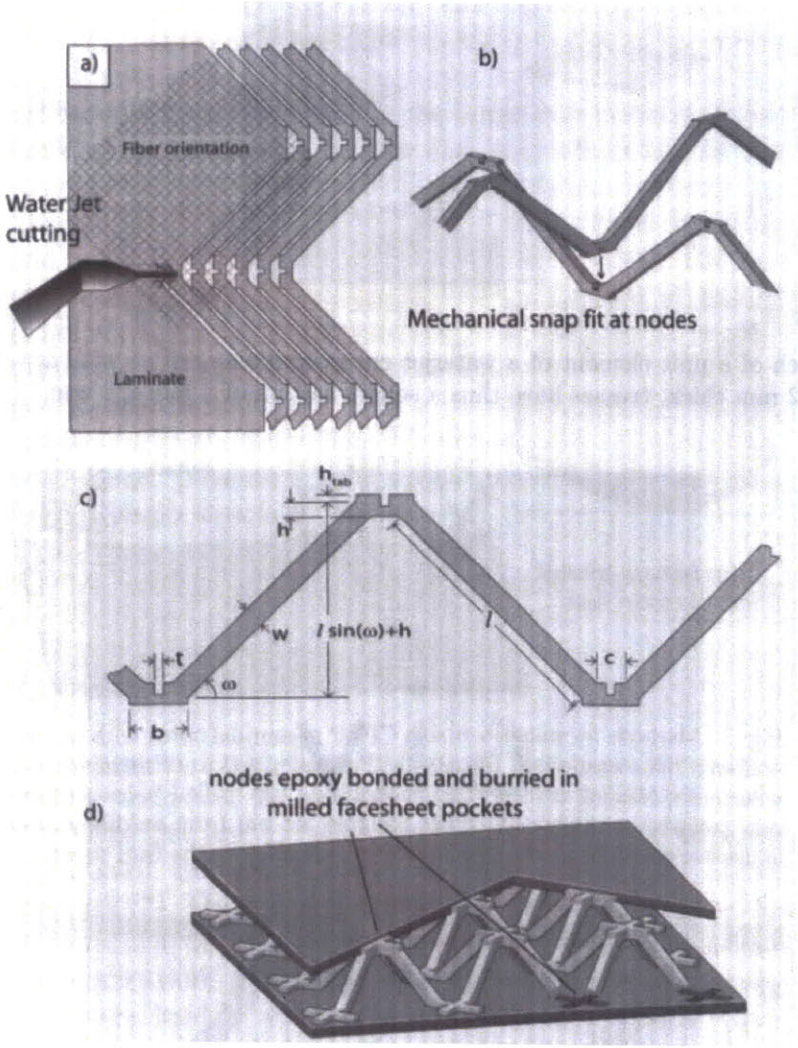

Figure 3-17: Steps of the waterjet cutting method, from Finnegan et al. (Finnegan et al., 2007)

at MIT (OMAX Model 2626, Kent, WA, USA). The result can be seen on Figure 3-19.

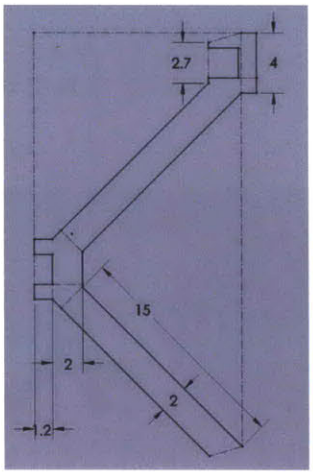

Figure 3-18: Sketch of a unit element of a waterjet cut polystyrene lattice with $\omega = 45°$. Length are in mm. For a sheet 2 mm thick, trusses have thus a square section of 2 mm x 2 mm.

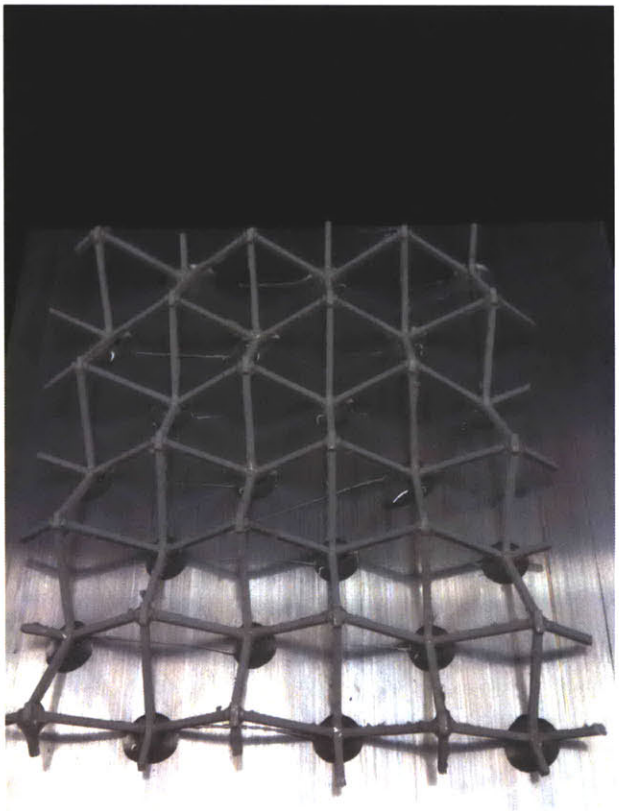

Figure 3-19: Truss lattice made by waterjet cutting epoxy-bonded to an aluminum plate

One of the challenge of this technique is to optimized the opening of the snap-fit. Too small openings make the core hard to assemble and the nodes may not perfectly lie in two parallel planes. On the other hand, too large an opening causes more freedom of rotation in the nodes, and the nodes may not form perfect squares.

3.5 Mechanical testing and comparison with the analysis

3.5.1 Mechanical properties of the polystyrene and relative density of the cores

In order to compare analysis and experiment, we need to know with reasonable accuracy the mechanical properties of the bulk material, polystyrene in our case, and the relative density, or volume fraction, of the cores.

The mechanical properties of the polystyrene vary within a range. For example, according to databases (Granta Design Limited, 1999), the Young's modulus of polystyrene can be found between 2.3 and 3.3 GPa. Therefore, we need to test the specific polystyrene that we are using for our cores. Depending on the manufacturing route, different methods shall be used.

Polystyrene of the injection molded truss specimens

For the injection molded specimens, given the short length of the struts, micro- or nano-indentation techniques are required in order to determine accurately the elastic properties of the polystyrene. A single strut is embedded in epoxy and then polished along its length, and a series of nano-indentation tests are performed using a TriboIndenter™TI-900 (Hysitron, Inc., Minneapolis, MN, USA). The results are then analyzed following the Oliver and Pharr method (Oliver and Pharr, 1992).

We performed the tests on two rods using a nanoindenter with a spherical tip of radius 10 μm. Two loading schemes were used:

1. Load to 500 μm (10 seconds, linearly) - hold (1 second) - unload (10 seconds)
2. Load to 500 μm (10 seconds, linearly) - hold (10 second) - unload (10 seconds)

The holding time is aimed at reducing the effect of creep, since polystyrene is a highly viscoelastic material which relaxes while the load remains constant. The creep typically increases the calculated elastic modulus (VanLandingham et al., 2001; Tweedie et al., 2007). However, the drifting of the machine does not allow for an arbitrary long time of holding (results with 100 seconds of holding were inconsistent).

Series of 25 indentations of each scheme were performed on each rod, for a total of 100 indentations. The average Young's modulus calculated over all the indentations is 3.40 GPa $\pm$ 0.20 GPa, which is in the high range of typical values (2.3 to 3.3 GPa). The longer holding had as expected the effect of reducing the modulus, but only slightly: The average for experiments with 10 seconds of holding time was 0.19

GPa lower than that with 1 second of holding time, or less than 6%. The two rods had the same modulus with accuracy 0.10 GPa. In the end we keep the value of 3.40 GPa given by the overall average.

The relative density of the cores could be determined in two main ways: by weighing the whole core and measuring it, the density of polystyrene being well determined at 1.04 - 1.05 Mg/m^3 (Granta Design Limited, 1999); or by measuring the geometric features (truss diameter and length) and inputing it in a geometric model. The approach using macroscopic measure (weight and sample dimensions) has been chosen for the injection molded cores because of its greater accuracy. The cores that we use have been found to be 4.3% dense.

Polystyrene sheets used for waterjet cutting

For truss samples made from sheets by waterjet cutting, dogbones can be made from the same sheet and then tested in tension according to the ASTM standard D 638 (ASTM International, 2008). A sketch of a dogbone is shown on Figure 3-20. The dogbone is then tested in an Instron machine 4201 (Instron®, Norwood, MA, USA). An extensometer is used to record the strain. The extension speed is 5 mm/s, within the range recommended by the ASTM standard.

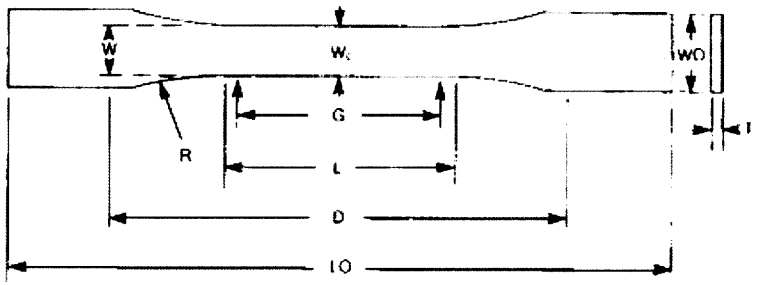

Figure 3-20: Tension test specimen for sheet plastic, from ASTM standard D 638 (ASTM International, 2008)

The typical stress strain response in uniaxial tension is shown on Figure 3-21. The non-linear part at the beginning of the curve corresponds to defaults in parallelism in the initial set-up of the dogbone. One can then observe a perfectly linear part during loading followed by a quasi perfectly plastic behavior. The plastic plateau is between 10 and 12 MPa, lower than that expected after handbooks (Ashby (Granta Design Limited, 1999) gives a tensile strength of 36 - 52 MPa for polystyrene).

It is to be noted that the behavior of the polystyrene is highly viscoelastic, *ie* if the test is stopped

and the dogbone held at a constant strain, the measured stress will decrease.

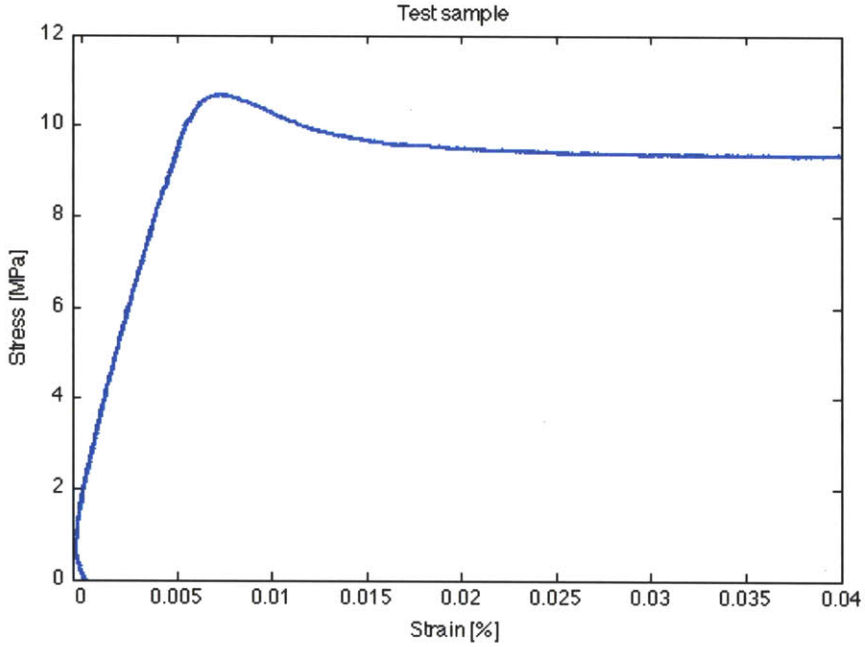

Figure 3-21: Stress-strain curve for an uniaxial tensile test of a polystyrene dogbone

The elastic modulus has been calculated from unloading curves while the polystyrene was still in the linear elastic regime. The Young's modulus is derived from the slope of the unloading curve between 95% and 50% of the maximum. Five dogbones have been tested in this fashion for an average elastic modulus of 2430 MPa $\pm$ 270 MPa (standard deviation), which is within the range given by handbooks.

The compressive strength has also been measured by compressing small parallelepipeds made from the polystyrene sheet (about 2 mm x 2 mm x 4 mm) with the Instron machine 4201. The compressive strength is found to be 43.8 MPa $\pm$ 0.6 MPa, which is lower than the range given by the handbooks (83 - 90 MPa) (Granta Design Limited, 1999), and therefore consistent with the lower than expected tensile strength.

For the waterjet cut samples, the relative density is precisely determined by the design and thus does not require further determination.

3.5.2 Compression tests of the injection molded specimens

We first performed compression tests on the cores made by injection molding. The cores were epoxied (with EASYPOXY ®K-45 Part A Resin, Cytec Industries Inc., West Paterson, NJ, USA) to aluminum plates 1/8" thick as shown in Figure 3-22. They were then compressed using an Instron machine 1321 (Instron®, Norwood, MA, USA). The load is recorded by the load cell and the displacement recorded is the crosshead displacement. The compliance of the machine and of the aluminum plates should be negligible compared to that of the core which is less than 100 MPa. Thus the strain ϵ in the core is calculated as the displacement $\Delta\delta$ over the height (or thickness) h_0 of the core at rest, $\epsilon = \frac{\Delta\delta}{h_0}$. All tests were conducted at the same speed of 0.01 mm/s.

Tests were performed with different sizes of samples. The samples are compressed until failure, which occurs by brittle failure of the trusses. Two typical stress-strain curves are shown on Figure 3-23. The non-linear part at the beginning of the curve is attributed to the imperfect parallelism of the two aluminum plates, perhaps because at some nodes some epoxy remained between the node and the plates despite the load applied during the gluing process. There is a linear region as expected, that is used to derive the Young's modulus of the core (the Young's modulus is calculated based on the points between 30 % and 80% of the maximum stress). After the linear part there is a maximum, corresponding to the time when struts start breaking because they support a compressive load superior to their compressive strength. Then the stress decreases as the strain increases. Two stages of the strut failure are shown on Figure 3-24. Generally, not all struts break during the experiment since the failure of the first struts induces a modification in the geometry that decreases the stress in the other struts. The test is stopped when the stress is clearly decreasing.

Four test results are shown on Figure 3-25, along with predictions based on our model for elastic modulus as well as compressive strength.

From the determination of the polystyrene Young's modulus at 3.40 GPa and of the relative density of the core at the 4.3%, and given that the core is made of regular tetrahedrons, the expected value for the Young's modulus is 65.0 MPa (based on the nanoindentation results). For the standard deviation on the determination of the bulk polystyrene Young's modulus alone, the confidence interval is $\pm$ 3.8 MPa; inaccuracies in the determination of the densities and in the model used for calculation of the core Young's modulus (in particular the limit of the vanishing nodes volume) further increase the extent of this interval.

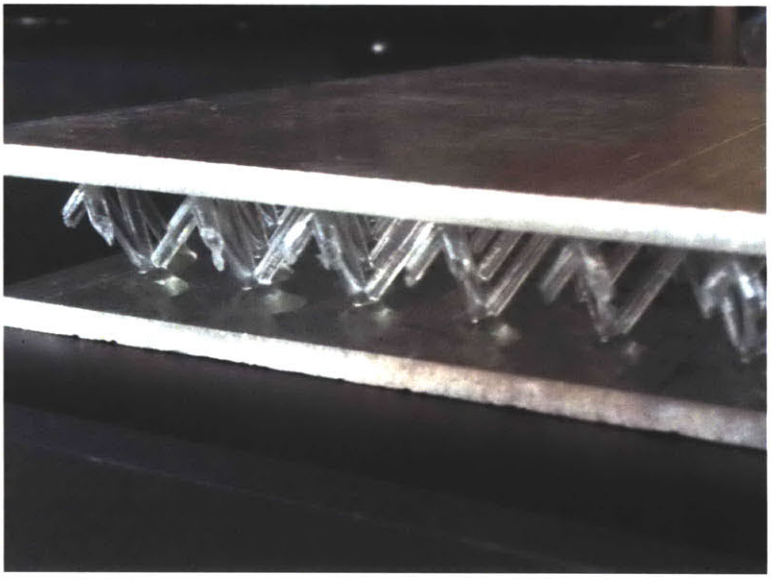

Figure 3-22: A polystyrene truss core between aluminum plates

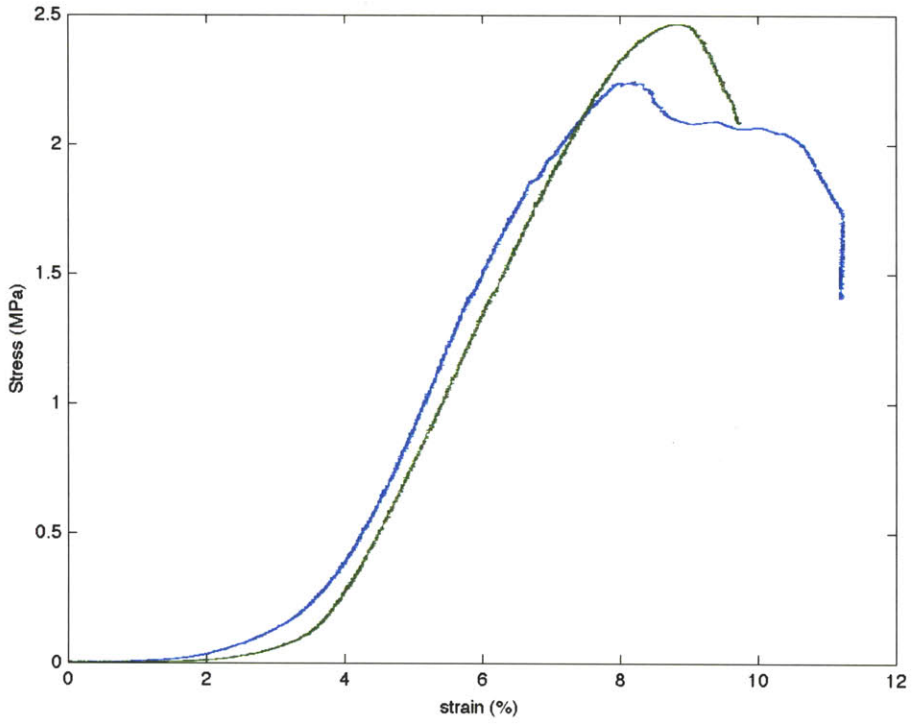

Figure 3-23: Results of the compression tests up to failure for two injection molded specimens.

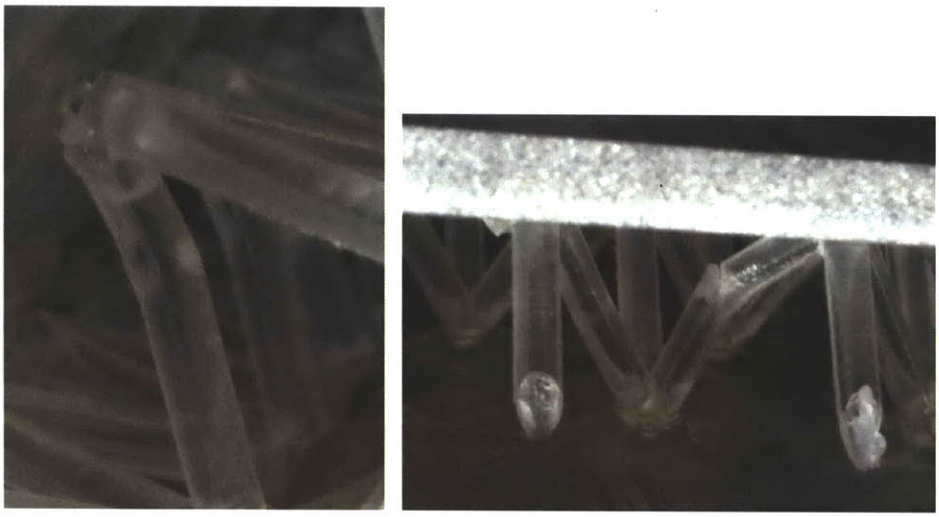

(a) Beginning of the failure. The strut is bent and the polystyrene goes from transparent to white.

(b) Ultimate failure. The strut is broken in two.

Figure 3-24: Polystyrene struts after failure for an injection molded core

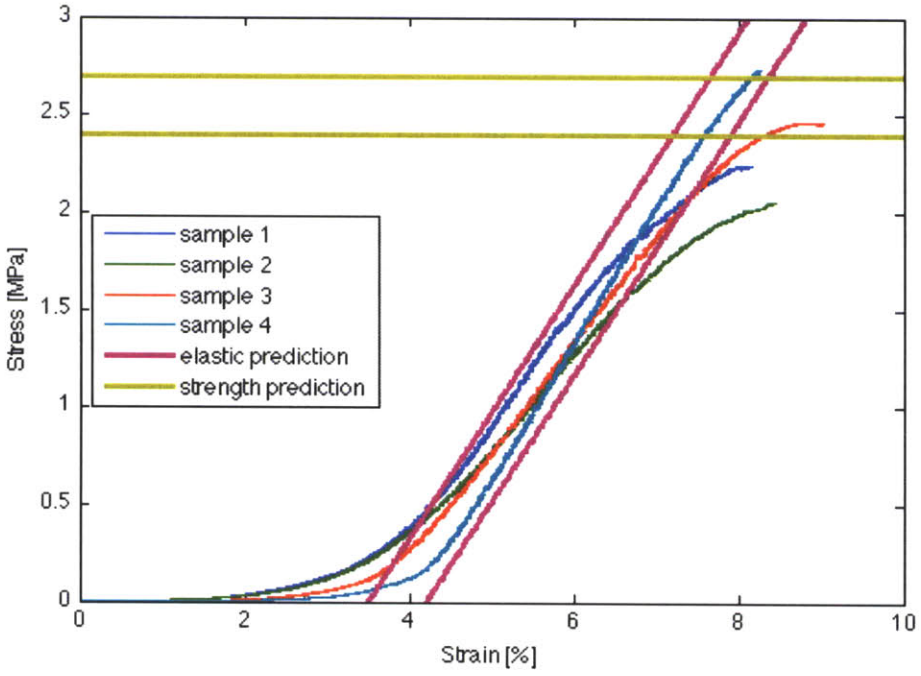

Figure 3-25: Results of the compression tests on injection molded specimens. Elastic predictions lines are of the same slope as guides for the eyes.

The average of all the compression tests gives a compressive Young's modulus for the injection molded cores of 59.8 MPa ± 7.9 MPa (standard deviation). The results are thus completely in line with our prediction.

The average strength at failure, which is taken as the maximum stress supported by the core in the entire uniaxial compression test, is found to be 2.50 MPa ± 0.34 MPa (standard deviation). Based on the average value of compressive strength of polystyrene given in handbooks (83-90 MPa) (Granta Design Limited, 1999), the expected compressive strength of these cores was expected to be 2.47 MPa ± 0.10 MPa.

Results of compressive tests on injection molded polystyrene cores give excellent concordance between experiment and theory for Young's modulus as well as for compressive strength.

3.5.3 Shear tests of the injection molded specimens

Shear tests of the injection molded cores have been done following the ASTM Standard C 273/C 273M (Standard Test Method for Shear Properties of Sandwich Core Materials) (ASTM International, 2007). We built fixtures for the Instron machine in order to comply with the standard requirement; the set-up is shown on Figure 3-26. The displacement is recorded by a LVDT (Linear variable differential transformer) mounted on one of the plates.

The failure in the cores occurs by failure of the epoxy bonding and thus the ultimate strength of the sample is not relevant to the core design (although it raises the question of how it will be bonded to the face material). The linear part stress-strain curve is shown on Figure 3-27. Surprisingly, the measured shear modulus turned out to be higher than predicted, which is uncommon for elastic moduli measurements. Two tests gave the same result of $G^* = 35$ MPa while the expected modulus for this geometry is 16.2 MPa. We cannot explain to date why we measure such high a modulus.

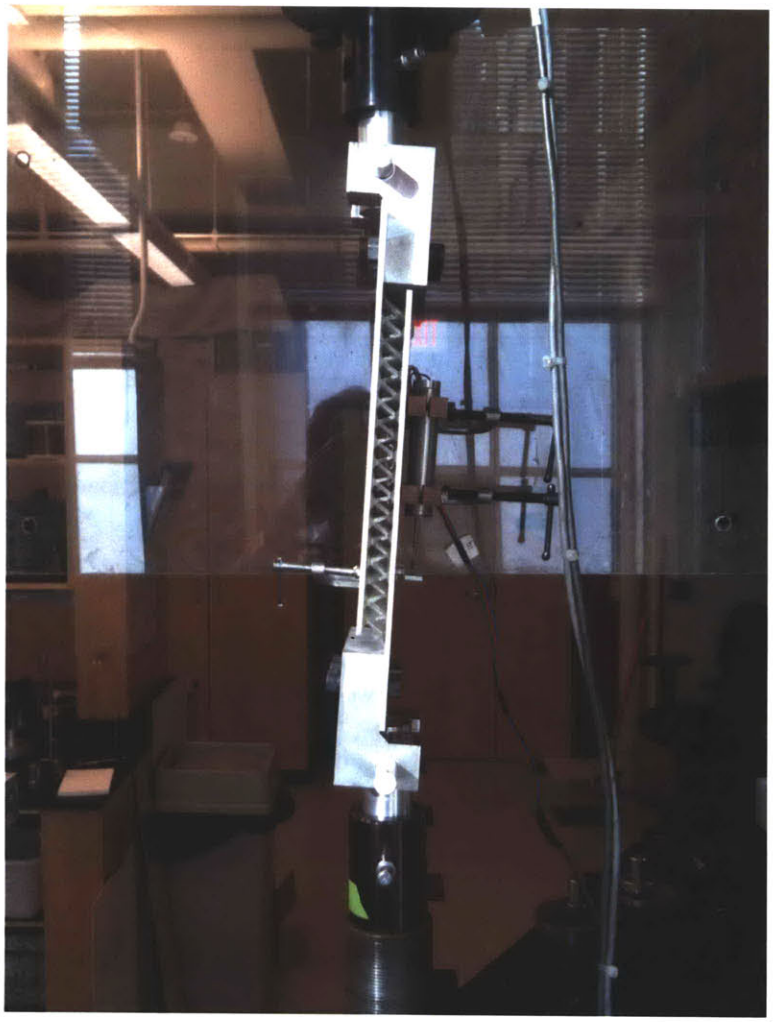

Figure 3-26: Picture of a polystyrene truss core between aluminum plates

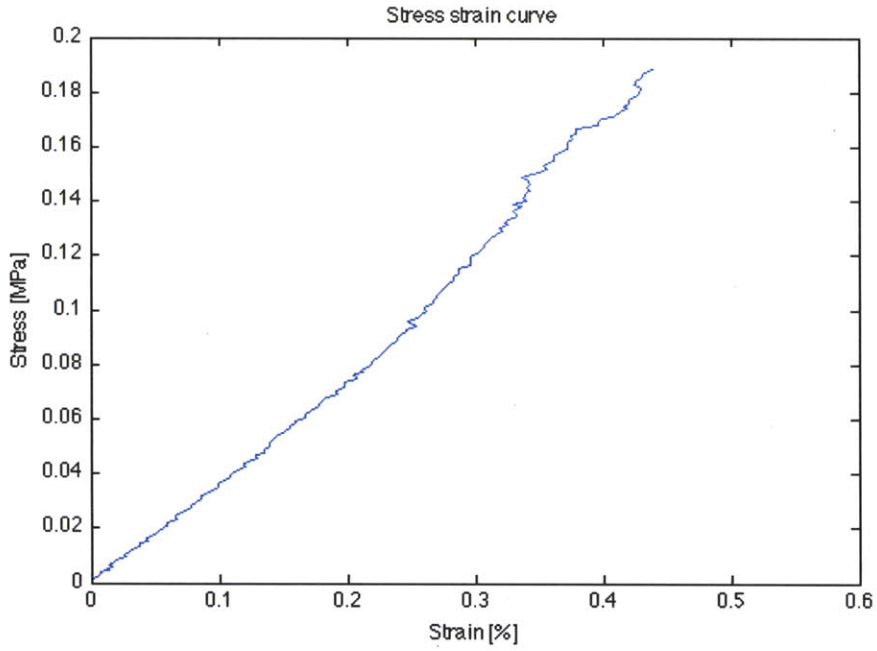

Figure 3-27: Stress strain curve of the polystyrene truss core loaded in shear

3.5.4 Compression tests of the waterjet cut specimens

The purpose of the waterjet cut cores is to study the effect of the geometry on the mechanical properties: Young's modulus and compressive strength. Thus, we fabricated samples with four different relative densities: 3.0%, 4.5%, 6.0% and 7.5%. The density was controlled by the length l of the struts, the node geometry, the truss thickness t and the truss angle ω remaining the same. About 5 samples were made for each density. The cores were epoxy-bonded to aluminum plates in the same way as injection molded cores, see section 3.5.2.

Table 3.7 shows the actual design choices made for the core, largely inspired by one of the designs of the Finnegan et al. study (Finnegan et al., 2007). The parameters are explained on Figure 3-28. The original polystyrene sheet was 0.08 in = 2.03 mm thick, thus the value of w is also 2.03 mm so that the struts have a square cross section. The value of t for the width of the opening for the snap-fit mechanism has been optimized at 2.15 mm in the trial-and-error process as the best value for snap-fitting: lower values lead to insufficient snap-fitting and thus cores insufficiently parallel, while higher values allow for too much rotation in the node. Finally, the angle ω is chosen equal to 45°.

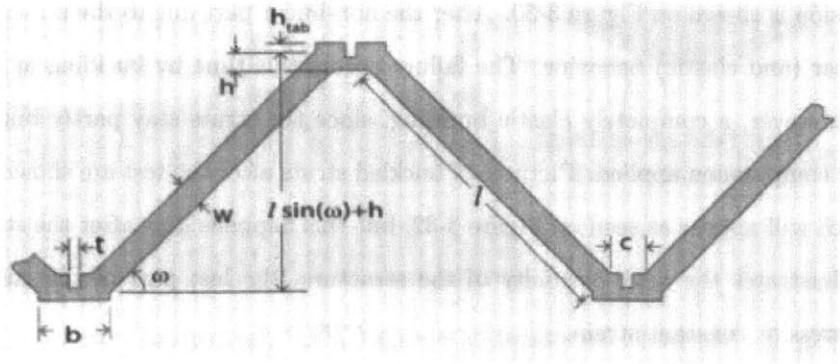

Figure 3-28: Geometry of the trusses made by the waterjet cutting technique

Table 3.7: Design chosen for waterjet cut cores. Parameter names are the same as in Figure 3-28. Values are given in mm.

h_{tab}	h	w	t	c	b
1.30	1.90	2.03	2.15	2.70	4.00

The density and the length of the struts are related through the equation

$$\frac{\rho^*}{\rho_S} = \frac{2(lt + hb)t}{l \sin\omega(l\cos\omega + b)^2}$$

which can be reduced, in the limits of vanishing node volumes to

$$\frac{\rho^*}{\rho_S} \simeq \frac{4t^2}{l^2 \sin 2\omega \cos\omega}$$

although, as we indicated in section 3.2.2, the two may differ quite significantly (from about 30% for a relative density of 5%), and we will thus always use the exact formula. Table 3.8 shows the lengths corresponding to the chosen densities.

The samples were tested in the same way as the injection molded ones. The experimental set-up is shown on Figure 3-29. The waterjet cut core behave slightly differently than the injection molded ones, because of the different geometry and of the different polystyrene used. The typical stress strain curve in

Table 3.8: Length l (in mm) of the struts for the chosen densities

density	3.0%	4.5%	6.0 %	7.5%
l	14.30	16.38	19.42	24.55

uniaxial compression is shown on Figure 3-30. After the non-linear part due to the imperfect parallelism, we observe a linear (and elastic) behavior. The failure occurs this time by buckling of the struts. This buckling is not, however, a completely elastic buckling, since the struts stay partly buckled even when there is no longer compression applied. Pictures of buckled struts after the test are shown on Figure 3-31. Eventually a notch will appear as seen on Figure 3-32, but this happens long after the strut has buckled. The curve also illustrates the visco-elasticity of the structure, the last part of the curve exhibiting a decrease in the stress at constant strain.

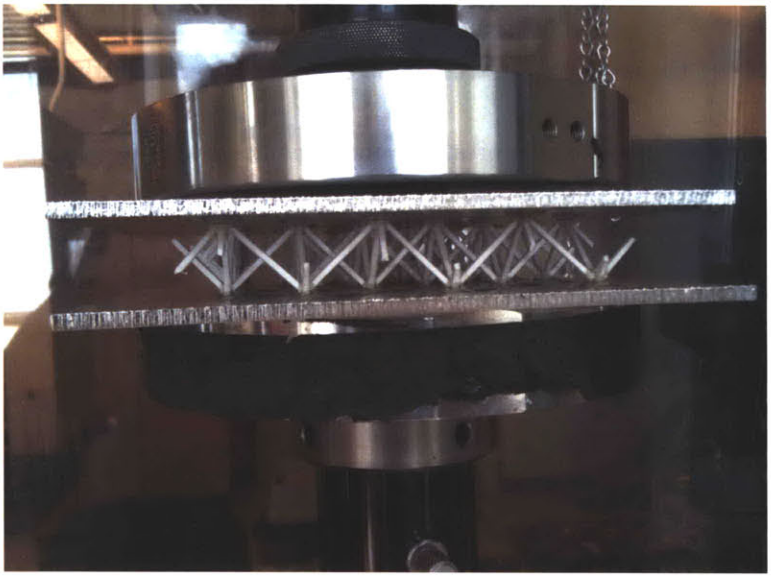

Figure 3-29: Set-up for the compression test of the waterjet cut polystyrene core

The graph showing the average compressive Young's modulus as a function of the density is shown on Figure 3-33. The first prediction is based on the model of Deshpande et al. (Deshpande and Fleck, 2001) assuming pin-jointed trusses with vanishing node volume. The second prediction is based on the beam model developed by Finnegan et al. (Finnegan et al., 2007) with non-zero volume at the nodes. The two predictions are based on the value of the polystyrene Young's modulus of 2.43 GPa $\pm$ 0.27 GPa measured in tensile tests. Both those models lead to an overestimate of the actual value of the Young's modulus of 30 to 40%. Also, it seems that for higher densities, $\frac{\rho^*}{\rho_S} > 6\%$, the Young's modulus is no longer a linear function of the core relative density. The results seem more satisfactory if restricted to the lower values of density (shown along with the first prediction), see Figure 3-34.

As for the ultimate strength in compression (taken as the maximum stress recorded during the ex-

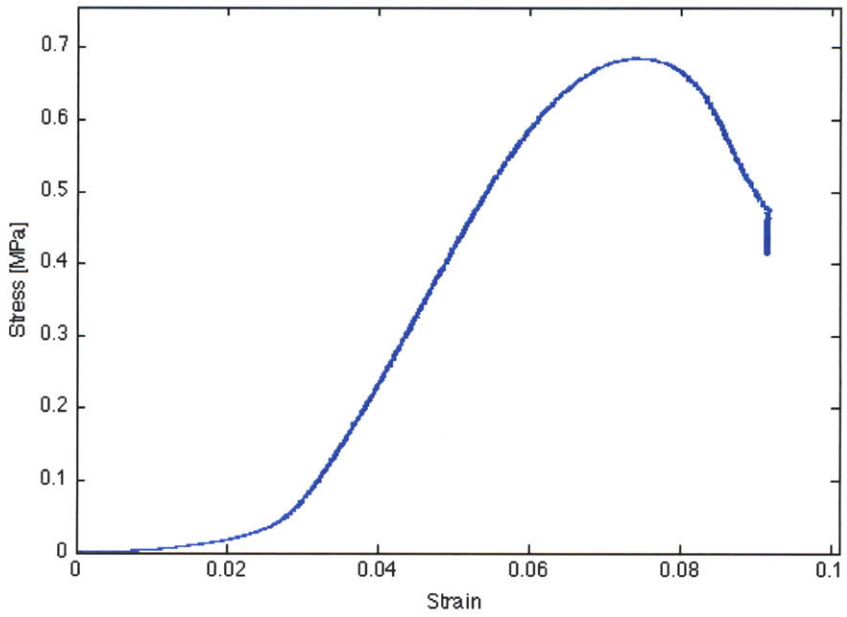

Figure 3-30: Stress strain curve of a waterjet cut core 6% dense in uniaxial compression

Figure 3-31: Buckled polystyrene struts after the compression of a waterjet cut core

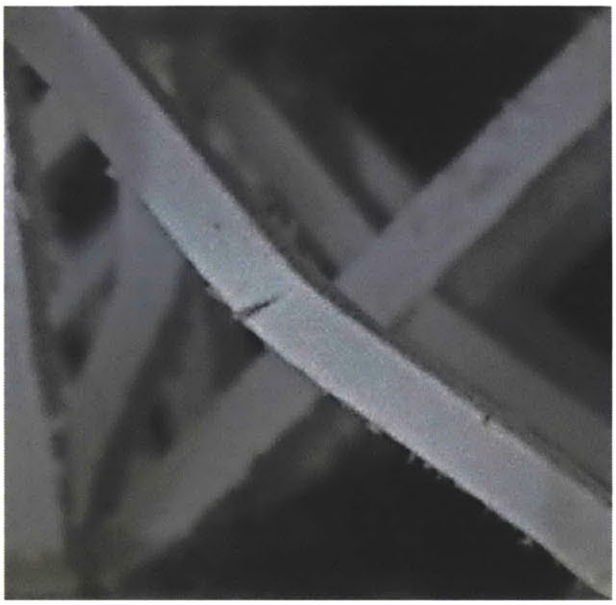

Figure 3-32: Buckled polystyrene strut exhibiting a notch after compression

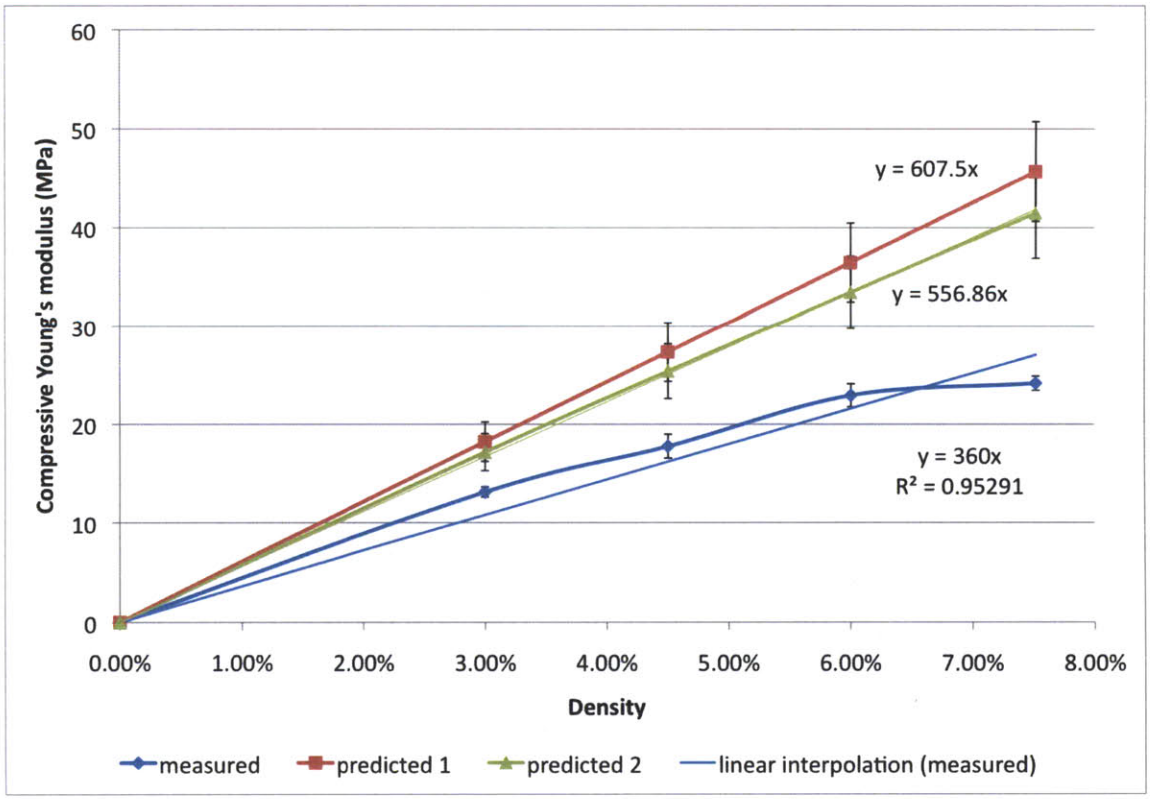

Figure 3-33: Calculated and predicted Young's modulus of a waterjet cut core as a function of the relative density in uniaxial compression

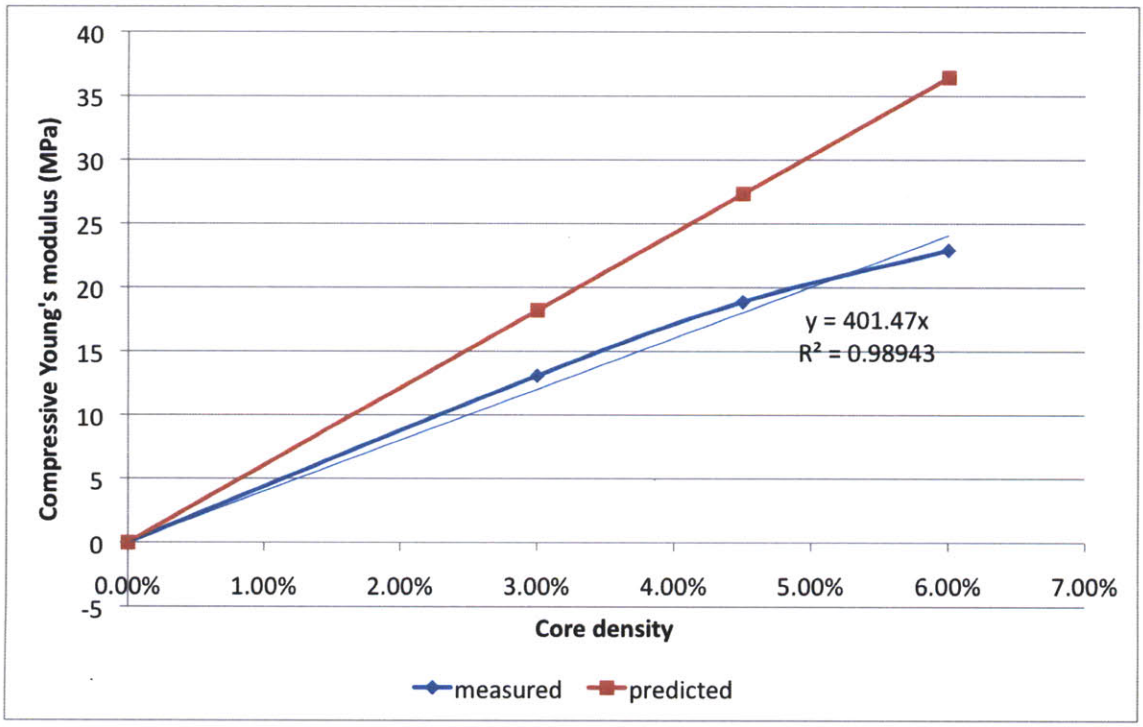

Figure 3-34: Calculated and predicted Young's modulus of a waterjet cut core as a function of the relative density in uniaxial compression for densities lower than 6%

periment), the results as function of the density are shown on Figure 3-35. The strength seems to have a linear behavior as a function of the density, typical of a failure occurring by yielding of the struts. We thus believe that the failure occurs first by local yielding of the struts introducing immediately a disequilibrium which conducive to plastic buckling. The slope of the strength vs density experimental curve is 26 % lower of that expected for yielding (from the measured compressive strength of the polystyrene from our sheets, 43.8 MPa $\pm$ 0.6 MPa). We show also predictions for elastic buckling, based on the measured polystyrene Young's modulus of 2.43 GPa, with different end constraint factors k ($1 \leqslant k \leqslant 4$ in the Euler buckling formula $P_{cr} = \frac{k\pi^2 E_S I}{l^2}$). For $k \geqslant 2$, intermediate between pinned ends and fixed ends, it is expected that the mode of failure be yielding since the buckling limit is higher that the yielding limit for the observed densities.

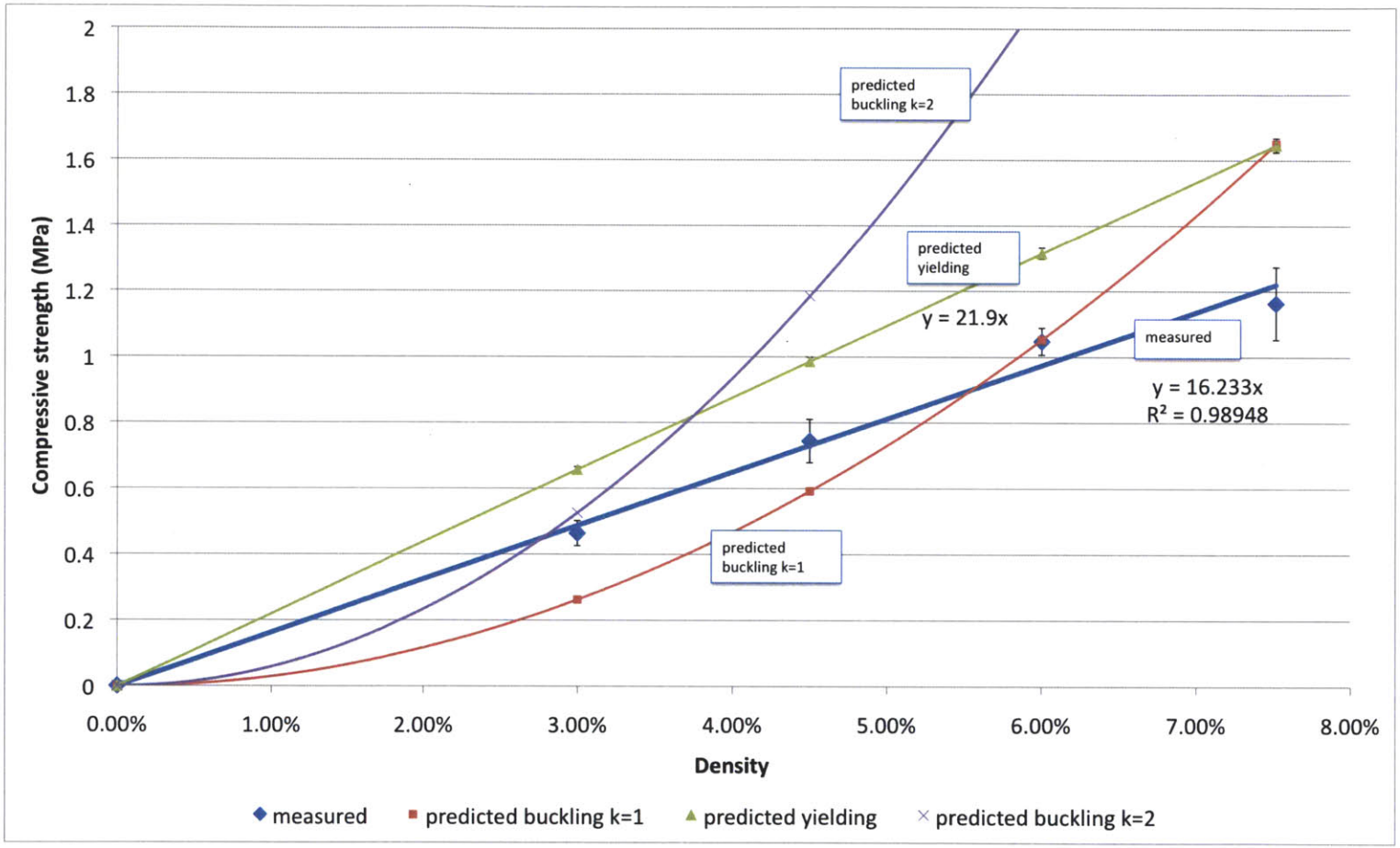

Figure 3-35: Calculated and predicted compressive strength of a waterjet cut core as a function of the relative density in uniaxial compression

3.6 Conclusion

We have done an analytic and experimental work to validate the use of truss cores as a structural component in an insulation panel. Polystyrene truss cores have been tested and the results agree with the analysis with a reasonable margin of error. Mechanical criteria for a mechanically efficient panel have still to be determined in order to optimize the structure.

In the next chapter, we study what would a complete aerogel insulation panel to look like. Specifically, we now need to focus on the combination of a core and of faces. We will then try to build such a panel, knowing that the incorporation of the aerogel into the truss core is not going to be an easy task, due to the shrinkage during the drying process.

Chapter 4

Design concepts for composite panels

4.1 Introduction

In this chapter, we are going to study a series of potential designs for a thermal insulating panel. This chapters focuses primarily on rigid insulation panels, although alternate design ideas for flexible panels will be discussed later in the chapter.

4.2 Design choices

4.2.1 Dimensions

We are going to consider small panels of 30 cm x 30 cm (about 1 ft x 1 ft). Those panels are relatively small panels, which is necessary in the case where we have a vacuum to maintain (since we don't want to lose all the benefits of the vacuum if the wall is punctured in one point). Also, it reduces the risk of breaking a sample during synthesis.

We will study two different thicknesses:

- A core 1 inch thick with faces each 1/16 inch thick (SI units: 25.4 mm for the core and 1.59 mm for the faces)
- A core 1/2 inch thick with faces each 1/32 inch thick (SI units: 12.7 mm for the core and 0.79 mm for the faces)

We believe that these thicknesses, relatively small, are interesting for a high insulator such as aerogels, whose main purpose is to reduce the thickness of the insulation required to achieve superior thermal insulation.

4.2.2 Core

In this chapter, we are going to consider 4 options for the core: 2 truss cores and 2 honeycomb cores. All the cores will be designed to have a solid thermal conductivity of 2 mW/mK.

The truss cores considered are both polystyrene tetrahedral truss core. One has an angle ω=45°(optimal geometry for shear modulus) and one has an angle ω=39.2°(optimal geometry for buckling strength at a given density). The geometry of truss cores has been discussed in chapter 3. Figure 4-1 recalls the geometry parameters.

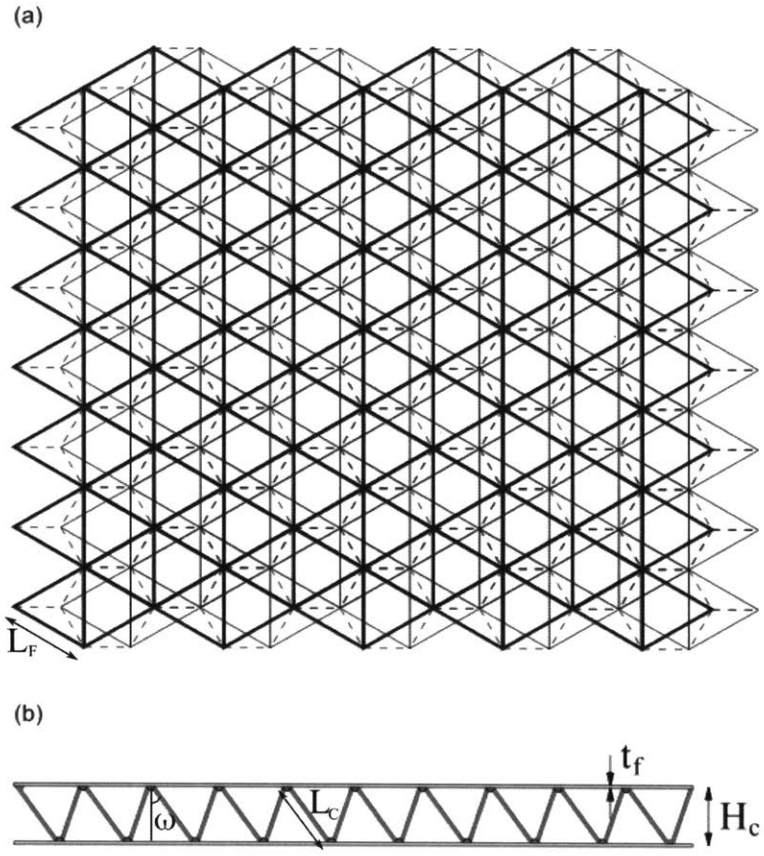

Figure 4-1: Geometry of a tetrahedral core panel, from Wicks and Hutchinson (Wicks and Hutchinson, 2001)

The first honeycomb core considered is a regular polystyrene honeycomb in order to have a direct comparison with the polystyrene truss cores. The second honeycomb core considered is a regular paper honeycomb with one wall out of three of double thickness, which is more realistic from a manufacturing point of view.

4.2.3 Faces

The faces of a sandwich panel have several functions. They provide most of the panel stiffness when it is bent. It also protects the core material from indentations by spreading the load on a larger area than the initial punch. It can also provide additional benefits such as protection from water or from fire. Finally, coupled with a membrane it can help maintain a vacuum.

From an industrial perspective, face materials have to be relatively cheap and easy to manufacture. It is attractive to use a material already in use in the building industry to make use of existing knowledge and infrastructure. With this in mind, three major categories of materials were identified: cement-based, wood-based and polymer-based materials.

Cement based materials were ruled out since a very thin cement layer is weak (brittle) in tension. It is possible to increase the tensile strength by reinforcing the cement, for example with paper fibers or polymer fibers. However, this increases the difficulty and the cost of making such faces. Furthermore, the thinness (1/16 in or 1/32 in) still adds more challenge to the manufacturing.

Therefore, we are going to consider only two different face materials. The wood-based material will be a generic wood widely used in construction, pine; for the sake of simplicity, the polymer-based material will be polystyrene, as in the truss cores.

4.2.4 Summary

In total, we are going to study 16 different designs for a rigid aerogel panel, as seen on Table 4.1.

We also are sometimes going to compare the design by replacing the core structure by pure aerogel, to give an idea of the improvements brought by the core.

Table 4.1: Designs considered for an aerogel rigid insulation panel

Dimension	Core type	Face	Design number
horizontal: 30 cm x 30 cm vertical: core 25.4 mm thick faces 1.59 mm thick	polystyrene tetrahedral core 45°	polystyrene	1
		pine	2
	polystyrene tetrahedral core 39.2°	polystyrene	3
		pine	4
	polystyrene regular honeycomb	polystyrene	5
		pine	6
	paper regular double-wall honeycomb	polystyrene	7
		pine	8
horizontal: 30 cm x 30 cm vertical: core 12.7 mm thick faces 0.79 inch thick	polystyrene tetrahedral core 45°	polystyrene	9
		pine	10
	polystyrene tetrahedral core 39.2°	polystyrene	11
		pine	12
	polystyrene regular honeycomb	polystyrene	13
		pine	14
	paper regular double-wall honeycomb	polystyrene	15
		pine	16

4.3 Calculations

4.3.1 Material Properties

Most of the properties that we use here are obtained from the Cambridge Engineering selector (Granta Design Limited, 1999) which compiles data from handbooks and articles. We will take the mean properties for each material we consider, even though in some case it may be possible to have a better combination of properties for a given material. All the properties we need are given in Table 4.2.

Table 4.2: Median properties of the materials used in this study (Granta Design Limited, 1999)

	Polystyrene	Paper	Pine
Density (kg/m^3)	1.05	0.95	0.49
Thermal conductivity (W/m.K)	0.126	0.258	0.082 (transverse)
Young's modulus (GPa)	2.78	3.00	0.76 (transverse) 9.35 (longitudinal)
Shear modulus (GPa)	1.00	1.50	0.09 (transverse) 0.69 (longitudinal)
Compressive strength (MPa)	86	48	5 (transverse)
Tensile strength (MPa)	44	25	3.6 (transverse)
Poisson's ratio	0.39	0.38	0.03 (transverse) 0.38 (longitudinal)

4.3.2 Determination of the cores densities and panels weights

We next derive a density for the cores so that all the cores have a solid thermal conductivity of 2 mW/mK. All the formulas used here come from the previous chapter (chapter 3).

1. Polystyrene truss core ($\omega = 45°$): The formula $\frac{\lambda^*}{\lambda_S} = \cos^2(\omega)\frac{\rho^*}{\rho_S}$ (Equation (3.29)) gives a density $\frac{\rho^*}{\rho_S} = 3.2\%$

2. Polystyrene truss core ($\omega = 39.2°$): The same formula yields $\frac{\rho^*}{\rho_S} = 2.6\%$

3. Polystyrene single wall regular honeycomb: The formula for honeycombs is simply $\frac{\lambda^*}{\lambda_S} = \frac{\rho^*}{\rho_S}$ (Equation (3.8)). In this case we find $\frac{\rho^*}{\rho_S} = 1.6\%$

4. Paper double wall regular honeycomb: We have the same formula but the thermal conductivity of paper being twice as much as that of polystyrene we find $\frac{\rho^*}{\rho_S} = 0.8\%$

We can now calculate the weight of a single panel (30 cm x 30 cm), assuming the rest of the core is filled with aerogel at density 0.120 g/cm^3, which is close to the optimum in terms of thermal conductivity. The weight of a panel for each design is given on Table 4.3. Note that aerogel still accounts for about 300 g in each of the bigger panels (designs 1 to 8), between 1/2 and 2/3 of the total weight. The truss or honeycomb core accounts for a maximum of 70 g (for the ω=45°one, the densest one), with the faces accounting for the rest of the total.

Table 4.3: Weight of a single panel for each design. Each design number is described on Table 4.1

Design number	total weight (kg)
1	0.64
2	0.48
3	0.63
4	0.47
5	0.61
6	0.45
7	0.59
8	0.43
9	0.32
10	0.24
11	0.32
12	0.24
13	0.30
14	0.22
15	0.29
16	0.21

4.3.3 Thermal properties

The core structures have now been scaled so that all cores have a thermal conductivity of 2 mW/mK. We will consider the thermal diagram on Figure 4-2 to compute the total thermal resistance. Note that this diagram is simplified in several ways. First, we consider that there is no interaction between the aerogel and the truss structure (we calculate the two as being in parallel, *ie* we add the conductances). This seems to be a reasonable approximation since the thermal conductivity of the polystyrene is more than ten times higher than that of aerogel. We also consider that there is a perfect thermal contact between the face and the truss or honeycomb structure, while in fact the structure is in contact with the face only over a limited area. This leads to some horizontal thermal flux in the faces and finally to an increase of the total resistance. In this case our simplification thus gives a lower bound for the thermal resistance; also the increase of the resistance due to this phenomenon has been estimated to be low.

We take the thermal conductivity of the aerogel to be 10 mW/mK. Most aerogels in this study indeed have thermal conductivity between 9 and 10 mW/m.K at atmospheric pressure (Zuo, 2010).

We can now calculate the R-value, R-value per inch and thermal conductivity for all our designs. Note that since the dimensions of the faces and of the core remain in the same proportion, the thermal conductivity (equivalent to the R-value per inch) are the same for the two dimensions; only the actual R-values change. The values are shown in Tables 4.4 and 4.5.

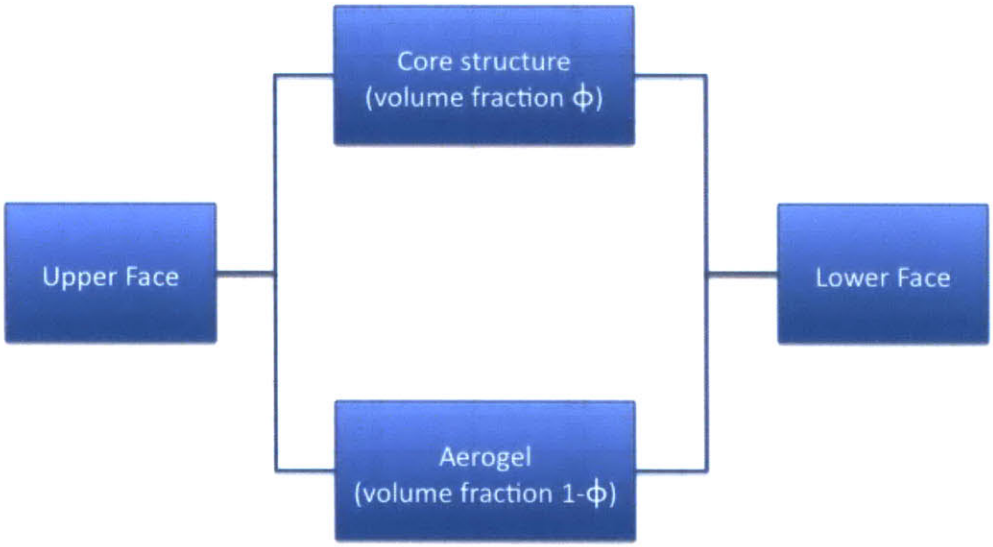

Figure 4-2: Thermal diagram for the calculation of the overall thermal resistance of the panel. The truss or honeycomb core has volume fraction $\Phi = \frac{\rho^*}{\rho_S}$ and the aerogel fills the rest of the core with volume fraction $1 - \Phi$

Table 4.4: Global thermal conductivity and thermal resistance per inch of each design for an aerogel thermal conductivity λ=10 mW/m.K

Design number	global thermal conductivity (mW/mK)	R-value per inch (imperial, $\frac{ft^2°F\ h}{Btu\ in}$)
1 and 9	12.99	11.10
2 and 10	12.91	11.17
3 and 11	13.05	11.05
4 and 12	12.97	11.12
5 and 13	13.17	10.95
6 and 14	13.09	11.02
7 and 15	13.26	10.88
8 and 16	13.17	10.95

Table 4.5: Thermal resistance of each design

Design number	R-value (SI, $\frac{m^2K}{W}$)	R-value (imperial, $\frac{ft^2°F\ h}{Btu}$)
1	2.20	12.49
2	2.21	12.57
3	2.19	12.43
4	2.20	12.51
5	2.17	12.32
6	2.18	12.40
7	2.16	12.24
8	2.17	12.32
9	1.10	6.24
10	1.11	6.28
11	1.09	6.22
12	1.10	6.25
13	1.09	6.16
14	1.09	6.20
15	1.08	6.12
16	1.08	6.16

The thermal conductivities of all the designs are all very close, around 13 mW/mK, or R-11 per inch (imperial units). The cores have indeed all the same conductivity, the difference in aerogel volume is small between the designs, and the faces are thin enough to have only a moderate effect. Note that the option of a panel only 9/16 inch thick still provides an insulation of more than R-6 (imperial units), while conventional insulations needs at least one inch thickness to achieve the same result.

We can also compute the thermal properties for the case of a reduced vacuum (between 1/10 and 1/3 of an atmosphere), with a thermal conductivity of 5 mW/mK for the aerogel (see Figure 4-3, (Cohen, 2011)). In that case, we find a R-value per inch between 18 and 19. The best designs (designs 2 and 10) have in this case an R-value of 18.94 per inch, ie R-21.30 for design 2 and R-10.65 for design 10.

Of course, the differences between the 16 designs in terms of thermal properties are almost negligible (and on purpose). The differences between those designs appear in their mechanical properties.

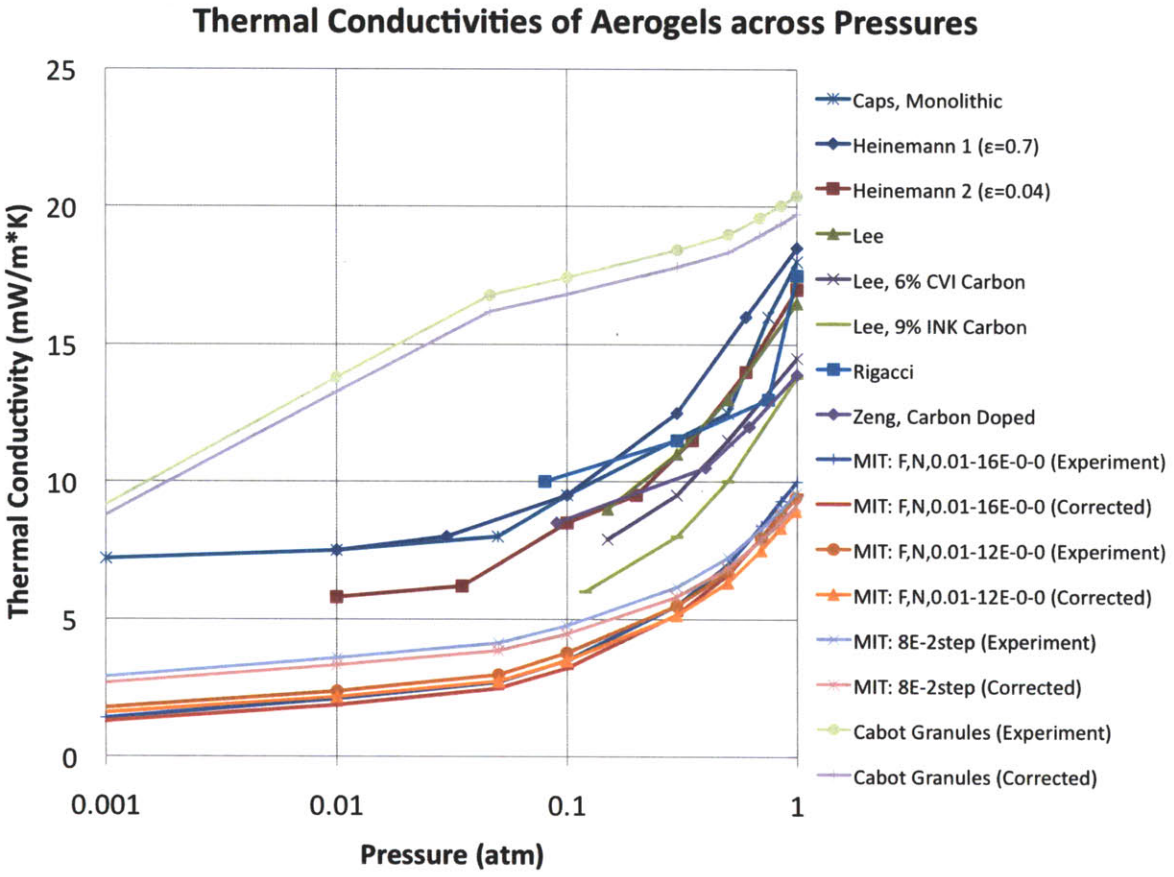

Figure 4-3: Thermal conductivity of aerogel at various pressures for a set of studies (Cohen, 2011)

4.3.4 Mechanical properties

Typical loads

It is of common knowledge that aerogel do not have mechanical properties good enough for being used in the building industry. However, it is hard to define the critical values for which mechanical properties are acceptable.

One way of defining them is to compare the mechanical properties of aerogels with the mechanical properties of other common insulating materials. That is what we did in section 2.6.2. The weakest of those materials, for example expanded polystyrene, gives a lower bound for acceptable mechanical properties since they are themselves quite weak and brittle. This gives us an indication of what the material Young's modulus, flexural strength and compressive strength should be.

Another way of deciding if the product meets the mechanical requirements is to check it can support a range of typical loads that it could be subject to during its life. We identified three kinds of typical loads (but this is not an extensive list):

- The panels are stacked on piles up to 2 meter high and the panel at the bottom must support the load of the upper panels
- One panel or a pile of several panels are transported by two ends and must resist bending
- The panel, while installed, has to resist to an indentation created by a thumb, a fist or a shoulder of someone leaning against the panel

In all the following, we will assume that the aerogel itself has no structural role in the panel. However, we will keep the maximum strain in the core less than 5% (which is the average strain at fracture in flexural test in aerogels, and close to their densification region in compression) as a constraint we cannot exceed (and we will even prefer to have a safety factor on this 5%).

Compressive Young's modulus and strength

We can calculate the Young's modulus for each of the design. Designs that differ only by the thickness of the panel will have the exact same mechanical properties because the dimensions are linearly scaled; and designs that differ only by the face material will differ only in a limited way, because the faces are thin compared to the core. Therefore, we only compare the structural performances of the cores in

Table 4.6: Young's modulus in compression of each of the cores

Type of core	Compressive Young's modulus (MPa)
polystyrene truss core (ω=45°)	22.06
polystyrene truss core (ω=39.2°)	26.50
polystyrene single wall regular honeycomb	44.13
paper double wall regular honeycomb	23.26

Table 4.7: Mechanical compressive strength of each of the cores

Type of core	Compressive yielding strength (MPa)	Compressive buckling strength (k=1) (MPa)
polystyrene truss core (ω=45°)	1.37	0.337
polystyrene truss core (ω=39.2°)	1.37	0.246
polystyrene single wall regular honeycomb	1.37	0.038
paper double wall regular honeycomb	0.37	0.009

compression in Tables 4.6 and 4.7. In Table 4.7, it appears that the cores, with their low densities, are more likely to fail in buckling. However note that there is a scaling buckling factor k ($1 \leqslant k \leqslant 4$ in the Euler buckling formula $P_{cr} = \frac{k\pi^2 E_S I}{l^2}$), and we give here the case k=1.

The calculation shows the following:

- As expected from the previous chapter, the best result for compressive Young's modulus is obtained by a honeycomb, for a given material. Polystyrene has a better ratio Young's modulus / thermal conductivity than paper.
- There is a similarity in formalism between yield strength and thermal conductivity so, for a given material, the yielding strength is the same, whatever design we choose. Note that polystyrene also has a better ratio yielding strength / thermal conductivity than paper.
- However, at these low densities, the cores are more likely to fail in buckling. In this regard, truss cores are more efficient than honeycombs. Between the two truss designs, the ω=45° appears to be the best, even though the ω=39.2° is better at a given density, just because the first design gave us a higher core density.

Under the load of a stack of panels 2 meter high, we can compute the normal strain in the core, see Table 4.8. These strains are identical for a given core design and faces (thanks to the linearity in the dimensions) but depends on the faces choice due to the fact that pine is approximately half as dense as polystyrene. We also included results for pure aerogel core as a comparison. If the strain is well

Table 4.8: Strain in the panel core under the load of a stack of panels 2 meter high

core type	polystyrene faces	pine faces
polystyrene truss core (ω=45°)	0.022%	0.017%
polystyrene truss core (ω=39.2°)	0.018%	0.014%
polystyrene single wall regular honeycomb	0.011%	0.008%
paper double wall regular honeycomb	0.019%	0.014%
pure aerogel	0.438%	0.316%

distributed, those strains (even for pure aerogel core) should not be enough to make the aerogel fail, but of course under a bigger load, the benefits of the core will become necessary, and it also gives a hint of how the core would reàct if it was not uniformly loaded.

Flexural stiffness and strength

The structural study of sandwich beams (and other sandwich structures) is developed in (Gibson and Ashby, 1997). For a rectangular beam as in Figures 4-4 and 4-5, when the faces are much thinner than the core so that $d \simeq c$, we have as a good approximation for the compliance of the beam (as a sum of a bending component from the faces and of a shear component from the core)

$$\frac{\delta}{P} = \frac{2l^3}{B_1 E_f b t c^2} + \frac{l}{B_2 b c G^*}$$

where E_f is the Young's modulus of the faces and G^* the shear modulus of the core; B_1 and B_2 are constants which depend on the geometry of loading. δ is the displacement at the center of the beam and P the applied load.

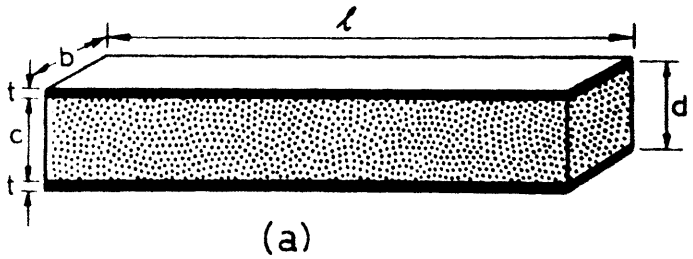

Figure 4-4: The geometry of a rectangular beam sandwich structure (Gibson and Ashby, 1997)

We first calculate the shear moduli for each core, derived from the equations in Chapter 3 (Equations

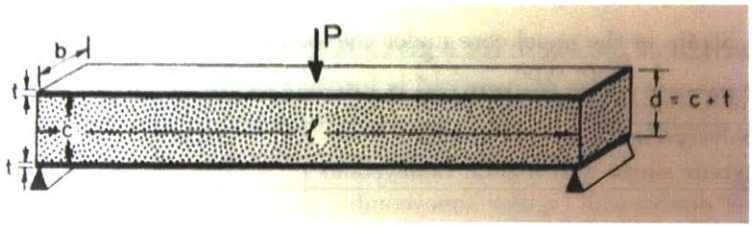

Figure 4-5: A sandwich beam loaded in 3-point bending (Gibson and Ashby, 1997)

Table 4.9: Shear modulus of each of the cores

Type of core	Shear modulus (MPa)
polystyrene truss core (ω=45°)	11.03
polystyrene truss core (ω=39.2°)	8.81
polystyrene single wall regular honeycomb	7.91
paper double wall regular honeycomb	4.36 (lowest) 7.27 (highest)

(3.4) and (3.15), Table 3.1). The moduli are given in Table 4.9. Two moduli are given for the double-wall honeycomb, corresponding to the lowest and the highest shear modulus of this anisotropic material. As a comparison, the shear modulus for aerogel in this study is about 0.4 MPa.

We give the compliance of the panel for each design under three-point bending with a uniformly distributed load ($B_1 = \frac{384}{5}$ and $B_2 = 8$) in Table 4.10. We can compare the values with those of a panel whose core is only pure aerogel, see Tabe 4.11. We draw the following conclusions:

- The panels with pine faces are around two times more compliant than those with polystyrene faces for the thicker design, and even three times more compliant for the thinner design.
- Design 1 is here the most efficient (the least compliant) and is ten times better (is ten times less compliant) than the corresponding aerogel panel.
- At this level of shear modulus for the cores and with these particular dimensions, the improvements in core shear modulus give relatively little in terms of compliance improvement; the face material has the biggest effect.

We can also compute the shear stress for various loads in the panel with the formula

$$\tau_c = \frac{P}{B_4 bc} \tag{4.1}$$

Table 4.10: Beam compliance under three-point bend with uniformly distributed load

Design number	compliance of the beam (mm/N)
1	0.00127
2	0.00346
3	0.00138
4	0.00357
5	0.00145
6	0.00363
7	0.00195
8	0.00414
9	0.00748
10	0.02498
11	0.00770
12	0.02521
13	0.00783
14	0.02533
15	0.00884
16	0.02635

Table 4.11: Beam compliance under three-point bend with uniformly distributed load of a panel with pure aerogel core

vertical dimension	face	compliance of the beam (mm/N)
core: 25.4 mm faces: 1.59 mm	polystyrene	0.01263
	pine	0.01482
core: 12.7 mm faces: 0.79 mm	polystyrene	0.03021
	pine	0.04771

Table 4.12: Shear strain in the core under three-point bend with a uniformly distributed load of 100 N, in %

	core: 25.4 mm thick faces: 1.59 mm thick	core: 12.7 mm thick faces: 0.59 mm thick
polystyrene truss core (ω=45°)	0.059%	0.119%
polystyrene truss core (ω=39.2°)	0.074%	0.049%
polystyrene single wall regular honeycomb	0.083%	0.166%
paper double wall regular honeycomb	0.150%	0.301%
pure aerogel	1.575%	3.150%

where B_4 is another constant depending on the loading geometry. This τ_c is the stress in the core structure (considered as a homogeneous media) and not the stress in the aerogel part. From τ_c we can calculate the shear strain in the core

$$\gamma_c = \frac{\tau_c}{G^*} = \frac{P}{B_4 bcG^*} \tag{4.2}$$

This shear strain is the same in the entire core, so it is also the shear strain in the aerogel. We can thus compare it to the shear strain at fracture in an aerogel, around 5%. For a three-point bending test, the constant B_4=2.

Interestingly, note that the shear stress only depends on the load and on the geometry of the core (so cores 1 to 8 and 9 to 16 respectively have the same shear stress for a given load), and thus the shear strain in the core does not depend on the faces but only on the loading configuration, the panel geometry and the core shear modulus. Table 4.12 shows results for three-point bending under a uniformly distributed load P=100 N. We see first that the thicker core behaves better (because its aspect ratio is lower). We note also that all four core designs reduce significantly the strain in the core, by a factor greater than 10; in the case we chose the pure aerogel panel is likely to break because the strain is 1.6% or 3.2%, close to the strain at fracture in bending experiments. Among all the cores, the one with the highest shear modulus, that is the polystyrene truss core with ω=45°), has subsequently the lowest strain in the core.

We can also calculate the shear strength of the cores to know if the structure will support a given load. We use Equations (3.7), (3.18) to (3.21) and Table 3.1. Note that for the yielding strength of the polystyrene (used in Equations (3.18) and (3.19)), we now use the tensile strength because the struts are loaded both in compression and tension and will fail first in tension. Note also that we do not have expressions for the yielding strength of the honeycombs in shear (but given the low density, it is very likely that they will fail in buckling). Finally, we give again the buckling strength of the truss cores for the weakest case where the struts are pin-jointed at both ends (k=1). The shear strengths are given in

Table 4.13: Mechanical compressive strength of each of the cores

Type of core	Shear yield strength (MPa)	Shear buckling strength (MPa)
polystyrene truss core (ω=45°)	0.35 (lowest) 0.40 (highest)	0.10 (lowest) 0.19 (highest)
polystyrene truss core (ω=39.2°)	0.28 (lowest) 0.33 (highest)	0.07 (lowest) 0.14 (highest)
polystyrene single wall regular honeycomb		0.040 (lowest) 0.046 (highest)
paper double wall regular honeycomb		0.002 (lowest) 0.004 (highest)

Table 4.14: Shear stress in the core under three-point bend with a uniformly distributed load of 100 N, in % of the shear strength of the core

	core: 25.4 mm thick faces: 1.59 mm thick	core: 12.7 mm thick faces: 0.79 mm thick
polystyrene truss core (ω=45°)	1.9% of the yielding strength 6.7% of the buckling strength	3.8% of the yielding strength 13.5% of the buckling strength
polystyrene truss core (ω=39.2°)	2.3% of the yielding strength 9.3% of the buckling strength	4.6% of the yielding strength 18.5% of the buckling strength
polystyrene single wall regular honeycomb	16.4% of the buckling strength	32.8% of the buckling strength
paper double wall regular honeycomb	276.2% of the buckling strength	552.4% of the buckling strength

Table 4.13.

Table 4.13 shows that honeycombs, and especially the paper honeycomb, are intrinsically weaker than the truss cores. Note than the shear strength of the paper honeycomb, at this density, is close to that of aerogel which we estimate to be of a few kPa.

We can now see if the shear stress in the core exceeds the shear strength. We take the same load P=100 N, uniformly distributed, as before, and we give the shear stress in the core as a percentage of the shear strength, see Table 4.14. The table shows that the paper honeycomb would be the only core not to sustain the load (which is an important result given that the strain was acceptable), while the polystyrene honeycomb also comes close to it. This indicates the need to use the truss core, instead of the honeycomb core.

Resistance to indentation

Another important improvement associated with the sandwich construction is that the faces is protect the aerogel from indentation. A first approach is to consider the face material and the core as a two-layer

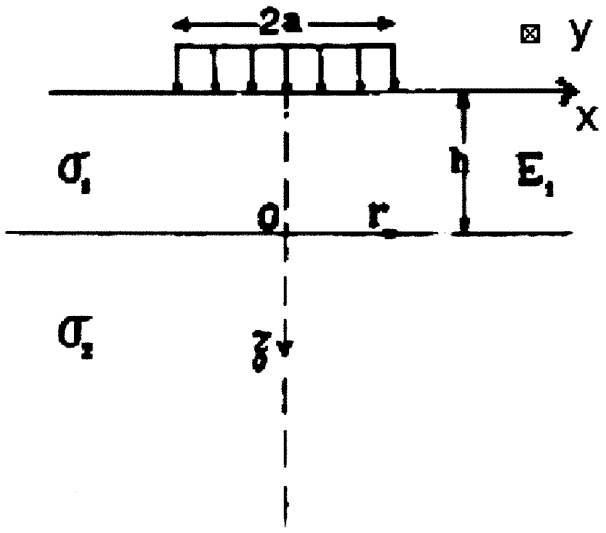

Figure 4-6: The two-layer system (Fox, 1948)

system, as pictured on Figure 4-6. The theory of two-layer systems has been developed by (Burmister, 1945; Fox, 1948; Poulos and Davis, 1974), who give a formula for the stress on the second (lower) layer along the axis. For a perfectly rough (*ie*, bonded) interface:

$$\sigma_{zz} = -(1-N)\int_0^{+\infty} \frac{a}{h} J_1(\frac{a}{h}x)dx \left[\frac{e^{-x(y+1)}(1+x+xy) - Ne^{-x(y+z)}\{1-x+xy(1-2x)\}}{1-2N(1+2x^2)e^{-2x}+N^2e^{-4x}}\right] \quad (4.3)$$

where $N = \frac{E_1-E_2}{E_1+E_2}$, E_1 being the Young's modulus of the upper layer material and E_2 the Young's modulus of the lower layer material. J_1 is a Bessel function of the first kind, a, h and the axis x, y and z are as shown in the diagram (Figure 4-6). The formula assume that the two media have a Poisson's ratio $\nu_1 = \nu_2 = 0.5$, which allowed for the simplification of the PDE system relating stress and strain. Since $\nu = 0.5$ means the material is incompressible, this probably gives an upper bound on the stress in the material ($\nu = 0.39$ for polystyrene and $\nu \simeq 0.2$ for aerogel). We also can compute

$$\sigma_{rr} = \sigma_{\theta\theta} = -\frac{(1-N)}{2}\int_0^{+\infty} \frac{a}{h} J_1(\frac{a}{h}x)dx \left[\frac{e^{-x(y+1)}(2-x-xy) - Ne^{-x(y+z)}\{2-5x-xy(1-2x)\}}{1-2N(1+2x^2)e^{-2x}+N^2e^{-4x}}\right] \quad (4.4)$$

We could apply these equations to an indentation on a sandwich panel with a core structure under the following assumptions:

1. The lower face is sufficiently far from the upper face that it does not play an important role, *ie* the thickness of the core c is great compared to a and h.

2. We can consider the core as a continuous media, *ie* if β is a dimension typical of the core spacing on a face, β is small compared to a and h.

Those assumptions are, in fact, very unlikely to hold together in a sandwich panel with a truss or honeycomb core, since c and β will generally have the same order of magnitude. Note that we could use more sophisticated models with more layers to eliminate the first assumption; but the computation would become really complicated. Thus, we are not going to use the two layer model for our truss and honeycomb core designs; but we will apply it to the case of panels with pure aerogel cores (with no truss or honeycomb structure). We compute the stress just below the first layer for a variety of loads; we can vary the size of the indenter. Then, we compute resulting strains (simply calculated as $\frac{\sigma_{zz}}{E_{zz}}$) for a variety of loads.The results are given in Table 4.15 for the case of an indenter with radius 1 cm (which is between the size of a thumb and that of a fist) and for loads from 10 to 100 N (pushing statically a thumb gives a load of around 20 N and pushing a fist a load around 60 N). We can see in the Table that a load of 50 N is already above the safety region for aerogel since the brittle failure in flexion occurs at a strain close to 5%.

Table 4.15: σ_{zz} just under the interface as a percentage of the applied stress for a=1 cm and resulting strain for various loads for a panel with pure aerogel core

vertical dimension	face	σ_{zz} (%)	strain for a 10 N load (%)	strain for a 50 N load (%)	strain for a 100 N load (%)
core: 1 in faces: 1/16 in	polystyrene	25.33	0.806	4.031	8.063
	pine	46.51	1.480	7.402	14.805
core: 1/2 in faces: 1/32 in	polystyrene	62.95	2.004	10.019	20.038
	pine	90.24	2.872	14.362	28.724

For the sandwich panels with a structural truss or honeycomb core component, we use a different method. We remark first that the worst case for indentation is when the indenter applies pressure on an area where there is no structural component below to support the load. We can approximate this case by considering the face as a plate supported only on certain points or edges and calculate the induced deflection. This should give an upper bound for the actual deflection of the face lying on pure aerogel.

Unlike truss cores, honeycomb cores requires an assumption about the size for the honeycomb cells to do the calculation. Since this is an extra factor of uncertainty, we did the calculations only for truss cores. For tetrahedral truss cores, (Roark and Young, 1975) gives formulas for an equilateral triangle plate with all edges being simply supported. This is again an approximation because in fact only the vertices of the triangle are supported by the core, so this gives an underestimate of the deflection; so in the end we only have a possible approximation.

The formula for the maximum displacement of the plate under a uniform load applied centrally over a small circle of radius r_0 ($r_0 \ll a$) is

$$\text{Max } y = 0.0069W(1-\nu^2)\frac{a^4}{Et^3} \tag{4.5}$$

where W is the load applied on the plate, ν the Poisson's ratio, a is as on Figure 4-7, E is the Young's modulus and t is the thickness of the plates (in a consistant system of units). Interestingly, the maximum displacement does not depend on r_0 (although the maximum stress does).

We have also an equation for the central deflection of the plate for a uniform load over the entire plate:

$$\text{Max } y = \frac{qa^4(1-\nu^2)}{81Et^3} \tag{4.6}$$

where q is the load per unit surface. We can also use this equation to give an order of magnitude estimate for indentation of larger objects, when the approximation $r_0 \ll a$ does not hold.

We give the results for the two tetrahedral cores for both types of loading with a total applied load of W=50 N (the intermediate load in Table 4.15, corresponding to 5 kg, around twice of what a thumb can statically apply), on Tables 4.16 and 4.17. We consider only polystyrene faces because the pine faces add the problem of anisotropy.

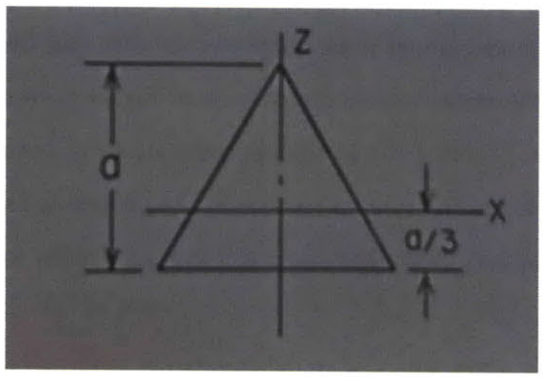

Figure 4-7: Equilateral triangle plate (all edges are simply supported) (Roark and Young, 1975)

Table 4.16: Maximum displacement of a polystyrene triangular plate and corresponding strain in the core under a concentrated load of W=50 N

	core: 25.4 mm thick faces: 1.59 mm thick	core: 12.7 mm thick faces: 0.79 mm thick
polystyrene truss core (ω=45°)	0.855 mm 53.87%	0.428 mm 52.87 %
polystyrene truss core (ω=39.2°)	0.378 mm 23.83 %	0.189 mm 23.83%

Table 4.17: Maximum displacement of a polystyrene triangular plate and corresponding strain in the core under a uniformly distributed load of W=50 N

	core: 25.4 mm thick faces: 1.59 mm thick	core: 12.7 mm thick faces: 0.79 mm thick
polystyrene truss core (ω=45°)	0.118 mm 7.42%	0.059 mm 7.42%
polystyrene truss core (ω=39.2°)	0.052 mm 3.28%	0.026 mm 3.28%

Tables 4.16 and 4.17 show that the thicker and the thinner designs give the same strain since they are linearly related; they show also that the core with ω=39.2° has better performance (lower strain), because the lower angle gives more contact points between the core and the face.

However, we can see that the strain results are close to or higher than those found for a polystyrene plate on an aerogel foundation (Table 4.15) so the approximations of considering aerogel as having no structural role in the composite structure or of considering the edges as fixed under an indentation are too strong. There is no obvious way other than finite element simulation to get a better estimate.

4.3.5 Conclusions

We can draw the following conclusions from our calculations:

- The honeycombs perform worse than the truss cores. They have better elastic properties in compression but lower shear properties and above all a lower strength under all loads because of the thinness of their walls leading to buckling under small loads. Note however that filling the honeycombs with aerogel could improve this behavior, but it is not likely that they could come close to the truss cores.

- Among the truss cores, the one with the wider angle (ω=45°) has the best properties in shear and the best compressive strength, while the one with a sharper angle (ω=39.2°) has better compressive Young's modulus. Note also that the latter is likely to behave better to protect the aerogel from indentation but this was difficult to quantify.

- The dimensions do not play an important role, except in bending where the greater aspect ratio of the thinnest panels make them weaker.

- For the faces, the polystyrene showed a better behaviour because the pine is anisotropic and clearly weaker than polystyrene in the transverse direction. However no calculation showed a major inconvenience in the use of pine, other possibly than the indentation where we could not carry out calculations for pine. If pine behaves similarly to polystyrene in indentation, the mechanical properties should not be a determining factor in the choice of the face material.

Only experimentation over actual panels could provide enough insight over which panel is actually the best and confirm these calculations.

4.4 Demonstration

4.4.1 Experiment

Due to the unavailability of an autoclave and a pump of sufficient size and power, it was impossible to test those designs at their true scale. The autoclave at our disposal for synthesis of aerogel samples is a cylinder of inner diameter 28 mm.

We decided to try to synthesize a composite panel of smaller size. We were limited to a box of inner dimensions 22 mm wide and 6 mm high (with walls 1.5 mm thick); we chose to make square boxes 22 mm x 22 mm. The truss cores were chosen to have a regular tetrahedral geometry, which allows for more tetrahedrons in a given surface at fixed height than, for example, $\omega = 45°$ tetrahedrons.

The truss cores were made with a Connex500 3-D printer (Objet Geometries Inc., Billerica, MA, USA). The material used was FullCure720, which is a transparent polymer whose mechanical properties are close to those of polystyrene. One of the cores is shown on Figure 4-8.

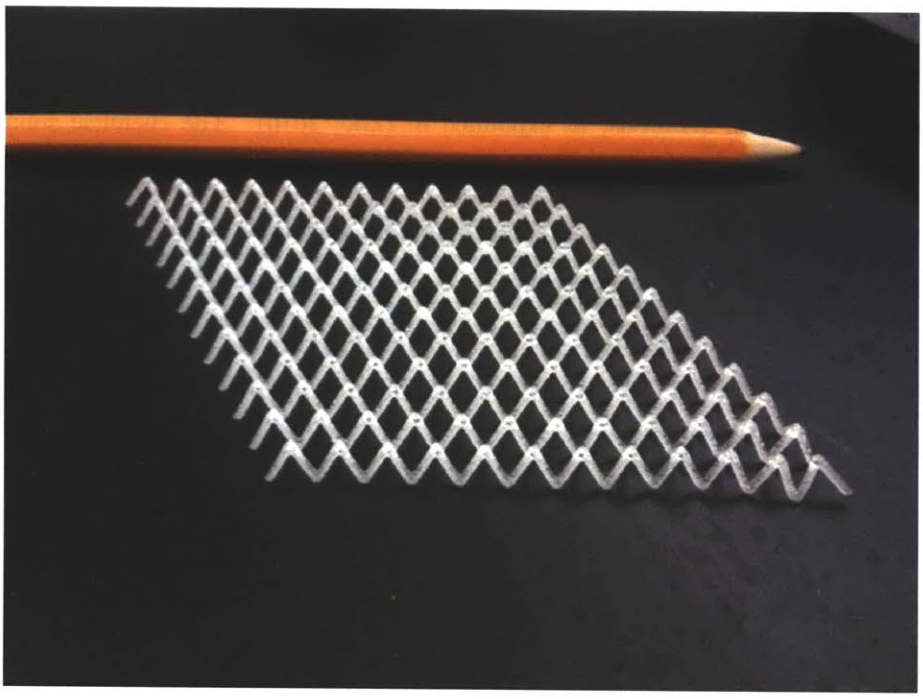

Figure 4-8: A tetrahedral truss core made by 3D-printing

Two different densities of cores were made. Both were regular tetrahedrons with struts of length 6.0 mm, giving a height of 4.9 mm for the core, which fits in the box. One core had struts of radius 0.60

mm (relative density of 4.24%) and the other had struts of radius 0.45 mm (relative density of 2.40%, achieving the 2 mW/m.K goal for this geometry). The two types of cores are shown on Figure 4-9.

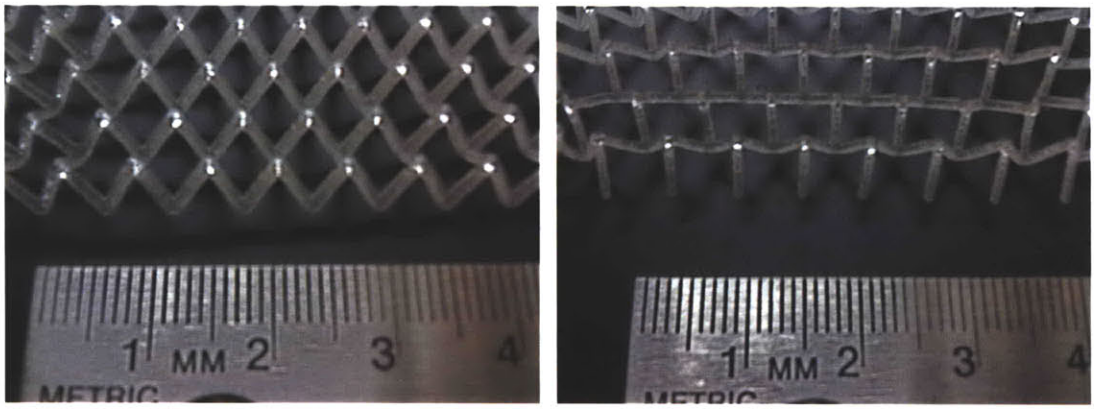

(a) (b)

Figure 4-9: Tetrahedral truss core made by 3D-printing with density (a) 4.24% and (b) 2.40%

The cores were then cut into square pieces of slightly less than 22 x 22 mm. Some of them were bonded on one side to polystyrene faces either with epoxy or cyclohexane glue. They were put in the boxes which became molds for the aerogel synthesis, as explained in (Zuo, 2010). The chemical solution and the gelation process took place around the truss. Then they were put in the autoclave to be supercritically dried. Unlike the method for a cylindrical sample, the gel remained in the mold during the drying process since it needed a flat support during gelation, due to the cylindrical shape of the autoclave. Note, however, that this prevents the diffusion of the solvent in all directions.

In total, we prepared and dried one witness sample, three samples with cores of density 4.24% and two with cores of density of 2.40%.

4.4.2 Results

We synthesized first a control sample: pure aerogel synthesized in the same conditions. It is shown in Figure 4-10. We remark that this sample is bent, probably due to the asymmetry in the drying conditions (one face is against a wall of the mold while the other face is free).

The samples with truss cores behaved quite differently as a function of the density of the core. The denser core created many cracks in the aerogel, as can be seen in Figure 4-11. The samples with cores of lower density, on the other hand, are quite encouraging, as can be seen in Figure 4-12. The aerogel was dried around the truss core with few or no cracks. We think this is related to the strut diameter

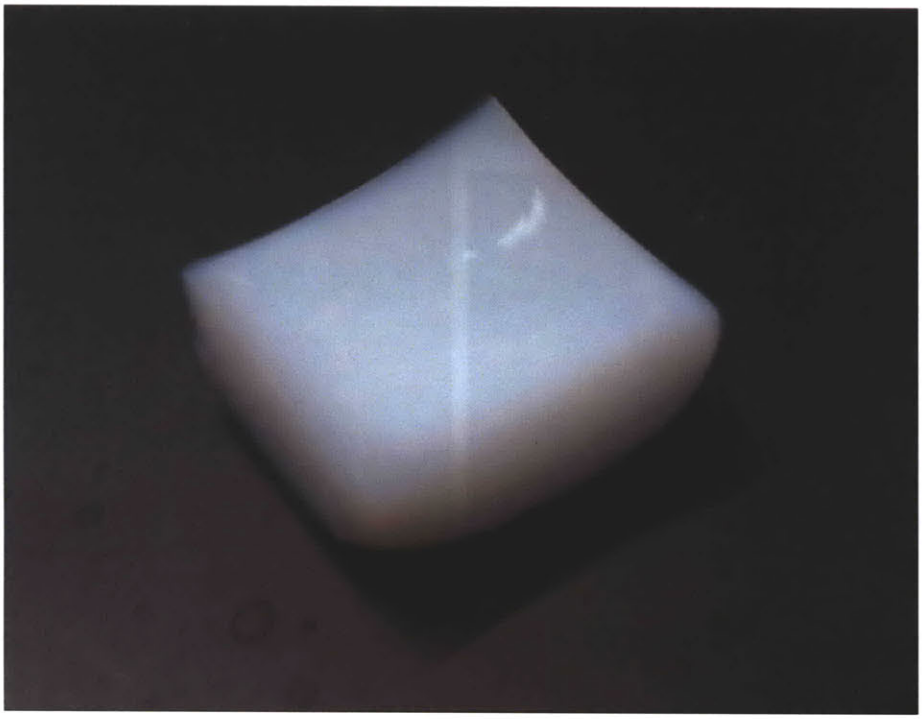

Figure 4-10: The control core made of pure aerogel

(more than to the density itself), but this would have to be confirmed by further experiments. Another explanation could be that, due to the particular drying configuration, the aerogel tries to bend during the supercritical drying and is more restrained to do so by the stiffer higher density lattice, producing higher stresses in the aerogel and causing cracking.

Neither the epoxy nor the glue held during the chemical process and the supercritical drying for all of the cores, so either other ways of bonding the core to the faces have to be found, or the bonding has to be done afterwards.

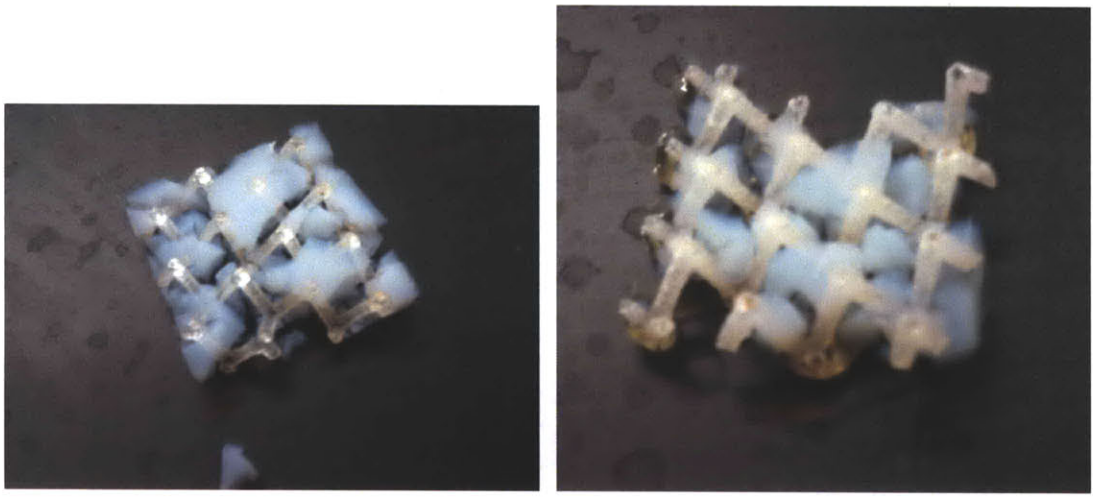

Figure 4-11: Aerogel embedded in the core 4.24% dense (struts of radius 0.60 mm)

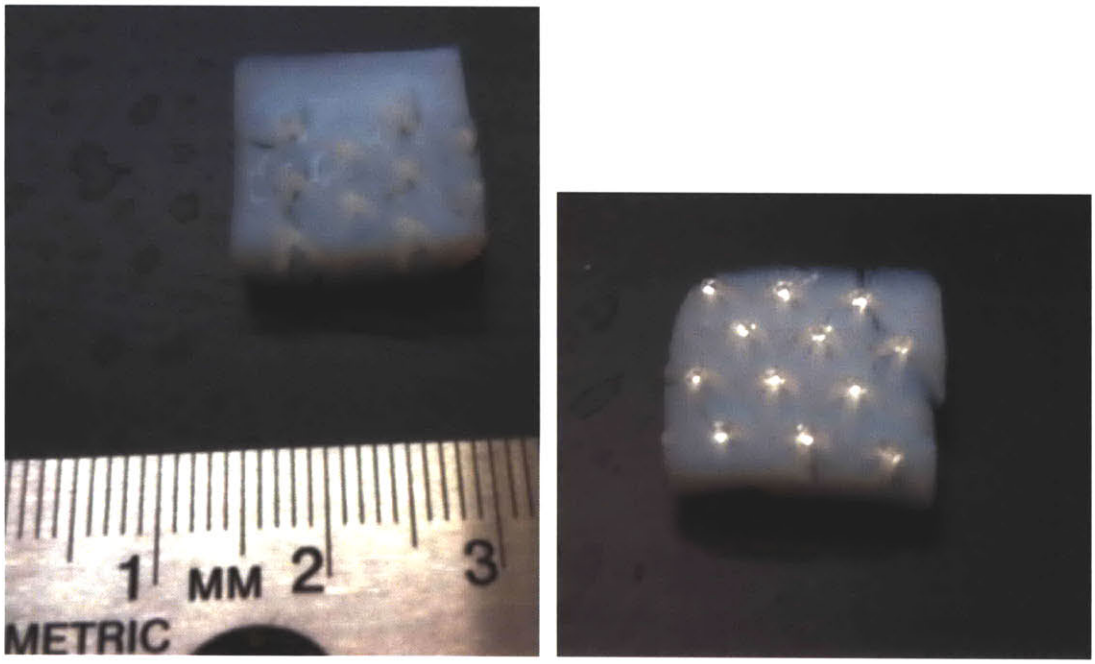

Figure 4-12: Aerogel embedded in the core 2.40% dense (struts of radius 0.45 mm)

4.4.3 Discussion

This experiment gives the following guidelines for future attempts at making composite panels.

1. The diffusion process has to be better controlled in order to prevent the aerogel from bending during the drying, because the bending likely increases the probability of cracks, especially for stiffer cores. If another autoclave with flat surfaces is available, it is probably better to dry the sample out of the mold.

2. The diameter of the struts may be an important criteria. We recommend experiments to determine if there is a critical diameter of the struts for them to be embedded in aerogel during the synthesis without breaking it during the drying, as well as the parameters that could have an influence over this diameter (truss material, chemistry of the aerogel).

3. Since for a truss core of given angle, the target thermal properties and mechanical properties determine the density of the core and thus the diameter of the struts, we may have to consider other geometries. In particular, the octet-truss lattice material (Deshpande et al., 2001), which is basically a stack of tetrahedral cores (see Figure 4-13), is an interesting option because it would allow independent modification of the density of the core and the diameter of the struts by controlling the cell size. However it adds some extra material (the horizontal material) compared to a single-layer core.

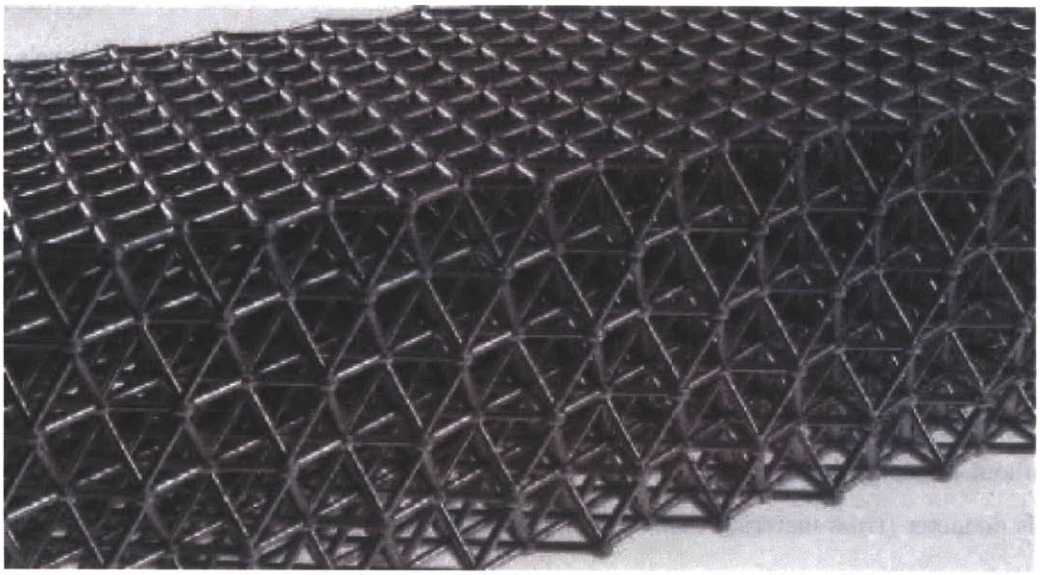

Figure 4-13: Photograph of the octet-truss lattice material, here made from a casting aluminium alloy (Deshpande et al., 2001)

4.5 Alternate designs

All those designs are designs of rigid panels containing monolithic aerogel. Some alternate decisions could be made.

- Use granulates instead of monolithic aerogel, either inside of rigid panels or, as commercially available, as loose insulation or embedded in fiber blankets. This avoids the challenges of monolithic aerogel synthesis; however lower thermal insulation is to be expected because of the voids between granules. One would have to get an optimal arrangement of the particles with preferably various sizes for the particles.

- Use an articulated system of small rigid panel. This solution is subject to a technology disclosure of Prof. Leon Glicksman and Ellann Cohen (Cohen, 2011).

Chapter 5

Conclusion and future research

5.1 Summary of the work

The work in this thesis can be summarized in the following points:

1. We reviewed the existing literature on the structure of aerogels, their mechanical properties and the models that simulate the structure and relate it to mechanical properties. We also made mechanical tests on the aerogels of this study.

2. We reviewed the aerogels currently available on the market. We concluded that we wanted a product with better insulation property that could only be provided through the use of monolithic aerogel. We also came to the conclusion that monolithic aerogel alone cannot be made strong enough to make a viable product. We thus proposed the concept of a composite panel with a macroscopic structure (truss or honeycomb core) to support the mechanical loads.

3. We studied analytically the cores we suggested using. We made experiments to compare the theoretical and measured behavior of polystyrene truss cores. We found a good fit between data and predictions, which gives confidence that the analysis correctly describes the behavior of the cores.

4. We proposed a number of specific designs that we studied analytically. We could give some criteria for the choice of the core geometry (a truss core with a relatively wide angle seems more appropriate for a number of loading configurations), while some other characteristics were calculated to have little effect (the face material).

5. We tested on a small scale embedding aerogel in a truss core. The results of the attempt were encouraging. We learnt that the diameter of the struts in the truss core is probably a critical parameter. We also note the possibility of using structures like the octet-truss material to reduce the diameter of the struts, the length of the struts and maintain an overall desired core thickness.

5.2 Future research

The main direction for further research is to extend the tests on the manufacturing of the composite panel. First of all, larger samples would need to be made in order to have a representative number of cells in the truss core, and also to make mechanical and thermal tests. For example, a thermal conductivity test with guarded hot plates requires samples at least 600 x 600 mm. As a first step, panels 150 x 150 mm seem to be a reasonable objective.

We also need to have a better knowledge of the criteria required for a structural truss core to be embedded in aerogel without cracking during the supercritical drying. Depending on these criteria, we may have to study new types of cores such as the octet-truss lattice material to allow for a smaller diameter of the struts.

Bibliography

Alaoui, A. H., Woignier, T., Scherer, G. W., and Phalippou, J. (2008). Comparison between flexural and uniaxial compression tests to measure the elastic modulus of silica aerogel. *Journal of Non-Crystalline Solids*, 354:4556–4561.

Alié, C., Pirard, R., and Pirard, J.-P. (2001). Mercury porosimetry: applicability of the buckling-intrusion mechanism to low-density xerogels. *Journal of Non-Crystalline Solids*, 292:138–149.

ASTM International (2007). C 273/C 273M Standard test method for shear properties of sandwich core materials.

ASTM International (2008). D 638 Standard test method for tensile properties of plastics.

Barrett, E. P., Joyner, L. G., and Halenda, P. P. (1951). The determination of pore volume and area distributions in porous substances. I. Computations from nitrogen isotherms. *Journal of the American Chemical Society*, 73:373–380.

Borne, A., Chevalier, B., Chevalier, J. L., Quenard, D., Elaloui, E., and Lambard, J. (1995). Characterization of silica aerogel with the atomic force microscope and SAXS. *Journal of Non-Crystalline Solids*, 188:235–242.

Botet, R., Jullien, R., and Kolb, M. (1984). Hierarchical model for irreversible kinetic cluster formation. *Journal of Physics A: Mathematical and General*, 17:L75–L79.

Bouaziz, J., Bourret, D., Sivade, A., and Grill, C. (1992). Phase separation during isothermal sintering of (1-x)SiO_2 - $x Ln_2O_3$ aerogels. *Journal of Non-Crystalline Solids*, 145:71–74.

Bourret, A. (1988). Low-density silica aerogels observed by high-resolution electron microscopy. *Europhysics Letters*, 6:731–737.

Bouwhuis, B. and Hibbard, G. (2006). Compression testing of periodic cellular sandwich cores. *Metallurgical and Materials Transactions B*, 37B:919–927.

Brun, M., Lallemand, A., Quinson, J. F., and Eyraud, C. (1977). New method for simultaneous determination of size and shape of pores - thermoporometry. *Thermochimica Acta*, 21(1):59–88.

Burmister, D. M. (1945). The general theory of stresses and displacements in layered systems. I*. *Journal of Applied Physics*, 16:89–94.

Chiras, S., Mumm, D. R., Evans, A. G., Wicks, N., Hutchinson, J. W., Dharmasena, K., Wadley, H. N. G., and Fichter, S. (2002). The structural performance of near-optimized truss core panels. *International Journal of Solids and Structures*, 39:4093–4115.

Cohen, E. (2011). Master's thesis, Massachussets Institute of Technology.

DeFriend, K. A., Espinoza, B., and Patterson, B. (2007). Templating silica aerogel with polystyrene to improve their mechanical properties. *Fusion Science and Technology*, 51:693–700.

Deshpande, V. S. and Fleck, N. A. (2001). Collapse of truss core sandwich beams in 3-point bending. *International Journal of Solids and Structures*, 38:6275–6305.

Deshpande, V. S., Fleck, N. A., and Ashby, M. F. (2001). Effective properties of the octet-truss lattice material. *Journal of the Mechanics and Physics of Solids*, 49:1747–1769.

Dumas, J., Serughetti, J., Rousset, J. L., Boukenter, A., Champagnon, B., Duval, E., and Quinson, J. F. (1990). Gel to glass transformation of silica. *Journal of Non-Crystalline Solids*, 121:128–131.

Ehrburger-Dolle, F., Holz, M., Mauzac, C., Lahaye, J., and Pajonk, G. M. (1992). Characterization of the porous texture of aerogel, precipitated and pyrogenic silica. *Journal of Non-Crystalline Solids*, 145:185–190.

Emmerling, A. and Fricke, J. (1992). Small angle scattering and the structure of aerogels. *Journal of Non-Crystalline Solids*, 145:113–120.

Emmerling, A. and Fricke, J. (1997). Scaling properties and structure of aerogels. *Journal of Sol-Gel Science and Technology*, 8:781–788.

Esquivias, L., Rodriguez-Ortega, J., Barrera-Solano, C., and De La Rosa-Fox, N. (1998). Structural models of dense gels. *Journal of Non-Crystalline Solids*, 225:239–243.

European Environment Agency (2008). Energy and environment report.

Evans, A. G., Hutchinson, J. W., Fleck, N. A., Ashby, M. F., and Wadley, H. N. G. (2001). The topological design of multifunctional cellular metals. *Progress in Materials Science*, 46:309–327.

Finnegan, K., Kooistra, G., Wadley, H. N. G., and Deshpande, V. S. (2007). The compressive response of carbon fiber composite pyramidal truss sandwich cores. *International Journal of Materials Research*, 98(12):1264–1272.

Fox, L. (1948). Computations of traffic stresses in a simple road structure. In *Proceedings of the 2nd International Conference on Soil Mechanics and Foundation Engineering*, pages 236–246.

Fricke, J. and Emmerling, A. (1992). Aerogels - preparation, properties, applications. *Structure and Bonding*, 77:37–87.

Gelb, L. D. (2007). Simulating silica aerogels with a coarse-grained flexible model and Langevin dynamics. *The Journal of Physical Chemistry C*, 111:15792–15802.

Gibson, L. J. and Ashby, M. F. (1997). *Cellular solids: Structure and Properties.* Cambridge University Press, 2nd edition.

Granta Design Limited (1999). Cambridge Engineering Selector.

Gross, J., Fricke, J., Pekala, R. W., and Hrubesh, L. W. (1992). Elastic nonlinearity of aerogels. *Physical Review B*, 45(22):12774–12777.

Gross, J., Reichenauer, G., and Fricke, J. (1988). Mechanical properties of SiO_2 aerogels. *Journal of Physics D: Applied Physics*, 21:1447–1451.

Hasmy, A., Anglaret, É., Forest, M., Pelous, J., and Jullien, R. (1994). Small-angle neutron-scattering investigation of long-range correlations in silica aerogels: Simulations and experiments. *Physical Review B*, 50(9):6006–6016.

Hasmy, A., Foret, M., Pelous, J., and Jullien, R. (1993). Small-angle neutron-scattering investigation of short-range correlations in fractal aerogels: Simulation and experiments. *Physical Review B*, 48(13):9345–9354.

Hüsing, N., Schubert, U., Misof, K., and Fratzl, P. (1998). Formation and structure of porous gel networks from $Si(OMe)_4$ in the presence of $A(CH_2)_nSi(OR)_3$ (A = functional group). *Chemistry of Materials*, 10:3024–3032.

Ilhan, U. F., Fabrizio, E. F., McCorkle, L., Scheiman, D. A., Dass, A., Palczer, A., Meador, M. A. B., Johnston, J. C., and Leventis, N. (2006). Hydrophobic monolithic aerogels by nanocasting polystyrene on amine-modified silica. *Journal of Materials Chemistry*, 16:3046–3054.

Jarzebski, A. B., Lorenc, J., Aristov, Y. I., and Lisitza, N. (1995). Porous texture characteristics of a homologous series of base-catalysed silica aerogels. *Journal of Non-Crystalline Solids*, 190:198–205.

Kistler, S. S. (1931). Coherent expanded aerogels and jellies. *Nature*, 127:741–741.

Kolb, M., Botet, R., and Jullien, R. (1983). Scaling of kinetically growing clusters. *Physical Review Letters*, 51(13):1123–1126.

Kucheyev, S. O., Toth, M., Baumann, T. F., Hamza, A. V., Ilavsky, J., Knowles, W. R., Saw, C. K., Thiel, B. L., Tileli, V., van Buuren, T., Wang, Y. m., and Willey, T. M. (2007). Structure of low-density nanoporous dielectrics revealed by low-vacuum electron microscopy and small-angle x-ray scattering. *Langmuir*, 23:353–356.

Lee, D., Stevens, P. C., Zeng, S. Q., and Hunt, A. J. (1995). Thermal characterization of carbon-opacified silica aerogel. *Journal of Non-Crystalline Solids*, 186:285–290.

Lowell, S., Shiels, J. E., Thomas, M. A., and Thommes, M. (2004). *Characterization of Porous Solids and Powders: Surface Area, Pore Size and Density.* Kluwer Academic Publishers.

Ma, H.-S., Prévost, J.-H., , and Scherer, G. W. (2002). Elasticity of DLCA model gels with loops. *International Journal of Solids and Structures*, 39:4605–4614.

Ma, H.-S., Prévost, J.-H., Jullien, R., and Scherer, G. W. (2001). Computer simulation of mechanical structure-property relationship of aerogels. *Journal of Non-Crystalline Solids*, 285:216–221.

Ma, H.-S., Roberts, A. P., Prévost, J.-H., Jullien, R., and Scherer, G. W. (2000). Mechanical structure-property relationship of aerogels. *Journal of Non-Crystalline Solids*, 277:127–141.

Marlière, C., Despetis, F., Etienne, P., Woignier, T., Dieudonné, P., and Phalippou, J. (2001). Very large-scale structures in sintered silica aerogels as evidenced by atomic force microscopy ans ultra-angle x-ray scattering experiments. *Journal of Non-Crystalline Solids*, 285:148–153.

Martin, J., Hosticka, B., Lattimer, C., and Norris, P. M. (2001). Mechanical and acoustical properties as a function of peg concentration in macroporous silica gels. *Journal of Non-Crystalline Solids*, 285:222–229.

Meador, M. A. B., Fabrizio, E. F., Ilhan, F., Dass, A., Zhang, G., Vassilaras, P., Johnston, J. C., and Leventis, N. (2005). Cross-linking amine-modified silica aerogels with epoxies: Mechanically strong lightweight porous materials. *Chemistry of Materials*, 17:1085–1098.

Meakin, P. (1983). Formation of fractal clusters and networks by irreversible diffusion-limited aggregation. *Physical Review Letters*, 51(13):1119–1122.

Moner-Girona, M., Roig, A., Molins, E., Martìnez, E., and Esteve, J. (1999). Micromechanical properties of silica aerogels. *Applied Physics Letters*, 75(5):653–655.

Morales-Flórez, V., de la Rosa-Fox, N., Piñero, M., and Esquivias, L. (2005). The cluster model: A simulation of the aerogel structure as a hierarchically-ordered arrangement of randomly packed spheres. *Journal of Sol-Gel Science and Technology*, 35:203–210.

Morales-Flórez, V., Piñero, M., de la Rosa-Fox, N., Esquivias, L., Anta, J. A., and Primera, J. (2008). The cluster model: a hierarchically-ordered assemblage of random-packing spheres for modelling microstructure of porous materials. *Journal of Non-Crystalline Solids*, 354:193–198.

Oliver, W. C. and Pharr, G. M. (1992). An improved technique for determining hardness and elastic modulus using load and displacement sensing indentation experiments. *Journal of Materials Research*, 7:1564–1583.

Pajonk, G. M., Venkateswara Rao, A., Parvathy, N. N., and Elaloui, E. (1996). Microstructural characterization of silica aerogels using scanning electron microscopy. *Journal of Materials Science*, 31:5683–5689.

Parmenter, K. E. and Milstein, F. (1998). Mechanical properties of silica aerogels. *Journal of Non-Crystalline Solids*, 223:179–189.

Pekala, R. W., Hrubesh, L. W., Tillotson, T. M., Alviso, C. T., Poco, J. F., and LeMay, J. D. (1991). A comparison of mechanical properties and scaling law relationships for silica aerogels and their organic counterparts. In Sieradzki, K., Green, D. J., and Gibson, L. J., editors, *Mechanical Properties of Porous and Cellular Materials*, volume 207, pages 197–200. Material Research Society Symposium Proceedings, Materials Research Society.

Phalippou, J., Woignier, T., and Rogier, R. (1989). Fracture-toughness of silica aerogels. *Journal de Physique*, 50(C-4):C4191–C4196. Suppl. 4.

Pierre, A. C. and Pajonk, G. M. (2002). Chemistry of aerogels and their applications. *Chemical Reviews*, 102:4243–4265.

Pirard, R., Blacher, S., Brouers, F., and Pirard, J. P. (1995). Interpretation of mercury porosimetry applied to aerogels. *Journal of Materials Research*, 10(8):2114–2119.

Pirard, R. and Pirard, J.-P. (1997). Aerogel compression theoretical analysis. *Journal of Non-Crystalline Solids*, 212:262–267.

Poulos, H. G. and Davis, E. H. (1974). *Elastic solutions for soil and rock mechanics.* John Wiley & Sons.

Queheillalt, D. T. and Wadley, H. N. G. (2005). Pyramidal lattice truss structures with hollow trusses. *Materials Science and Engineering A*, 397:132–137.

Reichenauer, G. and Scherer, G. W. (2001). Extracting the pore size distribution of compliant materials from nitrogen adsorption. *Colloids and Surfaces A: Physicochemical and Engineering Aspects*, 187-188:41–50.

Reidy, Richard, F., Allen, A. J., and Krueger, S. (2001). Small angle neutron scattering characterization of colloidal and fractal aerogels. *Journal of Non-Crystalline Solids*, 285:181–186.

Rigacci, A., Achard, P., Ehrburger-Dolle, F., and Pirard, R. (1998). Structural investigation in monolithic silica aerogels and thermal properties. *Journal of Non-Crystalline Solids*, 225:260–265.

Roark, R. J. and Young, W. C. (1975). *Formulas for Stress and Strain.* McGraw-Hill Book Company, fifth edition edition.

Rousset, J. L., Boukenter, A., Champagnon, B., Dumas, J., Duval, E., Quinson, J. F., and Serughetti, J. (1990). Granular structure and fractal domains of silica aerogels. *Journal of Physics: Condensed Matter*, 2:8845–8455.

Roy, S. and Hossain, A. (2008). *Multiscale modeling and simulation of composite materials and structures*, chapter Modeling of Stiffness, Strength, and Structure-Property Relationship in Crosslinked Silica Aerogel, pages 463–494. Springer.

Ruben, G. C., Hrubesh, L. W., and Tillotson, T. M. (1995). High resolution transmission electron microscopy nanostructure of condensed-silica aerogels. *Journal of Non-Crystalline Solids*, 186:209–218.

Rumpf, H. (1958). Grundlagen und Methoden des Granulierens. *Chemie Ingenieur Technik*, 30(3):144.

Schaefer, D. W. and Keefer, K. D. (1986). Structure of random porous materials: Silica aerogel. *Physical Review Letters*, 56(20):2199–2202.

Scherer, G. W. (1997). Effect of drying on properties of silica gel. *Journal of Non-Crystalline Solids*, 215:155–168.

Scherer, G. W. (1998). Characterization of aerogels. *Advances in Colloid and Interface Science*, 76-77:321–339.

Scherer, G. W., Smith, D. M., Qiu, X., and Anderson, J. M. (1995a). Compression of aerogels. *Journal of Non-Crystalline Solids*, 186:316–320.

Scherer, G. W., Smith, D. M., and Stein, D. (1995b). Deformation of aerogels during characterization. *Journal of Non-Crystalline Solids*, 186:309–315.

Smith, D. M., Maskara, A., and Boes, U. (1998). Aerogel-based thermal insulation. *Journal of Non-Crystalline Solids*, 225:254–259.

Stroud, R. M., Long, J. W., Pietron, J. J., and Rolison, D. R. (2004). A practical guide to transmission electron microscopy of aerogels. *Journal of Non-Crystalline Solids*, 350:277–284.

Sypeck, D. J. and Wadley, H. N. G. (2002). Cellular metal truss core sandwich structures. *Advanced Engineering Materials*, 4(10):759–764.

Tweedie, C. A., Constantinides, G., Lehman, K. E., Brill, D. J., Blackman, G. S., and Van Vliet, K. J. (2007). Enhanced stiffness of amorphous polymer surfaces under confinement of localized contact loads. *Advanced Materials*, 19:2540–2546.

U.S. Energy Information Administration (2008). Annual energy outlook 2008.

Vacher, R., Courtens, E., Stoll, E., Böffgen, M., and Rothuizen, H. (1991). Pores in fractal aerogels and their incidence on scaling. *Journal of Physics: Condensed Matter*, 3:6531–6545.

Vacher, R., Woignier, T., Phalippou, J., Pelous, J., and Courtens, E. (1988). Fractal structure of base catalysed and densified silica aerogels. *Journal of Non-Crystalline Solids*, 106:161–165.

VanLandingham, M. R., Villarubia, J. S., Guthrie, W. F., and Meyers, G. F. (2001). Nanoindentation of polymers: An overview. *Macromolecular Symposia*, 167:15–43.

Wallach, J. C. and Gibson, L. J. (2001). Mechanical behavior of a three-dimensional truss material. *Internation Journal of Solids and Structures*, 38:7181–7196.

Wicks, N. and Hutchinson, J. W. (2001). Optimal truss plates. *International Journal of Solids and Structures*, 38:5165–5183.

Witten, T. A. J. and Sander, L. M. (1981). Diffusion-limited aggregation, a kinetic critical phenomenon. *Physical Review Letters*, 47(19):1400–1403.

Woignier, T., Despetis, F., Alaoui, A., Etienne, P., and Phalippou, J. (2000). Mechanical properties of gel-derived materials. *Journal of Sol-Gel Science and Technology*, 19:163–169.

Woignier, T., Pelous, J., Phalippou, J., Vacher, R., and Courtens, E. (1987). Elastinc properties of silica aerogels. *Journal of Non-Crystalline Solids*, 95-96:1192–1202.

Woignier, T. and Phalippou, J. (1988). Mechanical strength of silica aerogels. *Journal of Non-Crystalline Solids*, 100:404–408.

Woignier, T., Phalippou, J., and Vacher, R. (1989). Parameters affecting elastic properties of silica aerogels. *Journal of Materials Research*, 4(3):688–692.

Woignier, T., Reynes, J., Alaoui, A. H., Beurroies, I., and Phalippou, J. (1998). Different kinds of structure in aerogels: relationships with the mechanical properties. *Journal of Non-Crystalline Solids*, 241:45–52.

Zarzycki, J. (1992). Structure of dense gels. *Journal of Non-Crystalline Solids*, 147&148:176–182.

Zhihua, Z., Jun, S., Yang, L., Jichao, W., Guangming, W., Bin, Z., Guoqing, W., Peiqing, W., Qingfeng, W., and Xixian, N. (2008). Mechanical reinforcment of silica aerogel insulation with ceramic fibers. In *2nd IEEE International Nanoelectronics Conference.*

Zuo, Y. (2010). Preparation of silica aerogels with improved mechanical properties and extremely low thermal conductivities through modified sol-gel process. Master's thesis, Massachussets Institute of Technology.